Construction and test of high resolution and radiation hard particle detectors for fundamental physics at the LHC experiments and search for signal of new physics through displaced and collimated jet-like structures with ATLAS experiment

University of Calabria

Giovandomenico Carducci

Advisor: Prof. Marco Schioppa

Day Month Year

Contents

Introduction

The following thesis is the result of the work carried out from mid 2016 to mid 2021, as a SIACE PhD student at the University of Calabria physics department and INFN cooperation associated, within the ATLAS collaboration.
The first part of the thesis, which is also the most consistent, is dedicated to the description of the techniques adopted for the construction of the tracking MICROMEGAS detectors (in the following MM 4-plets) of the ATLAS New Small Wheel project, as well as the description of the quality tests and relative stands developed "ad hoc" for them validation.
The New Small Wheel project provides for the upgrade of the ATLAS experiment endcap muon spectrometer, or the Small Wheels, with a more efficient tracking and triggering system that will ensure high spatial and temporal resolutions in a high radiation flux environment like that expected in the future eras of the Large Hadron Collider.
MICROMEGAS technology was born in 1996 and has been used for a long time only for the construction of small detectors (see e.g. the COMPASS experiment). In 2007 it was proposed to adopt this technology as an upgrade of the ATLAS muon spectrometer. From 2008 to 2016 the ATLAS collaboration carried out research and development, design and prototyping phases in order to make the MICROMEGAS technology application possible on large surface detectors and minimize the detector spark probability. The good results obtained during these years paved the way for the mass production of MM 4-plets for the New Small Whell project. The series production, which began in July 2016, saw the involvement of some of the most important European research institutes, including INFN. Despite the long research and development phase, mass production of MICROMEGAS 4-plets has met with several issues. In particular, the problem that most affected the operation of these detectors, and which seems to be mainly linked to a design defect, was their HV stability which forced the NSW collaboration to interrupt the production of detectors several times and to adopt significant invasive solutions.
In May 2021, one of the two New Small Wheels was completed and in the following July it was lowered into the ATLAS experimental area. Completion of the second New Small Wheel is scheduled for October. Once the commissioning phase is complete, the New Small Wheel will reconstruct the muon tracks coming from the ATLAS interaction point at least for the next 10 years, i.e. for the Large Hadron Collider RUN 3 and RUN 4.
The first chapter of the thesis is an introduction to the basic parameters of the Large Hadron Collider and the ATLAS experiment structure are briefly described, placing more attention on the muon spectrometer and its trigger system.
The second chapter is dedicated to the MICROMEGAS detector operating principle, to the New Small Wheel project and to the MM 4-plet mechanical and electrical structure.
The third chapter describes the construction techniques, the quality tests and the relative stands adopted for the mass production and the validation of the detectors, focusing on the detector drift plane mechanical and electrical "preparation and finalization". Also in

this chapter the different causes of the HV detector instability and the solutions adopted are described.
The fourth chapter, which closes the first part of the thesis, is completely dedicated to the study of the gas tightness of the detector. After a brief theoretical introduction, is presented an experimental method which allows to estimate the gas tightness of an elastic volume subjected to atmospheric pressure and temperature variations.
The last two chapters are dedicated to two different topics. The fifth chapter deals with the Non Collision Background problem in the ATLAS cavern. The ATLAS experiment, although being at a 100 m depth underground, is continuously crossed by the most energetic cosmic muons. During the ATLAS normal operations the cosmic muons that cross the detector in coincidence with the bunch crossing can generate triggers and therefore be considered as good events. We will see how and when it is possible to distinguish the cosmic muons from the "good" muons deriving from the collision between the bunches exploiting only the Resistive Plate Chambers timing.
The sixth chapter deals with the development of an algorithm for the reconstruction of the decay vertices that exploits the muon tracks identified from the muon spectrometer alone. This study is framed within a theory beyond the Standard Model which predicts the existence of neutral long lived particles that decay in some cases in one or more μ^+ μ^- pairs.

Chapter 1

LHC and ATLAS

1.1 The Large Hadron Collider

The most important parameters for a collider are the mass center energy ($\sqrt{s}$) and Luminosity (L). The last is a measurament of the number of collisions per cm^2 and per unit time. Bigger is the L higher is the probability that an event occurs. It can be expressed as

$$L = \frac{n_b N_1 N_2 f_{rev}}{4\pi(\sigma^*)^2} F$$

where n_b is the number of bunches, N_1 and N_2 are the numbers of particles per bunch, f_{rev} the revolution frequency, $(\sigma^*)^2 = \sigma_x \sigma_y$ the transverse beam area so $4\pi\sigma^{*2}$ the effective collision section and $F = \left(1 + \frac{\theta_c \sigma_z}{2(\sigma^*)^2}\right)^{1/2}$ the geometrical luminosity factor. Fig 1.1 is a particle bunches collision illustration, where in evidence are show the effective collision section and the crossing angle θ_c.

σ^* is related to normalized transverse emittance (ϵ_n) and amplitude function at interaction point (β^*) by $\sigma^* = \left(\frac{\epsilon_n \beta^*}{\gamma_r}\right)^{1/2}$, where γ_r is the relativistic factor. These quantities depend on the bunches preparation and on the magnet configuration and powering. A low emittance particle beam is a beam where the particles are confined to a small distance and have nearly the same momentum meanwhile a β^* low implies a narrower beam.

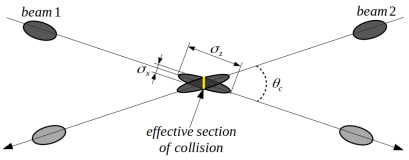

Figure 1.1

To date the biggest and most powerful particle collider in the world is the Large Hadron Collider (LHC), installed in the 26.7 km tunnel that was constructed for the CERN LEP machine.
The LHC accelerates and collides protons as well as heavy ions (e.g. lead ions, mixed proton - lead or Xe - Xe). The acceleration process involves a several number of smaller accelerators prior to the LHC in order to increase gradually the energy of the particles.
Since 2010 the LHC provides collisions to the experiments installed along its circumferences in corrispondence of four Interaction Region (IR): ALICE, ATLAS, CMS, LHCb. The ALICE experiment is mainly devoted to research in heavy-ion physics and Quark Gluon Plasma formation, whereas LHCb is primarily designed to investigate the decays of B-particles and so provide an insight into the phenomenon of CP-violation. ATLAS and

CMS are high luminosity experiment, therefore designed to see a wide range of particles produced in LHC collisions (Fig 1.2).

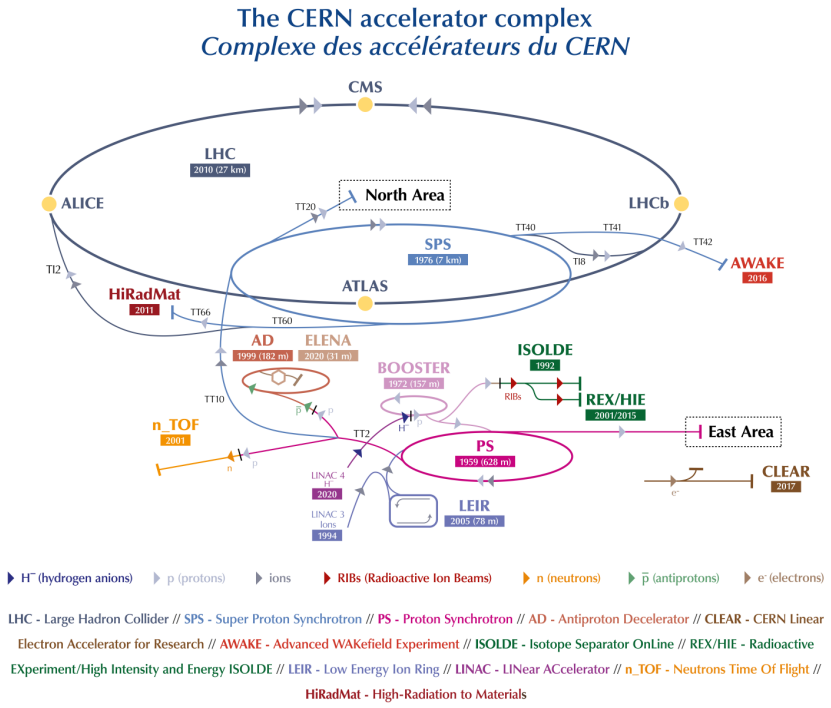

Figure 1.2: LHC complex sketch.

Table 1.1 is a summary of the main machine performance parameters for p-p operation relating to year 2012 of RUN 1 and year 2018 of RUN 2, as well as the expectation parameters value for RUN 3 and for the High Luminosity upgrade (HL-LHC). The parameters are referred to IR1 where is located the ATLAS experiment. [31] [9] [54]

Performance parameter	Design	RUN 1	RUN 2	RUN 3	HL-LHC
$\sqrt{s}$ (TeV)	14	8	13	14	14
bunch spacing (ns)	25	50	25	25	25
bunch intensity (10^{11} ppb)	1.15	1.6	1.0 - 1.25	up to 1.8	2.2
n_b	2800	1380	2556	2800	2800
ϵ_n (μm)	3.5	2.5	1.9	2.5	2.5
β^* (cm)	55	60	30 - 25	30 - 25	down to 15
θ_c (μrad)	285	170	320 - 260	300 - 260	-
L_{peak} (10^{34} cm^{-2} s^{-1})	1	0.77	2.1	2	5 - 7

Table 1.1: Main machine performance parameters for p-p operation for RUN 1 and 2 and the expectation parameters value for RUN 3 and HL-LHC

1.2 ATLAS Overview

Being a high luminosity experiment the ATLAS detector was developed following construction criteria such as:

- Fast and radiation-hard electronics and sensor elements;
- High detector granularity to handle the particle fluxes and to reduce the influence of overlapping events;
- Large acceptance in pseudorapidity with full azimuthal angle coverage;
- Good charged-particle momentum resolution and track reconstruction efficiency;
- Very good electromagnetic calorimetry for electron and photon identification and measurements, complemented by full-coverage hadronic calorimetry for accurate jet and missing transverse energy measurements.
- Good muon identification and momentum resolution over a wide range of momenta and the ability to determine unambiguously the charge of high p_T muons.
- Highly efficient triggering on low transverse-momentum objects with sufficient background rejection.

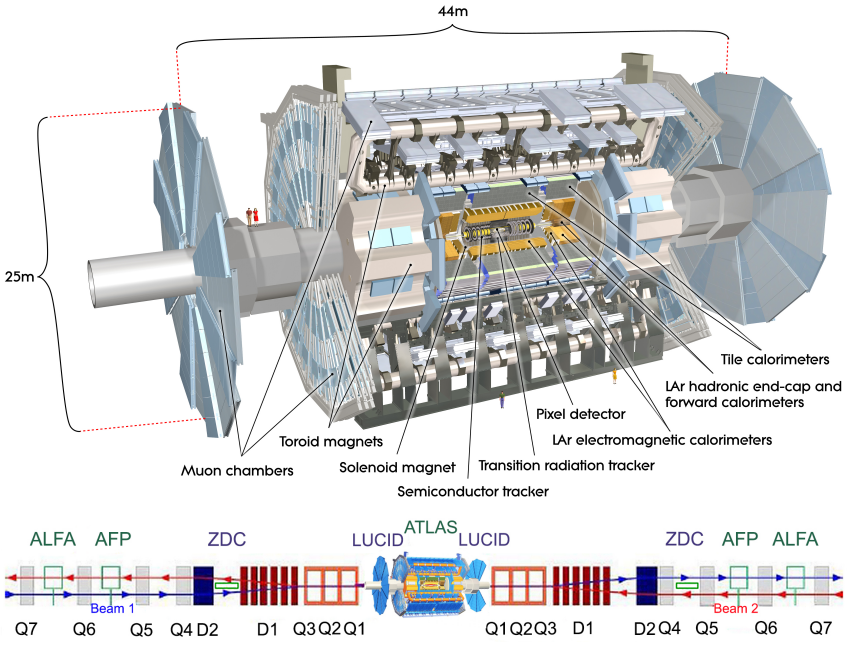

Figure 1.3: At the top a cut view of the ATLAS detector. At the bottom an overview of the forward detectors location.

The overall ATLAS detector layout is shown in Fig. 1.3. It is nominally forward-backward symmetric with respect to the Interaction Point (IP) and it is divided in the barrel region, a cylindrical structure around the beam pipe, and two end-cap regions closing the barrel along the beam pipe with all detector sub-systems.
Closest to the IP is the Inner Detector (ID). It is formed by four indipendent but complementary sub-detectors: Insertable B-Layer (IBL), Pixel Detector, SemiConductor Tracker

(SCT) and Transition Radiation Tracker (TRT). Most particles, except for muons and neutrinos are absorbed in the calorimeter system, which forms the next detector level to measure the particle energy.
As the only measurable particles emerging from the calorimeter are muons, a dedicated tracking system built from gaseous detectors follows the calorimeter system. The inner and muon tracking system are hosted in a magnet structure to measure the particle momentum from the bending radius in the magnetic field. The collected data is stored in a buffer at the chambers and only written to disk, if the trigger system which analyses part of the measured data online, identifies a potentially interesting event.
In addition to the main ATLAS detector systems, four smaller sets of detectors are being built to provide good coverage in the very forward region. Ordered according to their distance from the interaction point, the first system is a Cerenkov detector called LUminosity measurement using Cerenkov Integrating Detector (LUCID). It is the main relative luminosity monitor in ATLAS and is located at a distance of ±17 m from the IP, near the Target Absorber Secondaries collimator.
The second system is the Zero-Degree Calorimeter (ZDC), located at a distance of ±140 m from the IP. This corresponds to the location where the LHC beam-pipe is divided into two separate pipes. The ZDC is embedded in the TAN (Target Absorber Neutral), located between the beam-pipes just after the split. The ZDC primary purpose is to detect forward neutrons in heavy-ion collisions.

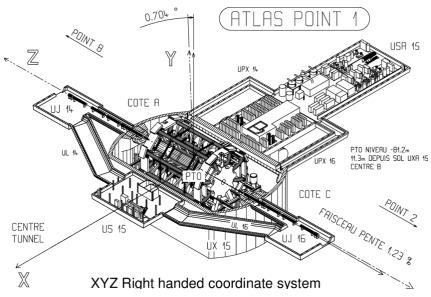

Figure 1.4

Diffractive protons are usually scattered at very small angles (hundreds of micro radians). In order to measure them the ATLAS Forward Proton (AFP) are placed almost symmetrically with respect to the IP at -204 m and +217 m. Stations located closer to the IP contain the tracking detectors, whereas the further ones are equipped with tracking and timing devices.
The most remote detector is the Absolute Luminosity For ATLAS (ALFA) detector. It consists of scintillating-fibre trackers located inside Roman pots at a distance of approximately ±240 m from the IP.
The detector coordinate system is defined as a right-handed system (Fig. 1.4). The nominal IP is defined as the origin of the coordinate system. The positive x-axis is defined as pointing from the nominal IP to the centre of the LHC ring and the positive y-axis is defined as pointing upwards. The z-axis is tangential to the beam pipe. The side-A of the detector is defined as that with positive z and side-C is that with negative z. For physics analysis it is common to work in the cylindrical coordinates frame, defining the azimuthal angle ϕ in the transverse plane around the beam axis and the polar angle θ to the beam pipe. The xy plane forms the transversal plane where are defined the transverse momentum p_T, the transverse energy E_T and the missing transverse energy E_T.
Instead of the the polar angle, the pseudo-rapidity

$$\eta = -ln\Big(\tan\frac{\theta}{2}\Big)$$

is widely used in collider experiments. For massless particles, this quantity converge to the definition of rapidity

$$y = \frac{1}{2} ln \frac{(E + p_z)}{(E - p_z)}$$

where E is the total energy and p_z is the component of the momentum along the beam axis of the particle. The distance ΔR in the pseudorapidity-azimuthal angle space is defined as

$$\Delta R = \sqrt{(\Delta\eta)^2 + (\Delta\phi)^2}$$

[24] [53]

1.2.1 ATLAS Muon Spectrometer

The ATLAS Muon Spectrometer (MS) [25] is designed to triggering and tracking the charged particles that exit from the calorimeter system, i.e. the muons. The peculiarity of the MS consists to provide an accurate and independent measurement of muons momentum reconstructing their tracks (in the pseudorapidity range $|\eta| < 2.7$), and also to provide a muon independent trigger (in the range $|\eta| < 2.4$). To obtain an accurate momentum measurements the MS takes advantage of the magnetic field produced by the air-core barrel toroid and the two air-core end-cap toroids. The barrel toroid covers the pseudorapidity range $|\eta| < 1.4$, the end-cap toroids cover the range $1.6 < |\eta| < 2.7$, while the range $1.4 < |\eta| < 1.6$, called transition region, is covered by a combination of barrel and end-cap fields (see Fig. 1.5).

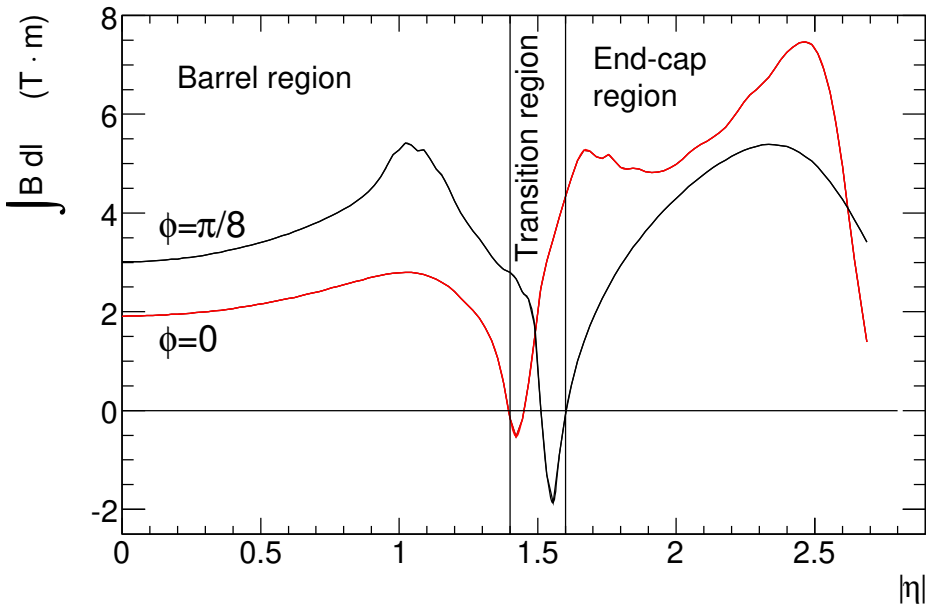

Figure 1.5: The MS integrated magnetic field as a function of $|\eta|$ for the barrel and end-cap regions.

Precision-tracking chambers in the barrel region are located between and on the eight coils of the barrel toroid magnet, while the end-cap chambers are in front and behind the two end-cap toroid magnets. The ϕ symmetry of the toroids is reflected in the symmetric structure of the muon chamber system, consisting of eight octants (Fig. 1.6b). Each

octant is subdivided in the azimuthal direction in two sectors with slightly different lateral extensions, a large and a small sector, leading to a region of overlap in ϕ.

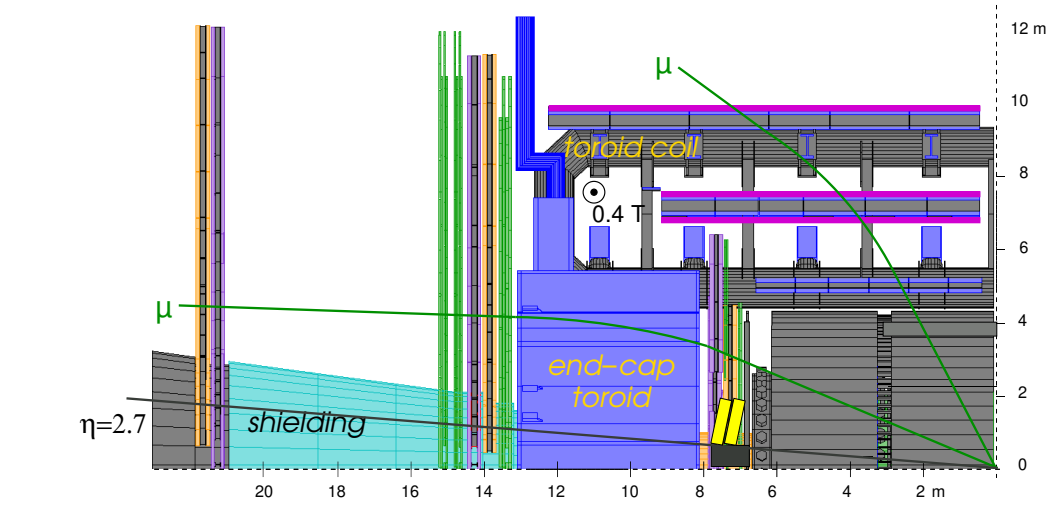

(a)

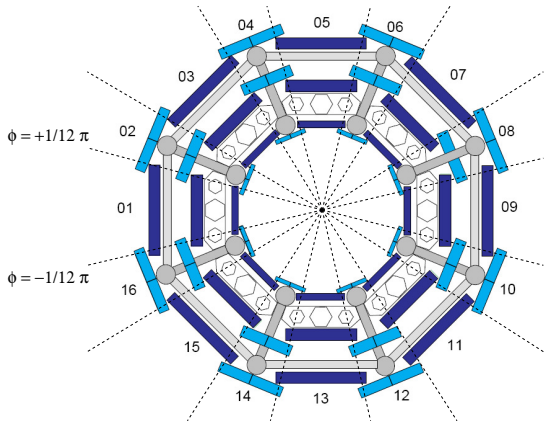

(b)

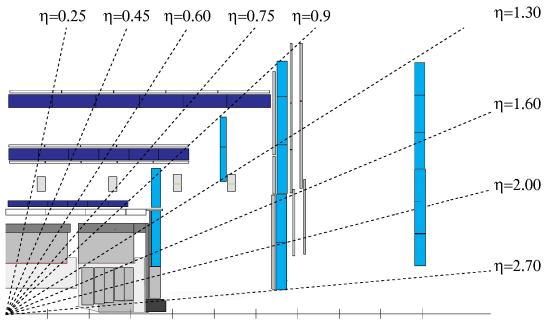

(c)

Figure 1.6: (a): Cross-section of the muon system in a plane containing the beam axis (bending plane). High-momentum muons would propagate along quasi-straight trajectories which are illustrated by the green line and typically traverse three muon stations. (b): Cross-section of the barrel region perpindicular to the beam axis (non-bending plane), showing three concentric cylindrical layers of eight large and eight small chambers. (c): the same of (a) figure but with η coordinate detail.

The chambers in the barrel are arranged in three concentric cylindrical shells around the beam axis at radii of approximately 5 m, 7.5 m, and 10 m. In the two end-cap regions, muon chambers form large wheels, perpendicular to the z-axis and located at distances of $|z| \simeq 7.4$ m, 10.8 m, 14 m, and 21.5 m from the nominal interaction point (Fig. 1.6a). The precision momentum measurement is performed by the Monitored Drift Tube (MDT) chambers, which combine high measurement accuracy, predictability of mechanical deformations and simplicity of construction. These chambers consist of three to eight layers of drift tubes, operating with an Ar/CO_2 gas mixture at an absolute pressure of 3 bar, which achieve an average resolution of 80 μm per tube, or about 35 μm per chamber. In the forward region ($2.0 < |\eta| < 2.7$) at 7.5 m distance from nominal IP, are located the Cathode-Strip Chambers (CSC), used in the innermost tracking layer due to their higher

rate capability and time resolution. The precision-tracking chambers are complemented by a system of fast trigger chambers capable of delivering track information within a few tens of nanoseconds after the passage of the particle. In the barrel region ($|\eta| < 1.05$), Resistive Plate Chambers (RPC) are selected for this purpose, while in the end-cap ($1.05 < |\eta| < 2.4$) Thin Gap Chambers (TGC) are chosen.
RPCs provide up to six position measurements along the muon trajectory in the MS, with a space–time resolution of the order of 2 cm $\times$ 2 ns. Each RPC consists of two independent detector layers (referred to as a doublet), separated by about 2 cm. The RPCs are arranged in three concentric cylindrical doublet layers at radii of approximately 7.8 m (6.8 m), 8.4 m (7.5 m), and 10.2 m (9.8 m) for the small (large) azimuthal sectors. Each single RPC detector layer is constructed from two parallel resistive electrodes which are made bakelite with a high resistivity of approximately 10^{10} Ωcm, that prevents self-sustaining discharges and limits the amount of charge produced in an ionisation event, thus allowing the high-rate operation of RPCs. A thin coat of linseed oil is applied to the inner surfaces of the electrodes in order to ensure their smoothness. The two electrodes are separated by a distance of 2 mm using insulating polycarbonate spacers. The external sides of the resistive electrodes are coated with a graphite paint. A reference voltage of 9.6 kV is typically applied across the two electrodes. The RPCs are continuously flushed with a gas mixture of $C_2H_2F_4/C_4H_{10}/SF_6$ (94.7:5:0.3). Each single RPC layer measures η and ϕ coordinates using orthogonal copper strips placed on opposite sides of the electrodes, with the strip widths varying in a range between 24.5 and 33.3 mm. Muon sagittae due to the magnetic field are measured by η strips, aligned perpendicularly to the bending (r-z) plane.

1.2.2 The L1Muon Barrel System for RUN 2

The Trigger and Data Acquisition (TDAQ) system [27] is an essential component of the ATLAS experiment as it is responsible for deciding in real time whether to record data from a given collision. Events are selected using a two levels trigger system called Level-1 (L1) and High-Level Trigger (HLT). Fig. 1.7 shows a flow diagram of the trigger and data acquisition.
The L1 is a hardware-based system using information from the calorimeters (L1Calo) and MS (L1Muon). It defines one or more Region-of-Interest (RoI), i.e. geometrical regions of the detector, identified by (η, ϕ) coordinates, containing interesting physics objects that can be investigated by the second trigger stage. The L1 trigger reduces the event rate from the LHC bunch crossing rate of approximately 30 MHz to 100 kHz. The decision time for a L1 accept is 2.5 μs, while the HLT reduces the 100 kHz rate from the L1 to approximately 1 kHz on average within a processing time of about 200 ms.
L1Calo uses reduced calorimeter information to identify jet, e/γ and τ candidates, as well as missing transverse energy E_T and total energy. The calorimeters measure energy deposited in small cells of various sizes down to a granularity in $\Delta\eta \times \Delta\phi = 0.025 \times 0.025$. L1Calo do not use the full calorimeter granularity but uses collections of calorimeter cells projecting back to the nominal interaction point, called "trigger towers", in regions of granularity ranging from 0.1×0.1 (central regions) up to 0.4×0.4 (forward regions).
The L1Muon barrel trigger system uses the RPCs to identify a RoI containing a muon candidate in the pseudorapidity range $|\eta| < 1.05$. A typical RoI has $\Delta\eta \times \Delta\phi$ dimensions of approximately 0.1×0.1. The L1 trigger assigns muon candidates to the correct LHC bunch crossing and determines the muon transverse momentum (p_T) using six pro-

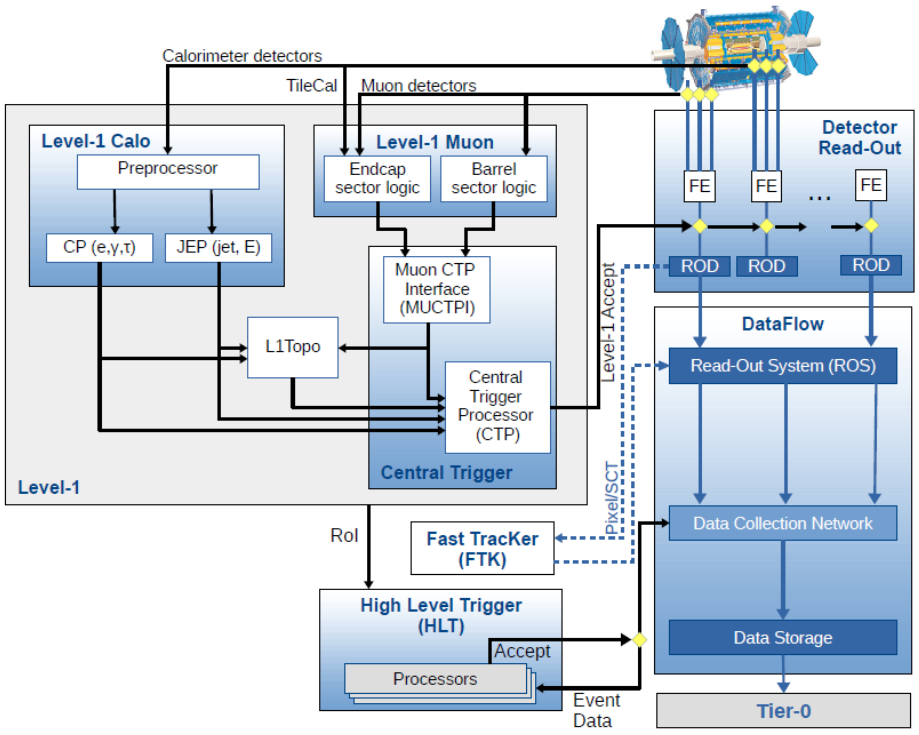

Figure 1.7: The ATLAS TDAQ system in Run 2 showing the components relevant for triggering as well as the detector read-out and data flow.

grammable thresholds. To compensate for different signal propagation times due to the different lengths of readout cables, timing response of RPC electronics channels are calibrated using programmable delays in steps of 3.125 ns, corresponding to an eighth of the LHC bunch spacing. One calibration constant is used for each group of eight channels. The transverse momentum of muon candidates is measured by the L1 muon barrel trigger using different algorithms for low-p_T and high-p_T triggers, as illustrated in Fig. 1.8. The low-p_T algorithm starts with a signal in an RPC2 (pivot) layer and then checks for matching signals in RPC1 (confirm) layer within a narrow cone or road pointing back to the IP. The low-p_T algorithm requires signals to be present in three out of four detector layers, which results in a significant suppression of random coincidences due to background events. The high-p_T algorithm starts with a muon candidate identified by the low-p_T algorithm and then checks for the presence of matching signals in one of the two RPC3 (confirm) layers within a narrower cone pointing back to the IP.
Three low-p_T thresholds and three high p_T thresholds were defined for the L1Muon barrel trigger system. In 2015–2018, the low-p_T trigger thresholds were $p_T = 4$, 6 and 10 GeV, i.e. MU4, MU6, MU10. In 2015–2016, the high-p_T trigger thresholds were $p_T = 10$, 15 and 20 GeV (MU10, MU15, MU20). In 2017–2018, the MU15 trigger was removed, and the MU21 trigger was introduced. The MU21 trigger was identical to the MU20 trigger except that the so-called new feet RPCs were not included in its trigger logic. These new feet chambers were installed as a fourth RPC doublet layer (RPC4) in ϕ sectors 12 and 14, which contain the ATLAS detector support structures [28]

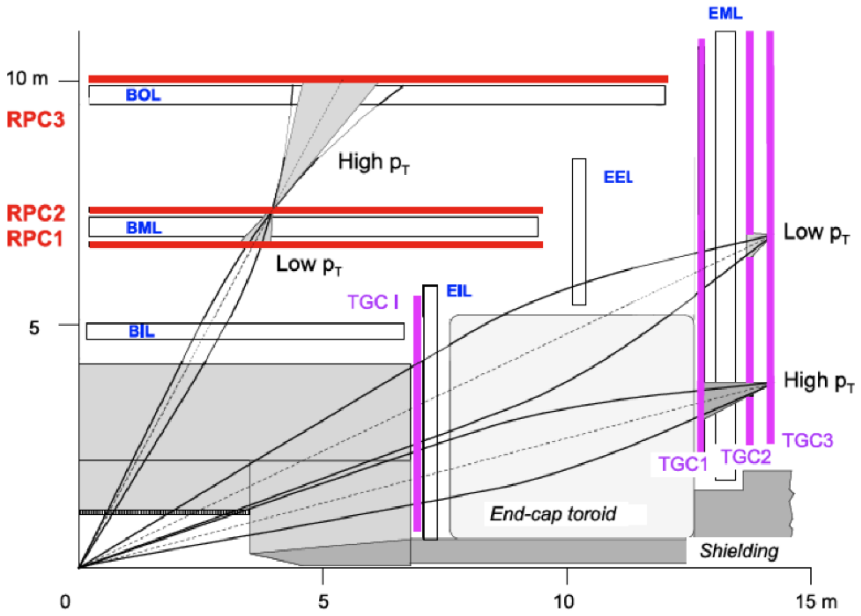

Figure 1.8: Longitudinal ATLAS cross-section. RPCs stations in red. RPC2 is the pivot plane. The MDT chambers are named in blue.

1.2.3 Stand-alone and Global Muon Spectrometer Track Reconstruction

The reconstruction of stand-alone tracks in the MS starts with the identification of short straight-line local track segments reconstructed from hits in an individual MS station. Segments are identified in the individual stations by means of a Hough transform [41]. Segments in the different stations are combined into preliminary track candidates using a loose pointing constraint based on the IP and a parabolic trajectory that constitutes a first-order approximation to the muon bending in the magnetic field. Finally, a global χ^2 fit of the muon trajectory through the magnetic field is performed, taking into account the effects of possible interactions in the detector material as well as the effects of possible misalignments between the different detector chambers.
Global muon track reconstruction is performed using information from the ID and MS as well as the calorimeters [26]. The reconstruction proceeds according to five main reconstruction strategies, leading to the corresponding muon types:

- Combined muons. They are identified by matching MS tracks to ID tracks and performing a combined track fit taking into account the energy loss in the calorimeters.
- Segment-tagged muons. They are ID tracks which are extrapolated to the MS. These tracks are usually associated to track segments in the first layer of the MS that were not used in the reconstruction of a full track in the MS. The segment-tagged muons improve the total reconstruction efficiency since they correspond to low-p_T muons which do not reach the middle and outer stations due to bending effects of the magnetic field.
- Calorimeter-tagged muons. They are ID tracks which are reconstructed in a region with no coverage from the MS. This is a small region around $\eta < 0.1$. ID tracks associated with an energy deposit in the calorimeter which is consistent with a minimum ionizing particle, are considered as muon candidates.

- Extrapolated muon spectrometer muons. If a MS track cannot be matched to an ID track, its parameters are extrapolated to the beamline and used to define an extrapolated muon spectrometer muon. Such muons are used to extend the acceptance outside that of the ID, thus fully exploiting the full MS coverage up to $|\eta| = 2.7$.

- Inside-out combined muons. They are reconstructed using a complementary inside-out algorithm, which extrapolates ID tracks to the MS and searches for at least three aligned MS hits to be used in a combined track fit. This algorithm does not rely on an independently reconstructed MS track, and therefore recovers some efficiency, e.g. in regions of limited MS coverage and for low-p_T muons which may not reach the middle MS station.

Chapter 2

MICROMEGAS Operating Principles and the New Small Wheel Project

2.1 Standard Micromegas

The detection of particles is based on their energy deposit within the active medium of the detector. The dominant mechanisms for energy deposition is the electromagnetic interaction since the electromagnetic cross sections dominate by orders of magnitude over the other cross sections (weak, strong or gravitational). Five different electromegnatic interaction mechanisms of charged particles are used in gas detectors: ionization, excitation, production of Cherenkov radiation, bremsstrahlung and production of transition radiation. The detection mechanism in the MICRO-Mesh GAseous Structure (MICROMEGAS or MM) is the ionization of the gas mixture, tipically Ar based, at a pressure slightly greater than the atmospheric one (1015-1016 mbar) by traversing particles or radiation. MM, developed for the first time by Giomataris et al. in 1996 [18], is a parallel plates chamber belongs to the Micro-Pattern Gaseous Detector (MPGD) family [33] designed to stand the very high fluxes of modern particle and nuclear physics. It consists of a stack of one ionization and one proportional chamber. A metallic micro-mesh separates the two communicating regions, where two different electric fields establish respectively a charge drift and a charge multiplication regime.
The micro-mesh is kept at a distance of few mm from the drift electrode forming the conversion/drift gap and at a distance of few 100 μm from the read-out electrode, by means of small insulating spacers (pillars) 50/120 μm height, forming the amplification gap.
A small amplification gap permits the fast evacuation of ions and to achieve larger electric fields through the Paschen law, and then larger gains. The electric field between the mesh and the read-out electrode E_A is held at a large value (of order of 40-50 kV/cm), while the electric field between the mesh and the drift electrode E_D is much lower (of order of 0.2-1.0 kV/cm) as shown in Fig. 2.1.
The intense E_A pulls down the mesh so the amplification gap width and its uniformity are defined by the height of the pillars and by the mesh mechanical tension.
Traversing charged particles ionize the noble gas based mixture in the drift gap of the detector. Produced electron-ion pairs are separated by the electric field in the drift region. Electrons produced in the primary ionization drift toward the micro-mesh and are sucked in the holes due to the strong E_A. The electron mesh trasparency depends on the characteristics of the mesh such as wire diameter and pitch, but above all on the ratio

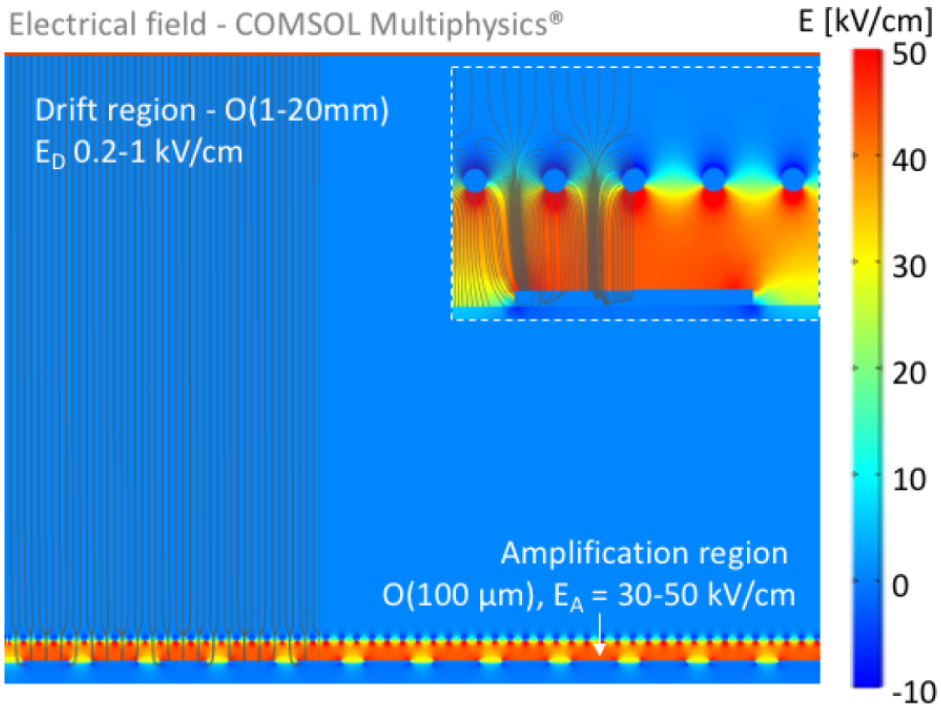

Figure 2.1: Electric field lines simulation in a MM detector [42].

E_A/E_D. It is observed that for ratios greater than 50 the transparency is maximum and almost independent of the mesh characteristics. Once in the amplication gap, electrons are accelerated and gain enough energy between two collisions to further ionize the gas and to starting an avalanche process. The electrons are collected in a few ns in the anode plane, while the ions slowly drift back to the micro-mesh, both inducing a signal on the read-out electronics. Because of the field asymmetry, the vast majority of the upcoming ions doesn't experience the "tunnel" effect as primary electrons do, and is collected by the micro-mesh. The charge evacuation time is then determined by the drift time of ions in the amplication gap, typically 100 ns.

2.1.1 Energy Loss by Ionization for heavy charged particles

The mean energy loss (or stopping power) of a heavy charged particle like muon or hadron with matter is mainly due to inelastic scattering between the incident particle and the atoms that form the target. In these collisions, energy is transferred from the particle to the atom causing an ionization or excitation of the latter. The transferred energy is described by the well known Bethe-Block formula

$$\left\langle \frac{dE}{dx} \right\rangle = -4\pi {r_e}^2 m_e c^2 \rho N_A \frac{Z z^2}{A\beta^2}\left(\frac{1}{2} ln \frac{2m_e c^2 \beta^2 \gamma^2 T_{max}}{I^2} - \beta^2 - \frac{\delta}{2} - \frac{C}{Z}\right)$$

r_e is the electron classical radius, m_e its mass, c the speed of light, ρ the density of the target material, N_A the Avogadro costant, Z the target material atomic number, z the incident particle charge, A the target material atomic mass, β the velocity of incident particle, γ the Lorentz factor, $T_{max} \simeq 2m_e c^2 \beta^2 \gamma^2$ the maximum kinetic energy transferable to an electron in a single collision, I the mean excitation energy, δ corrects for the density effect and C/Z accounts for shell corrections due to the structure of the atom.

This formula exhibits in particular a minimum around $\beta\gamma = 3$ corresponding to Minimum Ionizing Particles (MIPs).
For compounds or mixtures a good approximate mean energy loss value can be found by avereging dE/dx over each element in the compound weighted by the fraction of electrons belonging to each element. Thus

$$\frac{1}{\rho}\left\langle \frac{dE}{dx} \right\rangle = \frac{w_1}{\rho_1}\left\langle \frac{dE}{dx} \right\rangle_1 + \frac{w_2}{\rho_2}\left\langle \frac{dE}{dx} \right\rangle_2 + \ldots$$

where w_1, w_2, ... are the fractions by weight of elements 1, 2, ... in the compound. The mean energy loss of a singly charged particle in an $ArCO_2$ (93:7) gas mixture at normal temperature and pressure using previous equations is shown in Fig. 2.2.

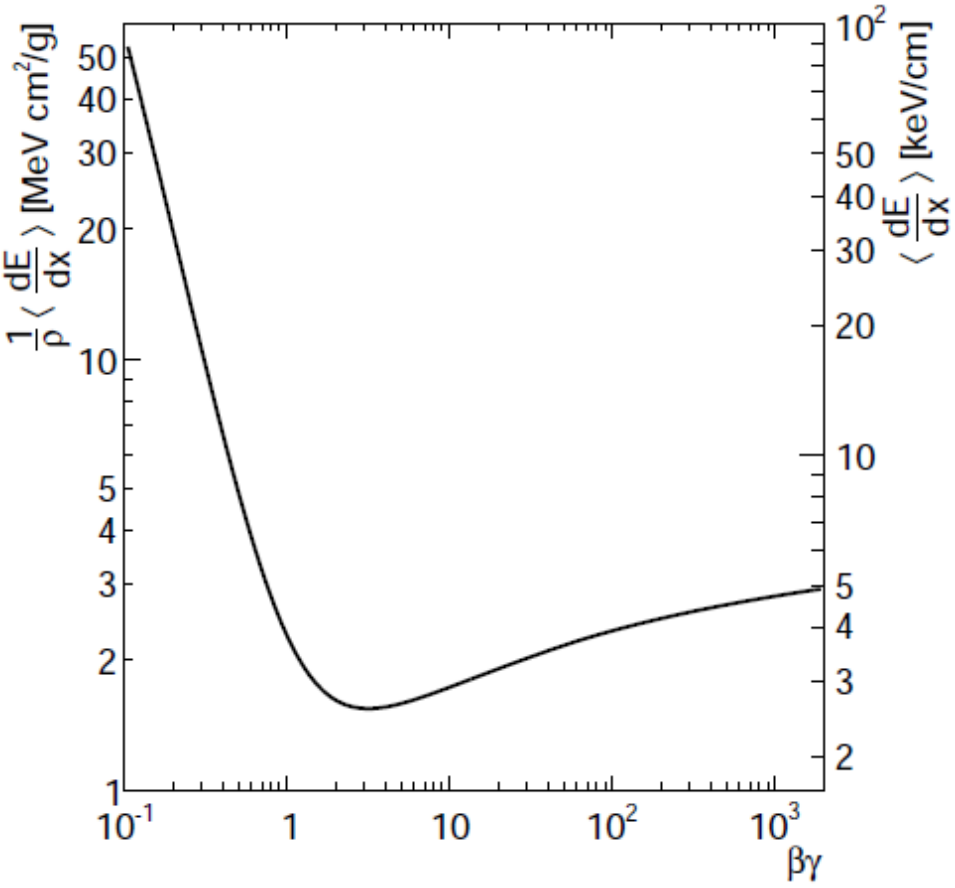

Figure 2.2: Mean energy loss of a singly charged particle in an $ArCO_2$ (93:7) gas mixture at 20 C and 1013 mbar in the range $0.1 \leq \beta\gamma \leq 2000$. [21].

The mean energy loss decreases approximately like $1/\beta^2$ for $\beta\gamma \leq 1$ and has a minimum with only small variations for $2 \leq \beta\gamma \leq 8$. For almost all materials, the mean energy loss of MIPs is on the order of 3 keV/cm. For increasing $\beta\gamma$ the mean energy loss rises like $\ln(\beta^2\gamma^2)$ and reaches the so called Fermi plateau $\beta\gamma \leq 500$.
The ionization yield i.e. the total number of produced electron-ion pairs can then be calculated from the mean energy loss ΔE in the active area of the gas detector

$$n_{tot} = \frac{\Delta E}{W_I}$$

where W_I is the mean ionization energy. W_I is for most materials more than twice as high as the ionization potential, since energy is lost due to excitation of the gas atoms or molecules [5], [43].

Gas	density (g/cm^3)	E_I	W_I	N_p (cm^{-1})	N_t cm^{-1}	$(dE/dx)_{MIP}$ (keV/cm)
Ar	1.662	15.76	26	23	94	2.44
CO_2	1.84	13.78	33	35.5	91	3.01
iC_4H_{10}	2.51	10.57	23	84	195	5.93

Table 2.1: Compilation of physical properties of some gases at standard pressure and temperature. N_p is the number of electron-ion pairs due to primary ionization.

2.1.2 Multiple Coulomb Scattering

In addition to inelastic collisions with the atomic electrons, charged particles passing through matter also suffer repetead elastic Coulomb scatterings from nuclei although with a smaller probability. The Coulomb scattering distribution is well represented by the theory of Molire. It is roughly Gaussian for small deflection angles, but at larger angles it behaves like Rutherford scattering, with larger tails than does a Gaussian distribution. The width θ_0 of the Gaussian angular distribution, resulting from multiple scattering of a narrow beam of particles with parallel momenta p and charge number z in a material of thickness x and radiation length X_0 is given by

$$\theta_0 \;=\; \frac{13.6\ MeV}{\beta cp} z \sqrt{\frac{x}{Z_0}} \left(1 \;+\; 0.038\ \ln\left(\frac{x}{X_0} \right) \right)$$

The angular scattering can be translated into a transverse broadening of the particle beam. Its width after a distance d to the scattering object is approximated by

$$\Delta y \;=\; \frac{\theta_0}{\sqrt{3}} d$$

For a composite scatterer, consisting of layers of materials with different radiation lengths X_i, densities ρ_i and thickness d_i, the resulting radiation length can be calculated as

$$\frac{1}{X_0} \;=\; \sum_i \frac{w_i}{X_i}$$

where w_i is the i-material weight fraction $w_i \;=\; d_i\rho_i / \sum_j d_j\rho_j$ [38].
MM are tracking detectors, therefore it is essential to minimize the presence of material so as to minimize the track particle degradation.

2.1.3 Electrons and Ions Transport in Gases

In the absence of an electric field, elctrons and ions liberated by passing charged particle diffuse uniformly outward their point of creation. In the process they suffer multiple collisions with the gas molecoules loosing their energy and quickly reach thermal equilibrium with the gas and eventually recombine. In the presence of electric field $\vec{E}$ the electrons and ions drift in opposite direction and diffuse towards the electrodes. The scattering cross section is determined by the details of atomic and molecular structure. Therefore,

the drift velocity and diffusion of electrons depend very strongly on the nature of the gas, specifically on the inelastic cross-section involving the rotational and vibrational levels of molecules. In noble gases, e.g. Ar, the inelastic cross section is zero below excitation and ionization thresholds. Large drift velocities are achieved by adding polyatomic gases (e.g. CO_2 and/or iC_4H_{10}) having large inelastic cross sections at moderate energies. Another principal role of the polyatomic gas is to absorb the ultraviolet photons emitted by the excited noble gas atoms, so acting as quenchers. Fig. 2.3 shows the photo-absorption cross section for Ar and other polyatomic gases like CO_2 and iC_4H_{10} as a function of the photon energy.

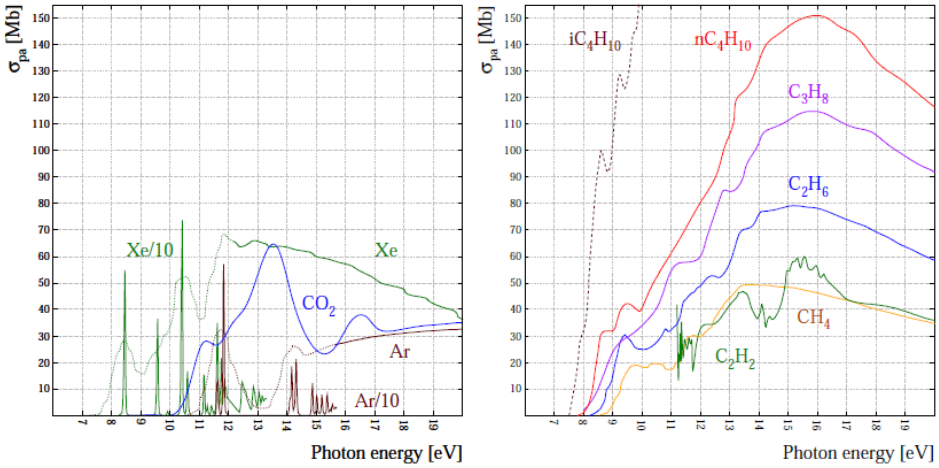

Figure 2.3: Photo-absorption cross section for argon and other polyatomic gases [8].

In the presence of an external magnetic field $\vec{B}$, the Lorentz force acting on electrons between collisions, deflects the drifting electrons and modifies the drift properties. Analitically the electrons drift velocity is given by

$$\vec{v}_d = \frac{e}{m_e}\frac{\tau}{1+\omega^2\tau^2}\left(\vec{E} + \frac{\omega\tau}{B}(\vec{E}\times\vec{B}) + \frac{\omega^2\tau^2}{B^2}(\vec{E}\cdot\vec{B})\vec{B}\right)$$

where $\omega = eB/m_e$ is the Larmor frequency and τ the mean time between two collisions with gas atoms. From the last equation we can observe that:

- $\vec{B} = 0$. The electrons follow on average the electric field lines;
- $\vec{E}\cdot\vec{B} = 0$. The $\vec{E}\times\vec{B}$ term leads to a drift component perpendicular to the fields, such that the drift velocity vector spans the so called Lorentz angle $\alpha_L = \arctan(\omega\tau)$ with the electric field vector. This effect leads to a systematic shift of hit positions with perpendicularly incident particles and compresses or disperses the detected charge distribution for inclined tracks;
- $\vec{E}\cdot\vec{B} \neq 0$. There is a drift component into the direction of the magnetic field. For large magnetic fields, i.e. $\omega\tau >> 1$ the net drift vector may even point into the same direction as magnetic field. Diffusion of electrons perpendicular to the magnetic field is strongly suppressed, as the field forces the electrons on a helix around the magnetic field lines.

In practice, the interaction of the electron with gas molecules is very complex and the parameters that characterize its diffusion and drift are calculated numerically using the

MAGBOLTZ [19] algorithm. Fig. 2.4 shows the electron drift velocity as a function of the electric field strenght E for two gaseous mixture, i.e. Ar/CO_2 (93:7) and $Ar/CO_2/iC_4H_{10}$ (93:5:2) at 1015 mbar pressure and 293.15 K temperature, calculated using MAGBOLTZ. The magnetic field $\vec{B}$ is assumed to be 0. The electric field intensity varies from 0.1 to 1 kV, characteristic of MM detectors drift gap. For 0.1 kV/cm $\leq$ E $\leq$ 0.5 kV/cm the gaseous mixture containing the iso-butane has a slightly higher v_d than that relative to the other mixture. The maximum v_d value is obtained for electric field values close to 0.5/0.6 for both mixtures. For these values the two velocity are almost equal.

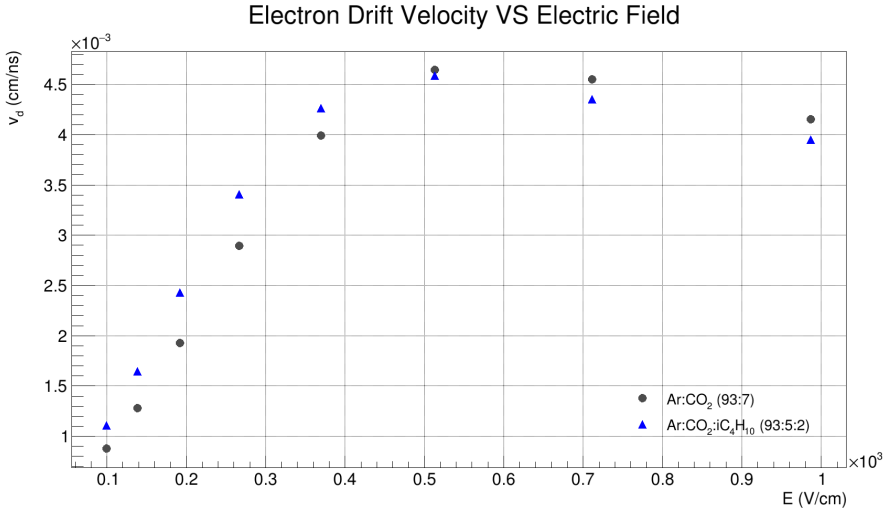

Figure 2.4: Drift velocity v_d as a function of electric field strength for two gaseous mixture at 1015 mbar pressure and 293.15 K temperature.

In weak electric fields the drift velocity of ions u_d depends linearly on the electric field E:

$$u_d = \mu E$$

where K is the ion mobility, which is a property of the gas mixture. Blanc[20] found that the mobility of ions in gaseous mixtures, obeyed a simple linear relationship which can be expressed as follows:

$$\frac{1}{\mu(I^+, AB...N)} = \sum_k \frac{f(k)}{\mu(I^+, k)}$$

where $\mu(I^+, AB...N)$ is the mobility of ion I^+ in a mixture of gases AB...I...N, $\mu(I^+,k)$ the mobility of ion I^+ in gas k and f(k) the concentration of gas k in the mixture. For very low gas concentrations ($\leq 3\%$) the Blanc linear reletionship is no longer followed and the mobility of the mixture is well described by the other components with higher concentration. The table 2.2 shows the mobility values of some gases at normal temperature and pressure.

2.1.4 Avalanche Multiplication

Multiplication in gas detectors occours when the primary ionization electrons gain sufficient energy from the accelerating high electric field to also ionize gas molecules. The resulting secondary electrons then produce tertiary ionization and so on. This results in

Gaseous mixture	Ion	μ ($cm^2/(V\ s)$)
Ar	Ar^+	1.54
Ar:iC_4H_{10}	$C_4H_{10}^+$	0.61
Ar:iC_4H_{10}	Ar^+	1.56
Ar:CO_2	Ar^+	1.72
Ar:CO_2	CO_2^+	1.09

Table 2.2: Ions mobility for some gaseous mixture at normal pressure and temperature. [52]

the formation of an avalanche. Because of the greater mobility of the electrons wrt the positive ions, the avalanche has the form of a liquid drop, with the electrons grouped near the head and the slower ions trailing behind.
Assuming n_0 electrons entering the high electric field region between cathode and anode of a detector, the total number of electrons after a path length x is given by

$$n = n_0 \exp(\alpha x)$$

where $\alpha = 1/\lambda$ is the probability of an ionization per unit path lenght dx, i.e. the first Townsend coefficient and where we have assumed attachment, photo-production and space charge effects negligible. From the last relation we can extract the multiplication factor G or gas gain

$$G = \frac{n}{n_0} = \exp(\alpha x)$$

Phisically the multiplication factor is limited to about $G \leq 10^8$ or $\alpha x \leq 20$ after which breakdown occours, i.e. Raether limit exceed. Fig. 2.5a shows the Townsend coefficient as a function of the applied electric field for two gaseous mixture, i.e. Ar/CO_2 (93:7) and $Ar/CO_2/iC_4H_{10}$ (93:5:2) at 1015 mbar pressure and 273.15 K temperature, calculated using Magboltz.

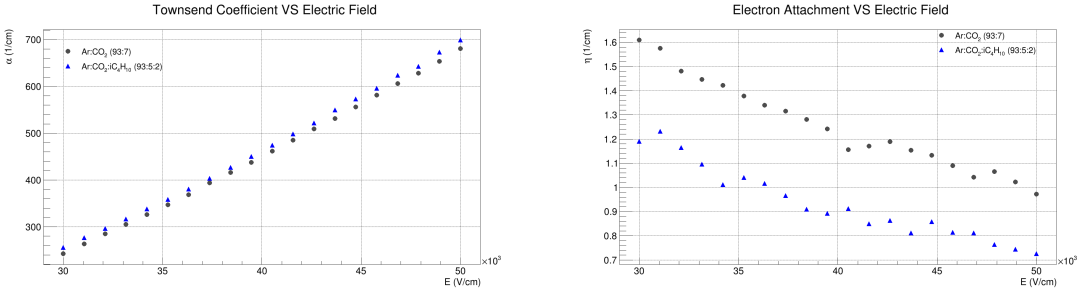

(a) (b)

Figure 2.5: (a): first Townsend coefficient α as a function of the amplification electric field for two gaseous mixture at 1015 mbar pressure and 273.15 K temperature, calculated using MAGBOLTZ. Penning transfer not taken into account. (b): the attachment coefficient for the same gas mixture.

In the electric field range considered ([30-50] kV/cm) , an increase in the coefficient and therefore also in the gain directly proportional to the applied electric field is observed for both mixtures. In particular, α is slightly greater in the case of the mixture containing

iso-butane.
Electron multiplication in gaseous mixture sometimes far exceeds the gain calculated using Townsend coefficients alone. This is most notably the case if a gas with a low ionisation potential (e.g. polyatomic gases) is added to a gas with higher energy excited states (e.g. Ar). The additional gain is accounted for by the transformation of excitation energy into ionisations ($A^* + B \rightarrow A + B^+ + e$). It can occur if the excited state A^* has an energy level above the ionization threshold of B and a lifetime sufficiently long to cause the energy transfer before de-exciting via other channels. The gain enhancement is named "Penning effect" [29].
Electrons can also form negative ions through collisions with atoms. This process is characterized by the attachment coefficient η (Fig. 2.5b), defined as the probability to form such a negative ion in a collision. The value of η strongly depends on the gas electron affinity. It is minimal for noble gases because of their full valence shell. On the other hand, air and water vapor have large attachment coefficient, and concentrations as small as a few ppm can signicantly degrade the charge collection, even in the presence of a strong electric field.

2.1.5 Discharges in Micromegas

At gaseous mixture pressures close to atmospheric one the dominant mechanism of discharge is a fast, photon-mediated transition from proportional multiplication to streamer, followed by breakdown. When the total charge in the avalanche exceeds a value in the range between 10^7 and 10^8 electron-ion pairs, i.e. Raether limit, the enhancement of the electric field in front and behind the primary avalanche is such as to induce the fast growth of secondary avalanches, and the appearance of a long, filament-like forward and backward charge propagation named streamer. In a uniform, strong electric field, the streamer propagates all the way through the gap. The outcome of the process is the creation of a densely ionized, low-resistivity channel between anode and cathode, inevitably leading to discharges as e.g. the sparks. Fig. 2.6 shows a positive streamer formation.
Sparks might affect the detector response in different ways: reducing its operating lifetime due to intense currents produced in short periods of time, heating and melting the materials at the affected regions; damaging the read-out electronics which have to support huge current loads; increasing the detector dead-time (breakdown). Discharge probability and its intensity are linked to several factors, e.g.: electric field strength , the gas mixture and its density, the presence of contaminants inside the mixture such as water vapour, the presence of dust inside the active medium of the detector, the presence of imperfections on the electrode surfaces, etc.. It is clear that zeroing the discharge probability in a detector is impossible, especially for detectors belonging to the MPGD family, such as MM, which aim for high gains by exploiting small amplification gaps and high electric fields. Unable to exclude the occurrence of sparks in the MM detector, the occurrence rate and their effect on the detector can be minimized. The best solution to limit discharge damage and breakdown MM detector consists in adding a resistive layer between the micro-mesh and the read-out strips. This layer is separated from the strips by an insulator, for example a Kapton foil. The signal is then transferred to the read-out elements by capacitive effect, and the charges are evacuated through the resistive layer. When a discharge occurs, the corresponding current leads to a very rapid increase of the resistive element potential which quenches the discharge before any signicant drop of the micro-mesh potential [11].

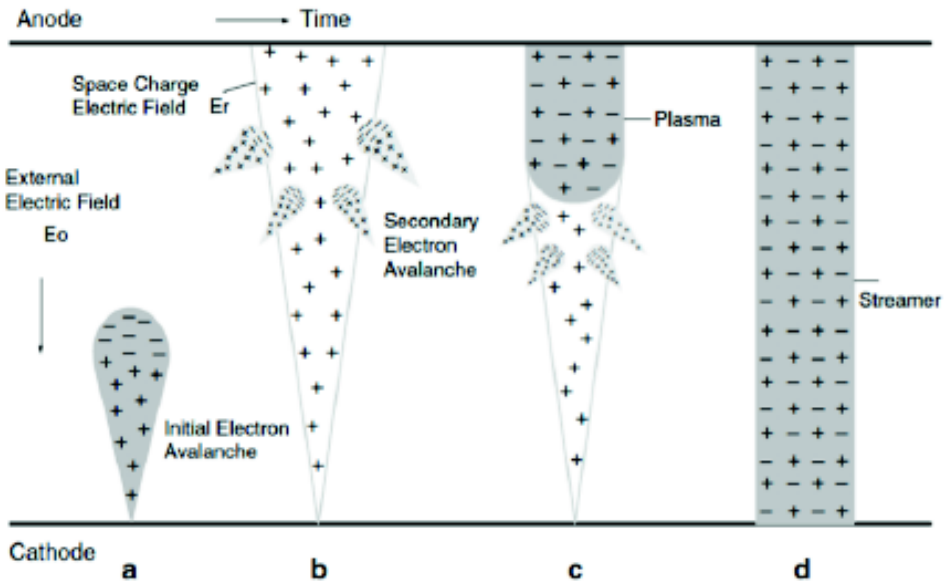

Figure 2.6: A positive streamer formation sketch. Photon radiation generates photo-ionization and so second electron avalanche (b); electrons form negative ions creating a plasma stream (c); when the streamer reaches the cathode, gap breakdown is completed (d).

2.2 MM Chambers for the ATLAS New Small Wheel Project

In order to benefit from the expected high luminosity performance that will be provided by the LHC in RUN 3 and in the HL-LHC era, the first station of the ATLAS MS end-cap system, the so called Small Wheels, located at ± 7 m from the IP and that cover the $1.3 < |\eta| < 2.7$ region, will need to be replaced with the New Small Wheels (NSWs), a more performant detector system capable to operate in a high background radiation region (between 600 Hz/cm^2 and 15 kHz/cm^2). The main NSWs goals are improve the tracking efficiency in the high rate environment and reduce fake triggers from background hits.

The NSW will be composed by two wheels, NSW-A and NSW-C for the forward and backward direction respectivley. Each wheel hosts two different detector technologies: the MM and the small-strip Thin Gap Chambers (sTGC). The sTGC will be primarily devoted to the L1 trigger functions, while providing also tracking information. The MM will be dedicated to precision tracking; it will also provide information on track segments found by the muon end-cap middle station (Big Wheel), improving the trigger capabilities, so the sTGC-MM chamber technology combination forms a fully redundant detector system for triggering and tracking both for online and offline functions. Fig. 2.7 shows the fine structure of a NSW.

The two detector technologies will be overlapping in the fundamental unit of a NSW: a sector. Each wheel will be composed by eight large and eight small sectors. Each sector hosts two WEdges (WE) per detector technology. The smaller sector cover the gap between the larger ones. Each of the 16 sectors will be equipped by a sandwich configuration of four WE sTGC-MM-MM-sTGC.

A MM WE is composed by two modules, as the production of a single piece is mechanically

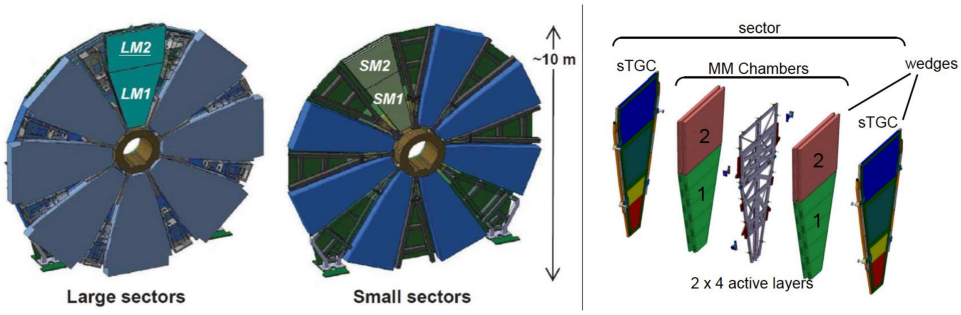

Figure 2.7: (right) An exploded drawing of a NSW where the large and small sector are in evidence. (left) An exploded drawing of a sector.

impossible, SM1 and SM2 for the small WEs and LM1 and LM2 for the large WEs. Each module is a quadruplet (4-plet), thus providing 4 detection layers for position measurements in the radial (precision or ETA) and in the azimuthal (or STEREO) coordinates. The construction of the four types of MM modules (SM1, SM2, LM1, LM2) is shared among four construction sites, 32 modules per type. All modules have trapezoidal shapes with slightly different sizes, ranging from a total active area per layer of about 2 m^2 (SM1, SM2) to about 3 m^2 (LM1, LM2).

2.2.1 SM1 MM Chamber Layout

A MM 4-plet or chamber contains 4 independent singlets of MM detectors. Each chamber is made up by 3 Drift Panels (DP), 2 Outer (ODP) and one Central (CDP) and by two Read Out Panels (ROP), one ETA (ETA-ROP) and one STEREO (STEREO-ROP) organized with a sandwich configuration, i.e. ODP/ETA-ROP/CDP/STEREO-ROP/ODP. The active trapezoidal region of the chamber has a height of 221 cm, a larger base equal to 132 cm and a minor base equal to 50 cm. The chamber thickness is just 8 cm.
Each singlet is constructed with the so-called floating mesh technique. The stainless steel micro-mesh is an integral part of the DP and together with its cathode surface defines the drift volume of the singlet. The amplification volume is defined only when the DP is coupled with the ROP. The mesh used for the construction of all NSW MM singlet is woven wire with a diameter of 30 μm and has openings of 71 μm nominal. The panels are assembled together to form the 4-plet by a series of special screws that cross the entire chamber transversely, passing through the so-called assembly holes arranged along the perimeter of each panel (1 every 10 cm). Furthermore, given the large surface of the 4-plet, four InterConnection (IC) systems (Fig. 2.8b) are provided along the axis of the trapezoidal 4-plet (Fig. 2.8a) in the active region. These systems have been designed in such a way as to keep the thickness of the 4 drift regions of the chamber as close as possible to the nominal one, also reducing the deformation of the external walls of the chamber due to the overpressure of the gaseous mixture.
The DPs and ROPs consist of an aluminum skeleton (internal frame + honeycomb), see Fig. 2.9, with a thickness of about 10 mm on whose faces are glued 5 trapezoidal FR4® sheets of different sizes that support the singlet anodic surface (anode-PCBs) for the ROP or the singlet cathode surface (cathode-PCBs) for the DP. The aluminium skeleton is the best compromise between strength and lightness. The use of materials with a low density, such as honeycomb and aluminum bars for the internal frame, minimizes the loss of energy and Coulomb scattering by the particles passing through the detector. The

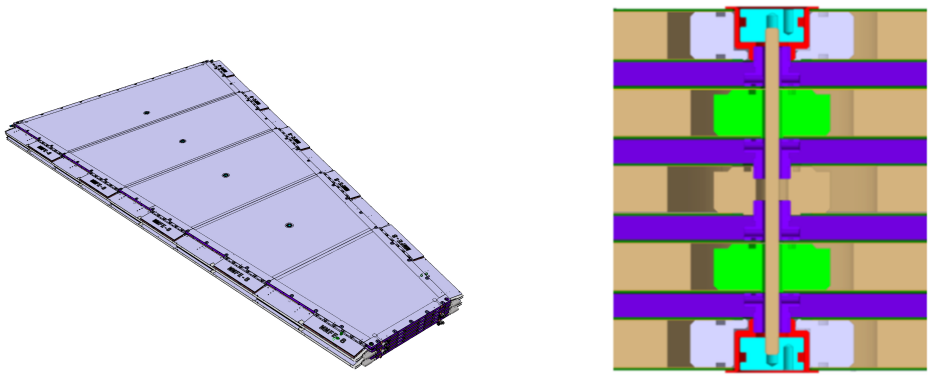

(a) (b)

Figure 2.8: (a): A planar view of the SM1 MM 4-plet. The four holes along the trapezoid axis represent the IC holes. Along the edges are represented the MM Front-End board (MMFE-8), 10 for each read-out layer. (b): A schematic view of a 4-plet IC system. In brown the threaded road that cross trasversally the entire 4-plet connecting the two external end-plugs (in light blue); in green and light violet the IC internal disks for drift and read-out panel respectivley. They are glued to the inside of the panels. In red are represented the IC holders that are glued only on the ODPs in the appropriate seats. In blue are represented the IC spacers.

external chamber sides, represented by the inactive face of the ODPs, are formed by bare FR4 sheets.

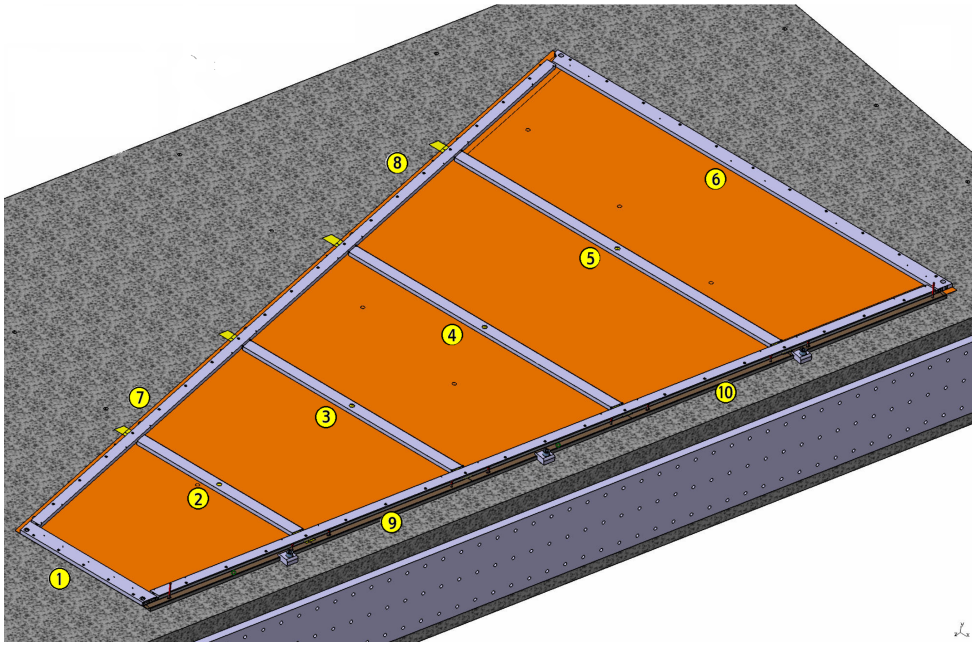

Figure 2.9: Drift and read-out panels internal frame schematic view. It consists of 6 transverse bars (1-6) and 4 lateral bars (7-10). The five trapezoidal regions delimited by the frame bars are filled with five honeycomb trapezoids sheet.

Drift Panel Structure

The cathode-PCBs (see Fig. 2.11 and Fig. 2.12 for a schematic view of an ODP) have a simple structure: on the 0.5 mm thickness FR4 trapezoidal sheet is glued a 17 μm thickness copper foil. On the cathode-PCBs inactive region around the copper surface are fixed the Mesh Frame (MF) and the Gas Gap Frame (GGF). The first, together with the IC spacers, has the purpose of keeping the mesh at a distance of 5 mm from the cathode surface defining the drift region. The second is necessary to define the O-ring (Or) seat. The MF consists of 6 aluminum profiles and 4 corners that run parallel to perimeter of the DP at a distance of 19 mm from its edges. Fig. 2.10 shows a MF profile cross section. The upper surface of the profile has parallel knurling. This design is chosen to optimize the bonding of the mesh on the MF. This surface is slightly inclined, i.e. the side of the MF which faces the copper surface is higher than the opposite side and has a nominal height of 5.060 mm

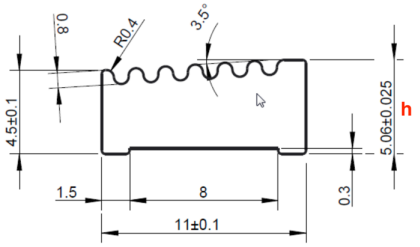

Figure 2.10

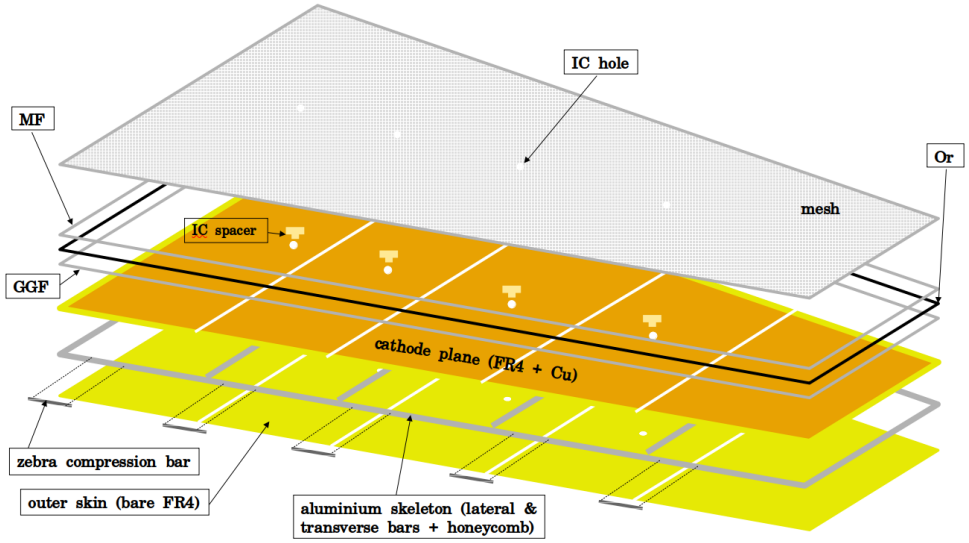

Figure 2.11: An exploded view of an ODP where are represented all the main components except the honeycomb and the IC internal disk. Not to scale.

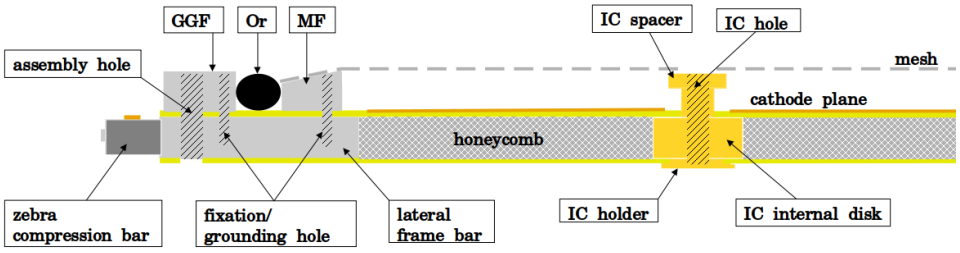

Figure 2.12: An ODP transversal section view. Not to scale.

The MF bottom surface has a 0.3 mm deep groove which, when gluing the MF on the DP, receives the quantity of glue necessary to hold the MF in position under the action

of the tangential force that applies the mesh on the MF. The GGF is constituted also by 6 aluminum profiles and 4 corners. Its cross section is rectangular with width and height equal to (12.1±0.1) mm and (5.2±0.1) mm respectivley. The GGF is fixed at a distance of 7 mm from the MF. The groove between MF and GGF will host the Or, or rather the EPDM ropes with closed skin that has a nominal density of 0.6 g/cm^3, a diameter of (7±1) mm and a length of 5900 mm.
The DPs also house the singlet gaseous mixture inlet/outlet system (see Fig. **??**) and 10 zebra compression bars. For each singlet there are two gas distribution tubes: one connected to the gas inlet and the other to the gas outlet. The tubes run parallel to the DP bases at 1 mm from the MF. The 1071 mm tube has 5 holes of 0.1 mm diameter and it is connected to the gas inlet. The 279 mm tube, on the other hand, has only 3 holes of 0.1 mm diameter and it is connected to the gas outlet. The difference in the number of holes in the inlet and outlet tubes causes an overpressure inside the singlet of about 1/2 mbar. The number of holes and their size have been chosen to make the gas flow inside the gap as uniform as possible and to guarantee the correct gas exchange at each point of the detector (see [13] for more details).
The Zebra compression bars are fixed on the lateral side of the lateral frame bars and have the purpose of pressing the Zebra solder-less connectors against the connector pad regions of the anode-PCBs. The zebra connectors allow the connection between the read-out strips and the MMFE-8 board.
There are two HV connectors for each DP cathode side thus forming a redundant connection to power supply. These are placed along the edge of the skeleton lateral bar.

Micromegas Anode PCB

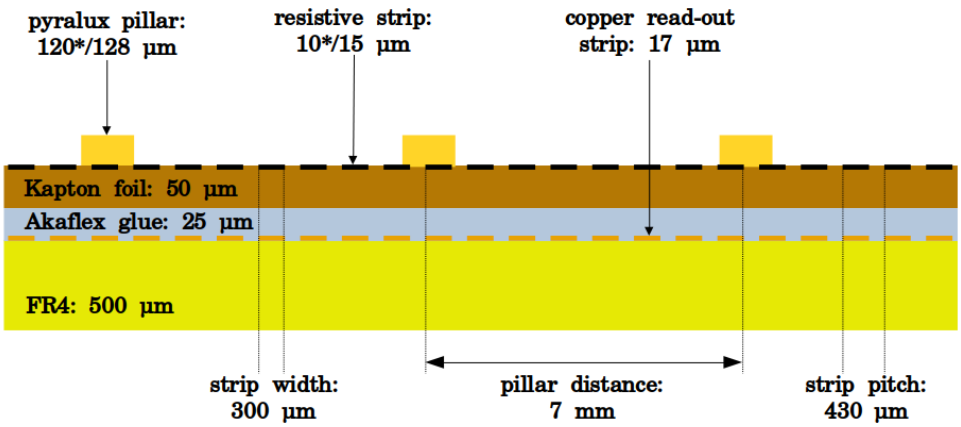

Figure 2.13: Schematic of the SM1 MM anode-PCB layers and dimensions of its main structures. Values marked with an asterisk indicate measured values, other ones nominal values. Not to scale.

The anode-PCBs are a stacked structure of several layers, as shown in Fig. 2.13. The copper read-out structure comprises 1022 read-out strips of 300 μm width and 430 μm pitch, covering the active area of the PCB. The routing of the read-out strips accounts for the positioning of IC without strip cuts or interruptions (Fig. 2.14d). Half of the strips are routed on the left or right to connector pads (Fig. 2.14a) where the signals are transmitted to the front-end electronics via the MMFE-8 board. Additionally the outer borders include, among other features, cross-mark targets for precision holes (Fig. 2.14c),

Rasnik Masks for positioning and dimensions control (Fig. 2.14b), alignment targets and a HV supply line including space for HV filters per side (Fig. 2.14e).
A layer of resistive strips 300 μm width and 10-15 μm height is printed on an insulating Kapton® foil follows the pattern of the read-out strips. High voltage is applied to the resistive layer from the copper pattern via a hole in the Kapton foil. A line of silver polymer ink, called silver line, ensures a low impedance connection to the end of each strip (Fig. 2.14e). The silver line and the first centimeter of the resistive strips connected to it are covered by a pyralux rim. The resistive strip linear electrical resistance is about 1 MΩ/mm. Since the length of the single strip from half PCB to the silver line varies from 15 cm for SX1 PCB to about 40 cm for SX5 PCB, interconnections have been inserted between the individual strips trying to uniform the resistance of the entire resistive layer therefore allowing for a more homogeneous impedance between the high voltage silver line and the resistive strips, trying to keep the resistance values in the range 5-20 MΩ. Thanks to these interconnections the charge is evacuated through a network of strips and not to a single strip. Another advantage of the interconnections is that defects in the resistive pattern like for e.g. broken strips, become uncritical unless they are too massive. These interconnections, called ladders, are made with the same resistive paste as the strips and are placed every 10 mm in an alternate configuration as Fig. 2.15 shows.

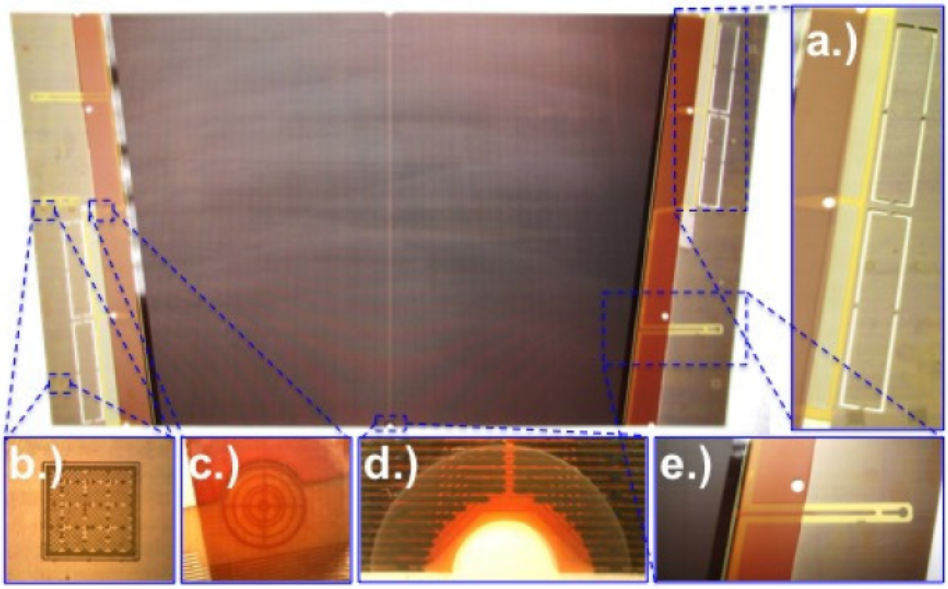

Figure 2.14: A NSW MM anode-PCB with magnification of: a) the connector pad region including holes and the cut-out for electronic cooling; b) Rasnik Masks; c) the precision target; d) the routing of strips around a hole and resistive layer interruption in the board center; e) HV supply point on the copper pattern and part of the silver line. In this image the pyralux rim.

The resistive layer provides protection for the read-out electronics and spark reduction, improving the high rate capability of the detector. The resistive strips are interrupted in the PCB middle (Fig. 2.14d) to achieve a finer granularity in the high voltage distribution. Pyralux pillars (rectangular parallelepiped shape with rounded edges 1000 μm lenght, 200 μm wide and 128 μm height) are arranged in a triangular array 7 mm aside all over

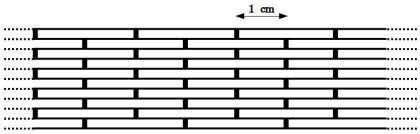

Figure 2.15

the detector area. Its height define, once the mesh is applied on top, the amplification gap. The pillars are created by photoimageable coverlay. Their resistivity is about 10^{16} Ω/cm, producing a small dead area and so a perturbation of the electric field in the region nearby. The boards are left-right symmetric to allow for installation of the same board types in a back-to-back doublet configuration (on the same ROP). While on the ETA-ROP (or ETA doublet) the strips run perpendicular to the precision coordinate (and parallel to each other), the strips are inclined by $\pm 1.5°$ (see [16] for more details) on the STEREO-ROP (second doublet). This allows for the reconstruction of the precision coordinate with a spatial resolution O(100 μm) in both configurations and of the second coordinate with a reduced resolution O(2-3 mm) on a stereo doublet. [32].

For the SM1 chambers have been designed ten kinds of anode-PCBs: 5 ETA PCBs (from SE1 to SE5, with increasing dimensions, corresponding to the 5 sections of any ETA-ROP) and 5 stereo PCBs (from SS1 to SS5, with the same dimensions of the ETA PCBs, corresponding to the 5 sections of any STEREO-ROP. Fig. 2.16 show a drawing of an SM1 anode plane where the identifiers of the different PCBs are represented according to the nomenclature adopted during the NSW MM construction phase. The letter X stands for E or S.

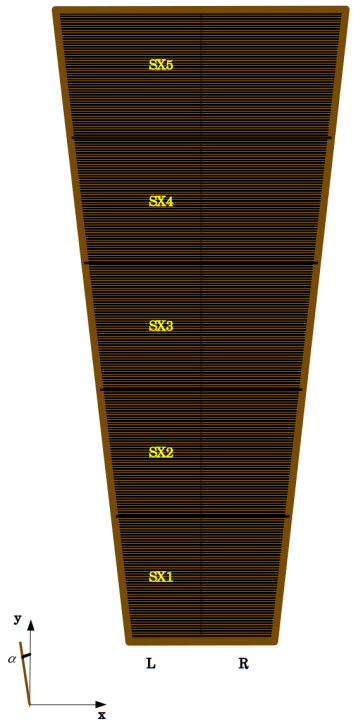

Figure 2.16

Chapter 3

SM1 MicroMegas 4-plet Construction and Tests

It is the first time that MM technology has been used to build such a large detector. Recall that a MM 4-plet has a surface not less than 2 m^2. At the same time, this must guarantee a resolution for perpendicular traces not less than 100 μm. Consequently the 4-plet construction specifications are very stringent.
In order to meet these specifications and verify that they have been respected, construction techniques and quality tests with the related stand have been developed.
In this chapter we will see how the mass production of the SM1 MM 4-plet has been divided into the various INFN sites involved, we will describe the construction techniques and quality tests adopted, without neglecting the operation problems of the detector that accompanied the whole process of production and the solutions adopted. [12] [35] [22]

3.1 SM1 MicroMegas 4-plets workflow

The SM1 MM 4-plet mass production started in 2016 and it is finalized in the end of 2020. The mass production involves both industries and INFN consortia: Cosenza, Laboratori Nazionali di Frascati (LNF), Lecce, Napoli, Roma 1, Roma 3, Pavia. The basic elements (PCBs, micro-mesh, honeycomb, internal frame bars, read-out electronics, ...) that make up the detector are produced by specialized companies after an appropriate knowledge transfer by the NSW collaboration.
Fig. 3.1 shows a diagram that summurize the main detector production phases.
After several quality control tests performed at CERN, the Read-Out PCBs reach the INFN Pavia laboratory which is responsible for the ROPs construction.
The construction and completion of the DPs involve 4 different laboratories (Roma 1, Cosenza, Roma 3, LNF) and can be divided into four steps: DP assembly, Micro-Mesh stretching, DP preparation and DP finalization.
Once the ROPs and DPs are completed and validated they are subjected to a washing and then drying processes. The panels are then assembled to form the MM 4-plet at LNF and the cosmic ray test is performed on it.
Then the latter reaches the CERN where, after further tests, it is integrated into the Double Wedge (DB) and then into the NSW.

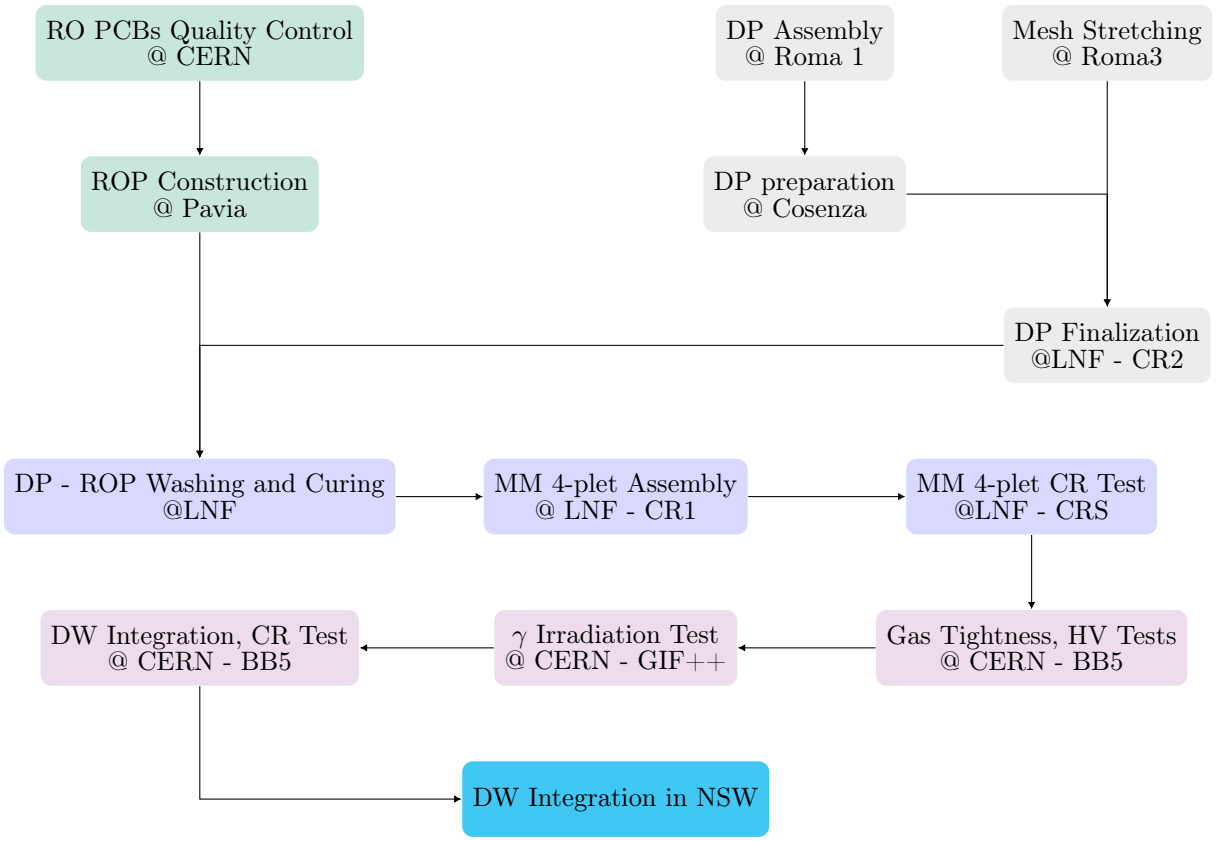

Figure 3.1: SM1 MM 4-plet construction workflow.

3.2 Read Out Panel Construction

3.2.1 Read Out Panel Assembly

The ROP houses the MM read-out strips. It is clear that the single strip global position of a single PCB, as well as the relative position of a strip wrt the strips of the other PCBs, must be known with a certain degree of accuracy. Assuming that the XY plane corresponds to the plane of the PCB and that X is perpendicular to the strip while Y parallel to the latter the panel construction specifications require a maximum tolerance of 40 μm in X and 150 μm in Y for the alignment of the single strip and 60 μm in X and 300 μm in Y for the alignment between different PCBs. Since the detector amplification gap is equal to 128 μm nominal, it is essential that the panel planarity has a tolerance equal to 110 μm which translates into an RMS of 37 μm. The procedure described below satisfies these requirements.
The ROPs assembly is done in a single step procedure. It was performed in a class 10000 clean room, using a (350 $\times$ 200 $\times$ 35) cm^3 granite table (with a certified maximum deviation from planarity of 8 μm), on which a Coordinate Measuring Machine (CMM) and the construction tools are placed. The construction of the panel is based on reference plates located on the granite table and a stiff-back (Fig. 3.2), both equipped with a vacuum system, precision pins inserted in precise holes and 10 cCCDs for the Rasnik masks reading to check the correct PCBs positioning and strips alignement. The reference plates are rectified aluminum plates, 20 mm thick and with planarity within 20 μm. It is anchored on the granite table. The stiff-back is composed of similar reference plates, mounted on a support made of 2 aluminum skins spaced by 10 cm aluminum honeycomb.

The stiff-back is attached to a crane and can be moved horizontally, vertically, and rotate to allow for an upward or downward facing of the RO plane, depending of the assembly phase.
The first RO plane is sucked on the reference plates on the table; the second on the stiffback. A dry-run is performed to check the coupling of the stiff-back with the reference plate and to get a reference measurement before gluing. At this point, the gluing of the two RO planes, aluminium skeleton and cooling bars is performed. The glue is automatically disposed by a remote controlled machine both on the PCBs on the table and those on the stiff-back. The panel is closed and the glue left to dry for 18 hours. Before switching off the vacuum table, alignment inserts (for eta panels) or pins (for stereo panels) are glued to the panel.

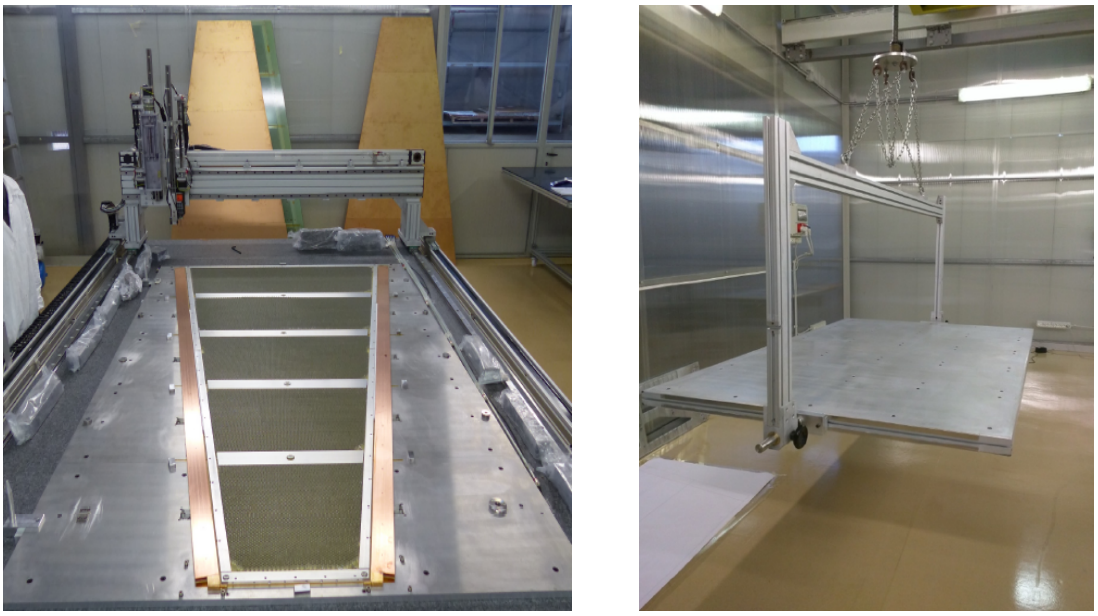

(a) (b)

Figure 3.2: (a): the first RO plane, aluminium skeleton and cooling bars on the reference plate. (b): the stiff-back tool.

Read Out Panel Quality Tests

Before proceeding with the panel assembly, several quality control tests are performed on their components. The skeleton Al bars are checked both for their dimensions, width and thickness, and for possible deviation from straightness (bending and torsion). The thickness bars is checked with a pass/no pass "limbo tool". The honeycomb sheets is only checked for thickness with a micrometer. Due to the panel construction method, a very precise height measurement of the components is not needed, since the discrepancies are compensated by layers of glue. The PCB thickness is measured by mean of the digital gauge.
After the ROP completion a panel planarity mapping is performed using a digital gauge connected to the CMM vertical arm. The planarity of the panel is measured with vacuum on and vacuum off so to verify possible distortions due to internal tension of the panel. Only for the stereo ROP a planarity measurement on both panel sides is performed, while for the ETA ROP the measurement of the planarity is performed only on the alignement

pin side. Figg. 3.3a and 3.3b shows the mean value of the panel thickness and the RMS of the planarity distribution as function of the panel number for all assemled 70 ROPs, respectivley.

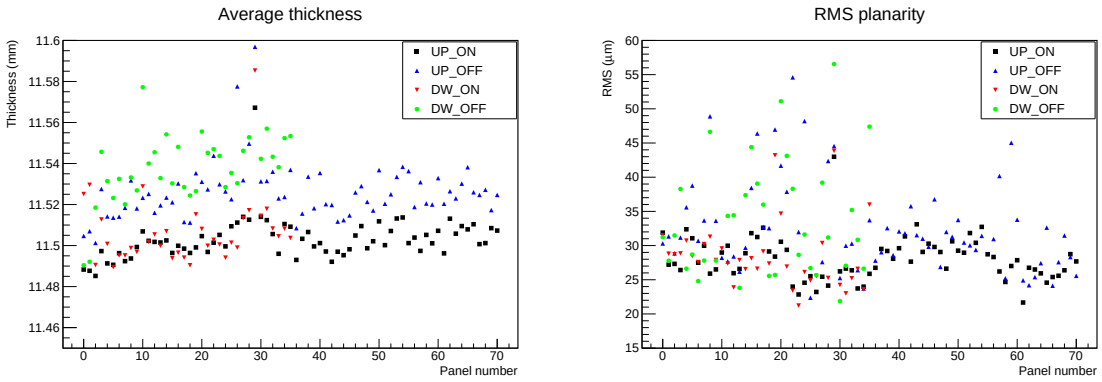

(a) (b)

Figure 3.3: (a): mean value of the panel thickness as function of the panel number for all assembled ROPs. The nominal average thickness is 11.50 (11.515) mm for vacuum on (off). (b): RMS of the planarity distribution as function of the panel number for all assembled ROPs. The maximum RMS planarity should be 37 *mum*.

Both the single PCB and the glued panels, are tested for their electrical properties. All the measurements are performed by means of a tool which has been designed and built in Pavia, which allows to have contact to the various part of the PCB by selecting dedicated connections (Fig. 3.4). This tool allows to measure the silverline electrical insulation, copper - resistive strips electrical insulation and the resistive strips electrical resistance. The probes used to carry out the resistive strips electrical resistance mapping on the single PCB have a surface of about 1 cm^2 (in Fig. 3.4 the probes are numerated from 1 to 5). Therefore the measurement is not related to the single strip, but to the set of strips and ladders that come into contact with the probe.

In particular, the insulation of the silverline is checked with respect to the HV connection. The measurement is taken with an automated insulation tester, Megger BM25®, which is able to measure resistances up to 1 TΩ. A distribution of the measured silverline insulation is shown in Fig. 3.5a. Most of the tested silverlines are very well insulated (about 1 TΩ).

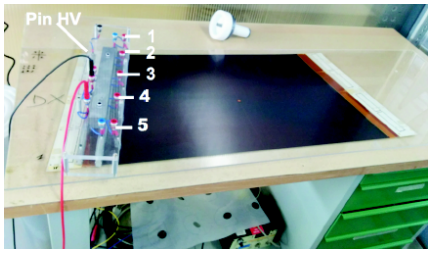

Figure 3.4: Electrical insulation measurement tool.

Insulation of copper versus resistive strips is also checked with the same system. Expected values, above a threshold of 13 GΩ, is always reached, with an average of 30 GΩ, as shown in Fig. 3.5b.

The resistive strips resistance is measured both close to the border with the kapton on the silverline, and in the whole surface of the PCB. Results are shown in Fig. 3.6, where the yellow and the red distributions are the measurements taken close to the silverline and in the main area of the PCBs, respectively. Since a very low resistivity has been observed in the border area, an additional local passivation has been added to prevent the possibility of dangerous discharges.

The last two tests that are carried out on the panel before its validation are the gas

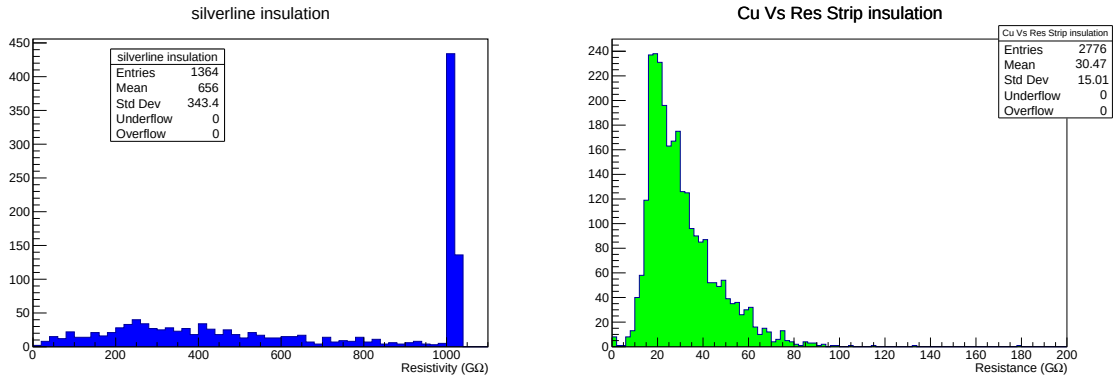

(a) (b)

Figure 3.5: (a): distribution of the silverline insulation obtained on the PCBs glued on panels. (b): distribution of the insulation of copper versus resistive strips.

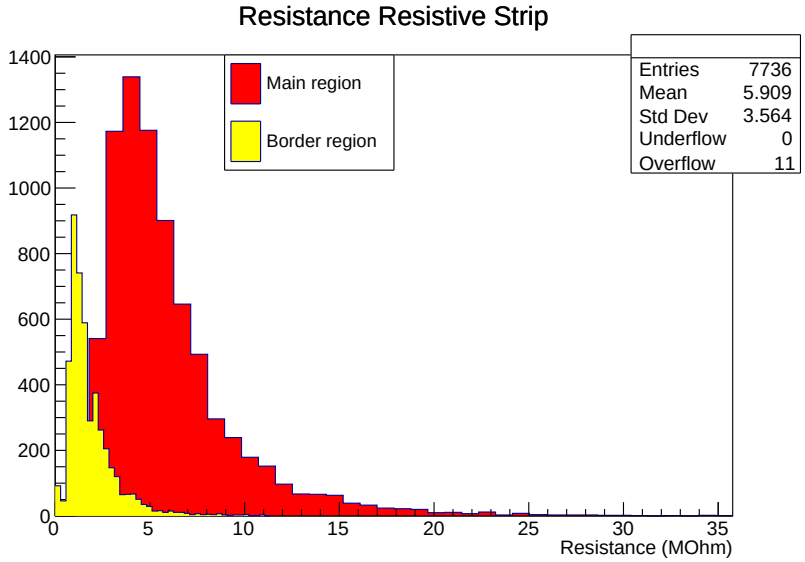

Figure 3.6: Distribution of resistance of the resistive strips.

tightness tests, one local and one global. The first is performed in corrispondence of the PCB - PCB grouting using the drop pressure method. For the second test the panel is coupled with two dummy panels so as to create two gas gaps. To measure the leak rate of the panel is used the Flow Rate Method (FRM).

3.3 Drift Panel Assembly

3.3.1 Assembly Procedure

The DPs hause the MM cathode plane. The drift electric field depend by the panel planarity. Also in this case a tolerance on the planarity of 110 μm is required. DPs were assembly in a class 10,000 clean room of the INFN - Roma 1 laboratory equipped with a granite table with a certified deviation from planarity of 8 μm using the so called vacuum bag technique. When using the vacuum bag technique the height and the planarity of the panel depend by the pile-up of the glued components and by the table planarity. It is therefore mandatory to check the thickness of all the components before assembly. The measurements were performed using the "limbo tool", which will be described later. The distributions of the measurements, regularly spaced over their full length and surface, are given in Fig. 3.7. From top to bottom we see the distribution for lateral frame bars, honeycomb and PCB. Two variants of this method were used: the single-step procedure for the ODP and the two-steps for the CDP.

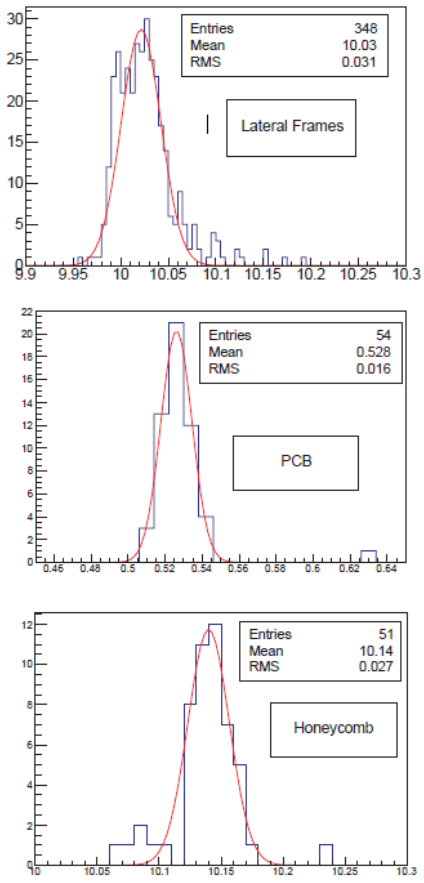

Figure 3.7

The glue was distributed on the PCBs by a programmable glue dispenser hosted in the clean room. About 100 ml of glue are deposited on the PCBs of each side of the panel, resulting in two layers of about 70 μm thickness. The assembly of the panel was driven by an alignment bar mounted on the granite table. First the glue was distributed on the PCB faces not covered by copper. These PCBs were then positioned on the granite table with the glue on the upper face and one of their lateral edges along the alignment bar. The PCBs were fixed to the bar using 5 mm dowel pins. At this point the Al skeleton, the 4 reinforcement interconnection inserts and the 4 gas inserts are positioned on the PCBs. All the skeleton bars are electrically connected with the honeycomb sheets except the minor base bar.

The following operations are different in the single and two step methods. In the single step procedure, used for the ODP, the glue was distributed on the second set of five PCBs without copper, which were then positioned on the components already assembled on the granite table with the glue on the lower face. Then an Al mask was superimposed on the assembled panel. Teflon dowel pins inserted in the holes in the mask determined the position of this second set of PCBs with respect to the other parts of the panel. Then a cover was fixed by a special double face tape to the granite table, in order to form a bag with the table, as shown in Fig. 3.8.

An under pressure of 100-150 mbar was produced and maintained constant for 20 hours in the bag by means of a pump system, while the glue was being cured.

A more accurate procedure was followed to prepare the CDP, where a good planarity is demanded on both sides. In this two step procedure the second set of five PCBs was positioned without glue and the vacuum bag procedure was started. When the curing

Figure 3.8: A drift panel during glue curing (vacuum bag technique) on the granite table.

of the glue on the bottom side was completed, the second set of PCBs was removed and the partially assembled panel was rotated and deposited on a second table. The glue was dispensed on five PCBs, which were positioned on the granite table using the reference bar. Afterwards the already semi-assembled panel was rotated and superimposed. Finally, the vacuum bag was applied again for about 20 hours to complete the assembly of the CDP.

Planarity Test

To measure the DPs thickness and check their planarity a dedicated limbo tool was developed at Laboratorio Alte Energie - Unical (Fig. 3.9). It consists of a reinforced Al profile, instrumented with 10 height digital gauges, read out serially by a PC.

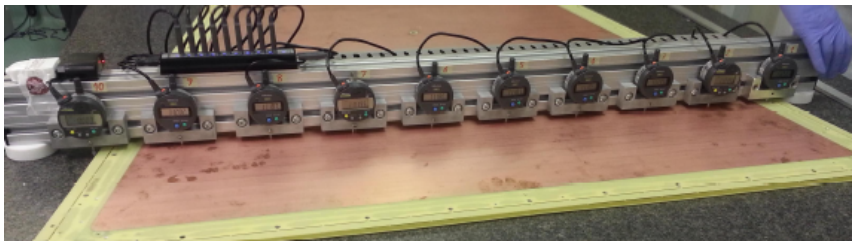

Figure 3.9: Limbo tool while used to measure the planarity of a DP.

The panel is positioned on the granite table. The gauges are zeroed on the granite table at the beginning of the measurement and then moved parallel to the bases at step of about 13 cm in pre-defined positions (Fig. 3.10).
The gauge values are recorded automatically and analyzed both during the measurement and at the end. To verify the quality of the recorded data, the limbo tool is brought back to the initial position where the indicators have been zeroed and the value of their reading has been recorded. Typically, the difference between the two values was found less than 10 μm for each indicator. If at least one of the indicators showed a difference greater than 10 μm the measurement was repeated.
As an example Fig. 3.11 shows the thickness map of the ODP 71. The average and the standard deviation of the measurements are used as estimators of the fluctuation in panel thickness. The planarity is determined by the difference between the maximum and the minimum deviation from the thickness average measurement.

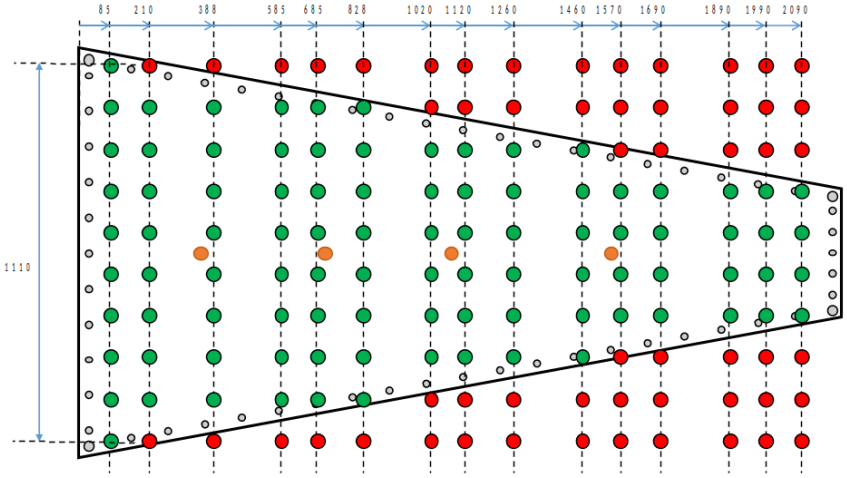

Figure 3.10: The limbo tool position along the panel. The digital gauge that touch the DP surface are drawed in green, the others in red.

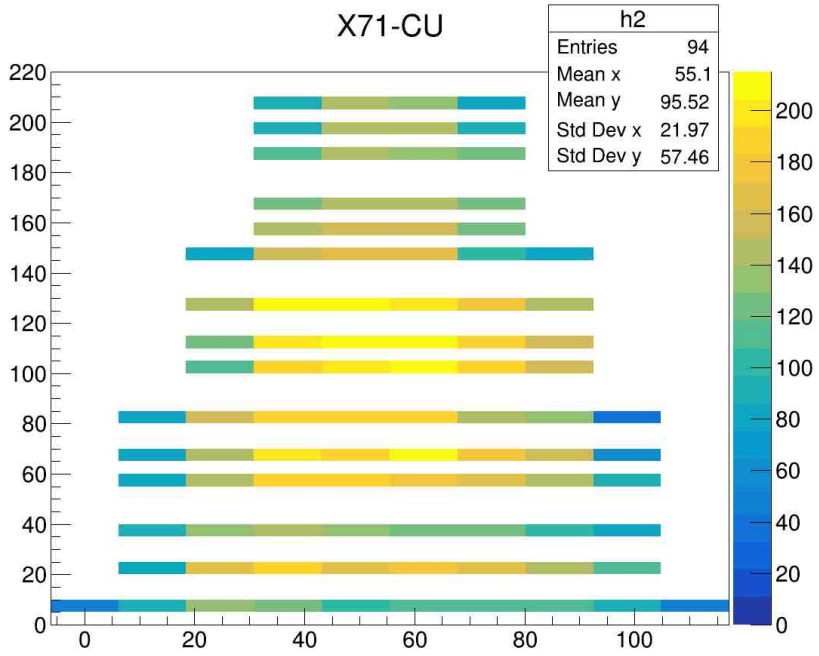

Figure 3.11: Thickness map of the ODP 71.

3.4 Drift Panel Preparation

DP preparation is the intermediate phase between DP assembly and finalization. This phase includes the gluing of some DP components and several quality tests, as well as some operations aimed at improving the efficiency of the panel assembly operations in the 4-plet and the detector efficiency itself.
The preparation of 105 DPs and the respect of the timing dictated by the MM 4-plet integration required a meticulous organization in terms of logistics, work flow, spaces in which to carry out the various operations.
The plot below shows the entire DP preparation procedure adopted during mass production at Laboratorio Alte Energie (LAE) - UNICAL, Cosenza. The blue bars refer to the

time required to perform a specific operation on a single MM 4-plet DPs set (2 ODP and 1 CDP), while the gray bars indicate the required glue curing time for the specific operation. In this subsection all the operations concerning the DP preparation will be described, except for the Global Gas Tightness test (GTT) to which the next chapter will be dedicated.

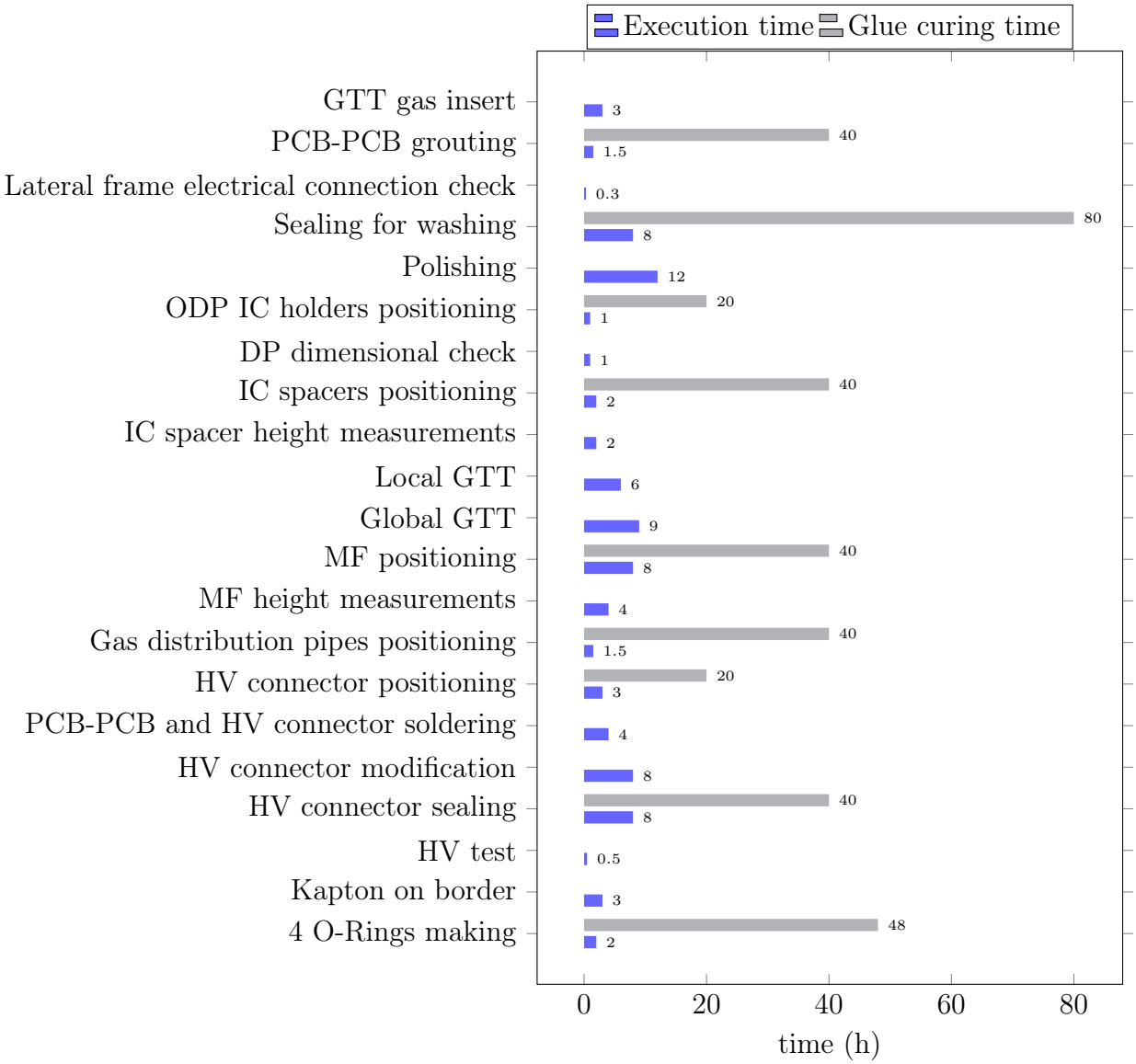

Fig. 3.12 shows how the three Ground Floor (GF) rooms and one First Floor (FF) room of the LAE were organized to deal the DPs preparation.

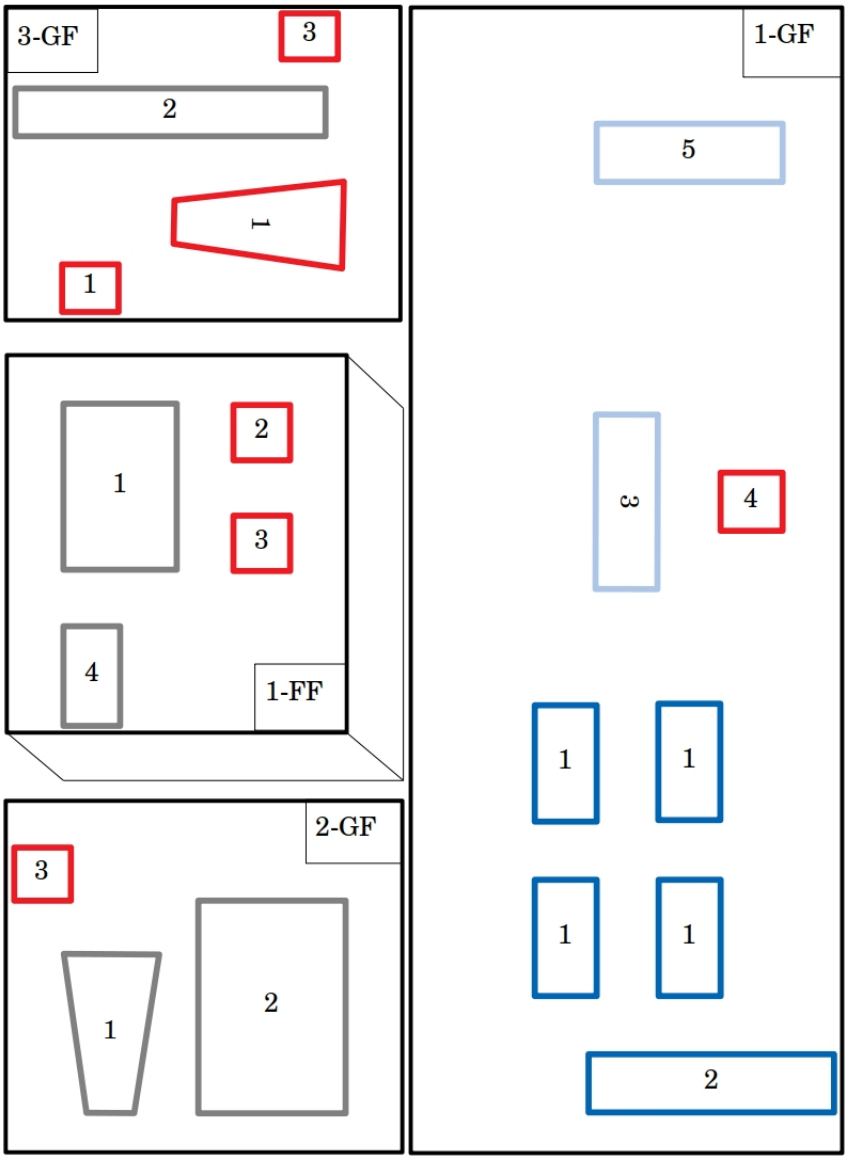

Figure 3.12: **1-GF**: **1 - Horizontal work tables** for PCB-PCB grouting and DPs polishing; **2 - Vertical work support** for DPs polishing; **3 - Vertical support station** for sealing for washing, HV connector gluing, kapton on border; **4 - Power supply** for HV test; **5 - Vertical storage station** for prepared DPs storage. **2 - GF**: **1 - Trapezoidal work table** for IC holders gluing, IC spacers gluing, MF gluing, IC spacer height measurements and local GTT; **2 - Granite table** for IC holders curing, MF curing and MF heigt measurements; **3 - Local GTT stand**. **3 - GF**: **1 - Global GTT stand**; **2 - SM1 and SM2 ORs cutting stand**; **3 - MF thickness measurements test stand**. **1 - FF**: **1 - Horizontal work table** for ORs gluing and curing; **2 - SM1 ORs GTT stand**; **3 - SM2 ORs GTT stand**; **4 - ORs horizontal storage table**.

3.4.1 Gas Inserts GTT

This operation must necessarily be performed first. The reason will become clear in the "Sealing for Washing" subsection.
Fig. 3.13 shows a gas insert drawing. It is made up of two components: a hollow cylinder and a pipe which allows the connection of the MM singlet to the gas distribution system. The local GTT, in this case, allows us to verify that, during the panel assembly phase, the cylinder - PCB joint (point 1) and the cylinder - pipe joint (point 2) were suitably sealed so to avoid gas leak. The test execution method will be described in the dedicated subsection. Point 1 and point 2 are the only possible gas leak sources for the gas distribution insert.
In the event that one or both of these operations have been poorly performed, we proceed in the first case with the addition of a drop of glue at the contact surface between the cylinder and the PCB (point 1) or, in the second case, with the replacement and joint sealing of the pipe.

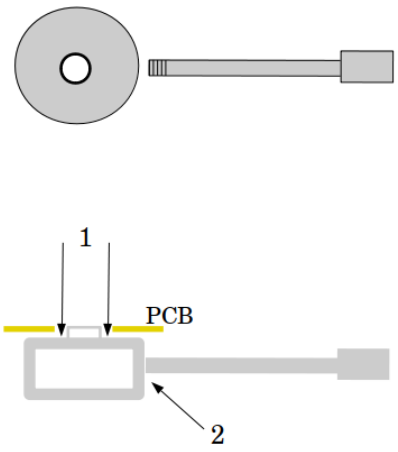

Figure 3.13

3.4.2 PCB - PCB grouting

This operation allows to seal the separating groove between two adjacent PCBs to limit gas leakage from MM module. It is obviously performed on all four grooves present on each DP cathode side. The groove width mainly depends on the PCBs alignement accuracy during DP assembly phase, but it is tipically around 1 mm. The groove depth is equal to the thickness of the PCBs, approximately 0.05 mm.
After the PCBs masking, performed to limit the cathode surface passivation, a curb of glue is distributed along the entire length of the groove. After 30 minutes the curb of glue is split by means of a spatula in order to eliminate part of the air bubbles trapped inside it. After another 10 minutes the glue is well distributed along the PCB-PCB groove and therefore the excess is eliminated. The masking tape is removed immediatly after this last operation.
Fig. 3.14a show a 60x magnification of the separating groove between two PCBs before the grouting in the cathode surface region. We note that the masking tape completely covers the cathode region. As can be seen in Fig. 3.14b, the separating groove is completely sealed. It is also possible to note small areas of the cathode surface near the grouting which are passivated: this is due to capillarity effects between the glue and the masking tape.

3.4.3 Lateral Frame Bars Electrical Connection Check

The aluminum skeleton is connected to ground during the operation of the detector. Fig. 3.15a shows the electrical connection scheme between honeycomb and skeleton bars adopted for all DPs. During the assembly phase it is possible that the glue dirty the electrical contact between the spider connectors and the skeleton components. This results in an increasing insulation between the skeleton components.

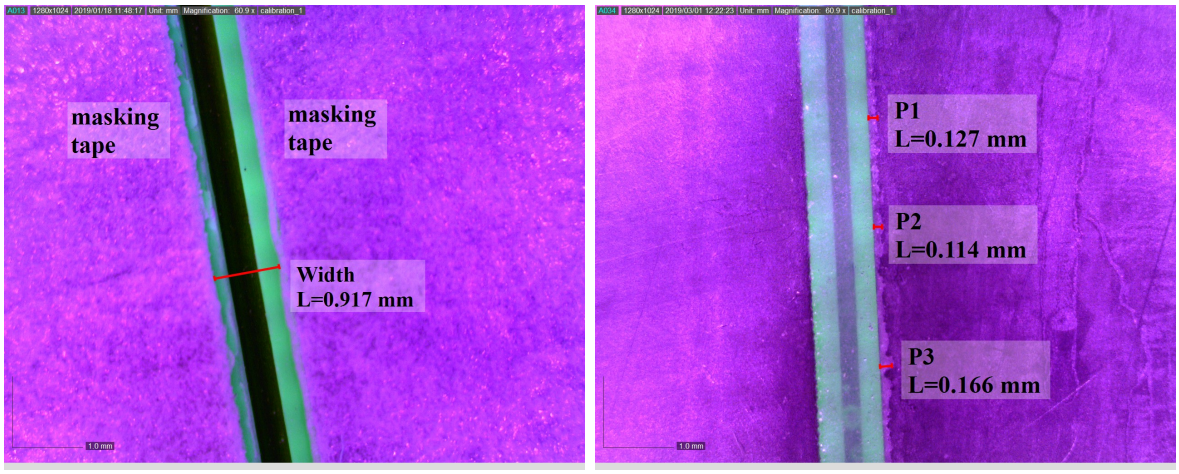

(a) (b)

Figure 3.14: (a): PCB-PCB separating groove in corrispondence of the cathode surface before the grouting. The masking tape completely cover the cathode surface. (b): PCB-PCB separating groove in corrispondence of the cathode surface after the grouting. Passivated zones of the order of 1/10 of mm in width are noted.

The third step is therefore the electrical connection check between adjiacent lateral frame bars, which is performed by means of a Fluke 116 Multimeter®.

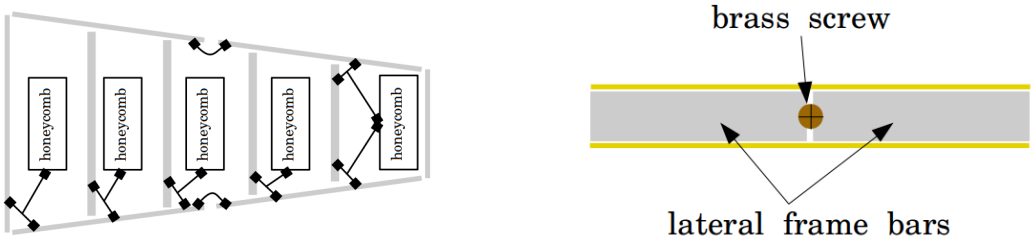

(a) (b)

Figure 3.15: (a): aluminium skeleton electrical connection scheme. (b): a brass screw to fix electrical connection problems.

If a resistance greater than 0.2 Ω is measured between two contiguous lateral frame bars, a brass screw is inserted as shown in Fig. 3.15b so to ensures the correct lateral frame electrical connection. To note that the DP minor base lateral frame bar is voluntarily left disconnected from the rest of the internal frame in order to avoid the formation of eddy currents.

3.4.4 Sealing For Washing

The first MM modules produced showed great instability during the HV tests. These instabilities were related mainly to the presence of dirty on the detector amplification volume surfaces (mesh and ROP). It was therefore necessary to introduce a careful washing procedure for the ROPs and for the DPs into the detector production chain. The washing procedure will be described later. As a result we were forced to make the DPs "water proof". The DP sealing for washing operation is aimed at sealing all the gaps present in the DP structure that can generate water infiltrations inside the volume of the panel between the two external sides. In particular we have: 6 gaps between two adjiacent lateral frame bars (Fig. 3.16), 4 gaps between PCB and gas insert (Fig. 3.17), small lesions on the assembly hole walls (Fig. 3.18) generated during the lateral frame bars milling to create the MM assembly holes (the bars are hallow) and the FR4-FR4 separating grooves present only on the outer skin of the ODPs (Fig. 3.19). In the first two cases, injections of glue are used. In the third case a piece of Kapton® is glued onto the assembly hole wall. In the latter case, grouting is carried out like those described for the PCB-PCB separating groove.
Another operation necessary to make the panel water proof is the sealing of the compression bars fixing holes present present on the lateral frame by means of Kapton tape. This operation is performed after the HV test, before the panels are transported to Frascati. Once the panel has been washed, the tape is removed.

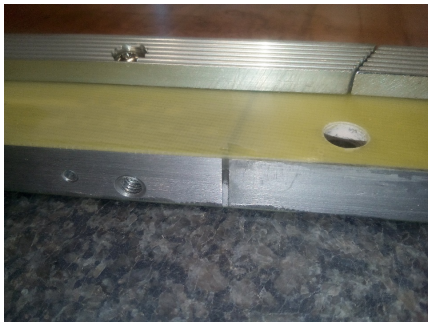

Figure 3.16

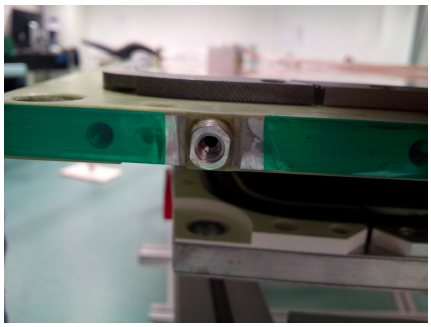

Figure 3.17

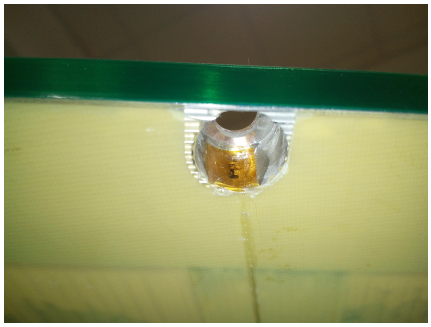

Figure 3.18

3.4.5 Polishing

This operation is foundamental to: flatten the DP passive surface on which will be fixed the mesh-frame, facilitate the 4-plet MM assembly procedure, garantee a correct compression bars positioning and 4-plet gas tightness. The operation begins with the reopening of the mesh frame fixing, gas gap fixing, assembly holes obstructed by glue during the DP assembly (per panel there are 51 holes 2.2 mm diameter, 4 holes 3 mm diameter, 54 holes 6 mm diameter and 4 holes 15 mm diameter). Then the removal of the glue in excess from the external frames and the correction of possible FR4 delamination problems due to lack of glue follow. The glue residues along the edges of the panels, together with the protrusions of the PCBs with respect to the internal frame, are removed with a file and coarse sandpaper and finally

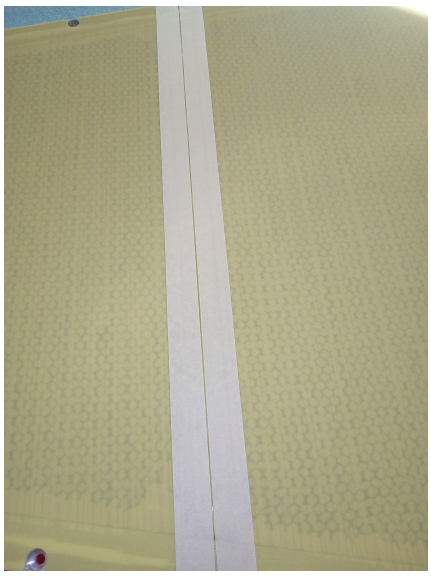

Figure 3.19

polished with fine sandpaper. Morover the DP passive surface is polished and cleaned of glue residues. This polishing is made using fine sandpaper 1000 grade. Fig. 3.20a and Fig. 3.20b show a 60× magnification of the DP passive surface in corrispondence of the PCB-PCB separating groove before and after the grouting and the polishing. The glue curb must be brought by means of the polishing to the same level as the FR4 surface. The grouting must not show imperfections, such as air bubbles, in correspondence with the O-Ring groove.

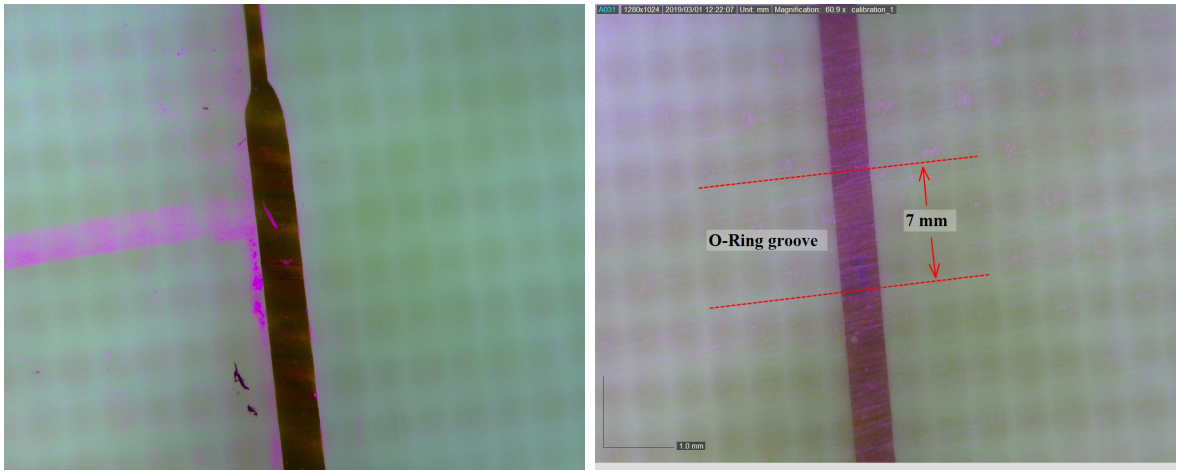

(a) (b)

Figure 3.20: (a): a 60× magnification of the OR groove surface before the grouting and polishing procedure. (b): a 60× magnification of the O-Ring groove surface after the grouting and polishing procedure.

3.4.6 ODP IC Holders Gluing, DP Dimensional Check, IC Spacers Gluing and IC Spacer Height Measurements

In this subsection will be described the following workflow operations: ODP IC holders gluing, IC spacers gluing and IC spacer height measurements.
The IC holders are gluing only on the ODPs. They have a dual function: to receive the nut that allows the tightening of the interconnections during the assembly phase and allows the IC spacer positioning. The holders are glued inside their respective ODP housings. The panel is then placed on the granite table under the weight of 4 lead bricks (11 kg each) positioned near the interconnection holes (Fig. 3.21). Before gluing the IC spacers on ODPs or CDPs, the DP dimensional check is carried out. The ODP or CDP is placed on the granite table and the distance from the center of each interconnection hole to the minor base of the panel is measured and compared with the design values. Subsequently the distance between the two oblique sides is measured in four points and then compared with the design values. The points coincide with the assembly holes at the ends of the inner bar frames. A stainless-steel ruler was then placed parallel to the panel bases and passing through the points mentioned above as shown in Fig. 3.22. All measurements taken are less than 0.5 mm from the design value, which is considered acceptable.
The IC spacers are glued on ODPs and CDPs. The nominal spacer height wrt the cathode plane is fixed at 5 mm (the nominal drift region thickness) with a tolerance of $\pm$ 30 μm. Moreover, the edge surface of the spacer must be as parallel as possible to the DP cathode surface, so to ensure an excellent coupling between DP and ROP during the assembly phase. In order to satisfy this specs., a special tool has been developed from Roma 3 mechanical workshop consisting of a circular stainless steel washer (use to set the spacer height) with a thickness of 5.015 mm and a three-arms brass stretcher (Fig. 3.24). The washer is positioned on the DP surface centered wrt the interconnection hole; the spacer is screwed onto the stretcher; a large string of glue is distributed on the edge of the spacer thread so as to definitively fixing the spacer and to sealing the contact surface between the PCB and IC internal disc; then the spacer is screwed into the IC holder/internal disc by means of a dynamometric screwdriver with a tightening torque set at 1.5 N m. After the glue curing the stretchers are removed, while the washer remain in place, and the height

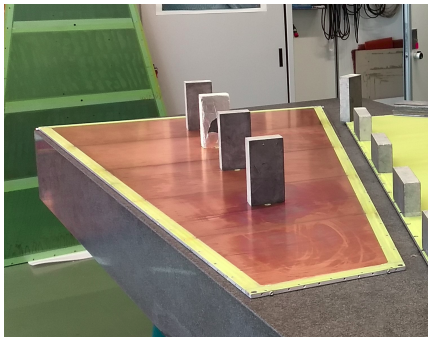

Figure 3.21

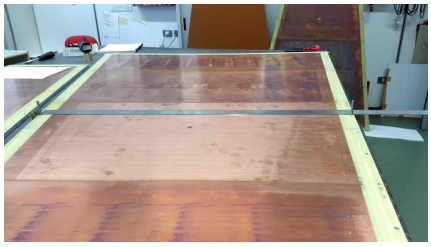

Figure 3.22

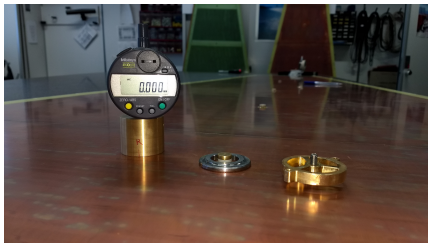

Figure 3.23

Figure 3.24

IC spacer measurements are performed by mean of a dedicated gauge formed by the comparator Mitutoyo 543-253 Digimatic Indicator® with a 0.001 mm resolution and a brass cylinder support (Fig. 3.23). The cylinder has two holes, one to house the spacer and a second one to hold the probe comparator. The center of this second hole falls on the border of the spacer. The comparator is first zeroed on the granite table and then put on the washer. Rotating the cylinder four times with an angular pitch of $\pi/2$, starting from the point closer to the minor base, the height of the spacer is recorded in four points and data analyzed to extract both the average height and the upper surface spacer inclination wrt the panel surface.
Fig. 3.25 shows the distribution of the residuals of the IC spacer height wrt the nominal value for 64 ODPs and 32 CDPs or the DPs used to complete the 32 SM1 4-plets. The data are fitted with a gaussian function whose standard deviation is about 18 μm and mean value is centered around 8 μm. This non-zero value can be explained as follows: to keep the spacer in the correct position it is necessary to fix it firmly in the three-arms brass stretcher and then screw it into the IC holder/disc by applying a torque with the screwdriver. The end result is that the three-arms brass stretcher, resting on the stainless-steel washer, pulls the IC internal disc outwards. After the glue is cured and the stretcher is removed, the internal disc returns to its initial position, taking the spacer with it. This involves a reduction of the height of the spacer Δh with respect to the surface of the panel. The height of the spacer is therefore the thickness of the stainless-steel washer (5.015 mm) reduced by Δh. In the stainless-steel washer design, the Δh value is purely overestimated so that the spacer tend to be a few micrometers higher than the nominal value.
The spacer upper surface inclination wrt the DP cathode surface is defined as the ratio between the difference of the two diametrically opposite height measures and the diameter of the spacer (10 mm)

$$\tan\alpha = \frac{(h_1 - h_2)}{d_{spacer}}$$

We define two inclinations: along and perpindicular to the DP bases, or wrt the x and y axis, $\tan\alpha_x$ and $\tan\alpha_y$. Figg. 3.26, 3.27 show the distribution of the two sapcer upper surface inclinations. In both cases the average value is close to zero, as expected, while the standard deviation tells us that the spacer upper surface is parallel to that of the panel within about 1 mrad. Fig 3.28 shows the scatter plot of these two angular variables. The data is distributed in this plane without showing any relevant correlation.

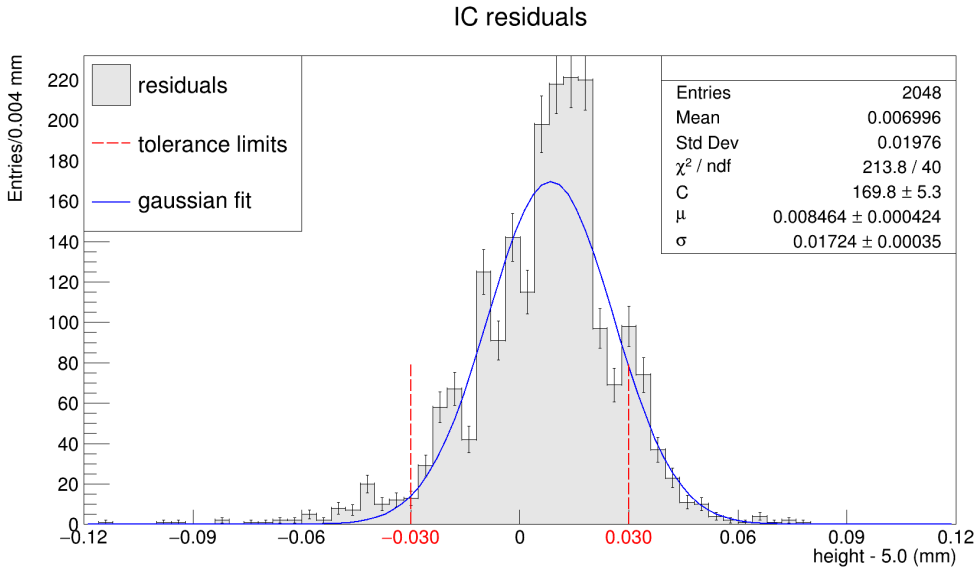

Figure 3.25: Distribution of the IC spacer heights with respect to the nominal value (5.0 mm) for 64 ODPs and 32 CDPs. The distribution is fitted with a gaussian function whose parameters are $\mu \simeq 8\mu m$ and $\sigma \simeq 18\mu m$.

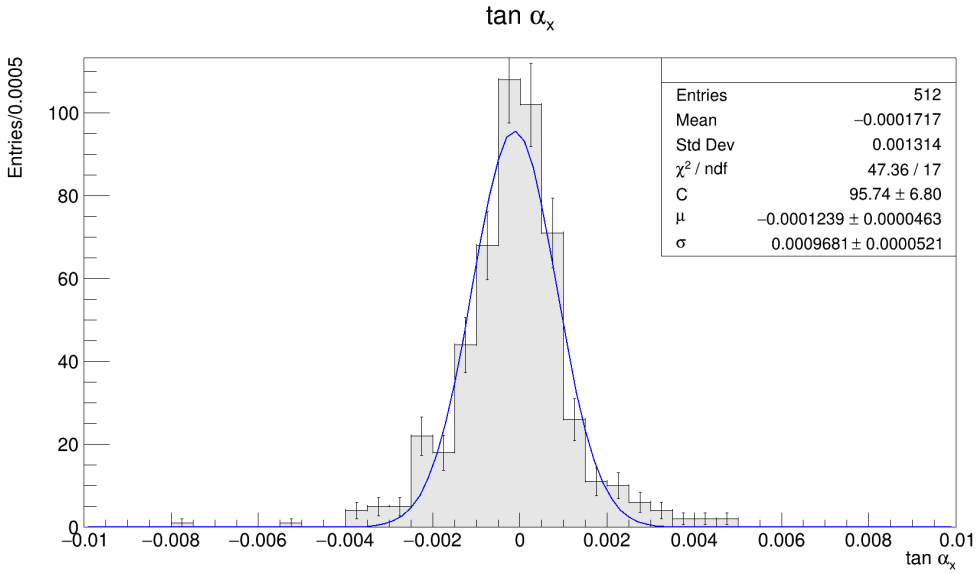

Figure 3.26: The $\tan \alpha_x$ distribution for 96 DPs. The distribution is fitted with a gaussian function. μ is close to zero and σ is close to 1 mrad.

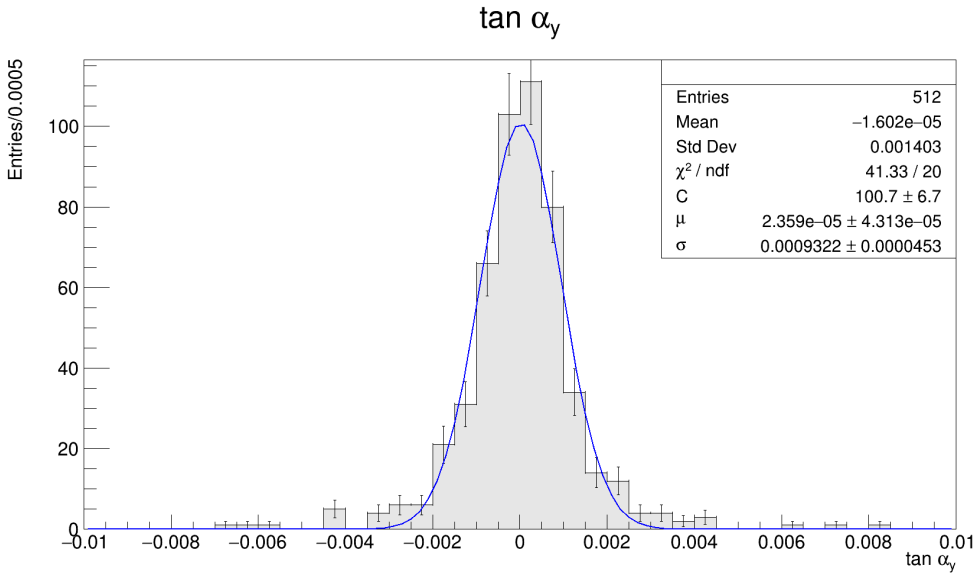

Figure 3.27: The $\tan\alpha_y$ distribution for 96 DPs. The distribution is fitted with a gaussian function. μ is close to zero and σ is close to 1 mrad.

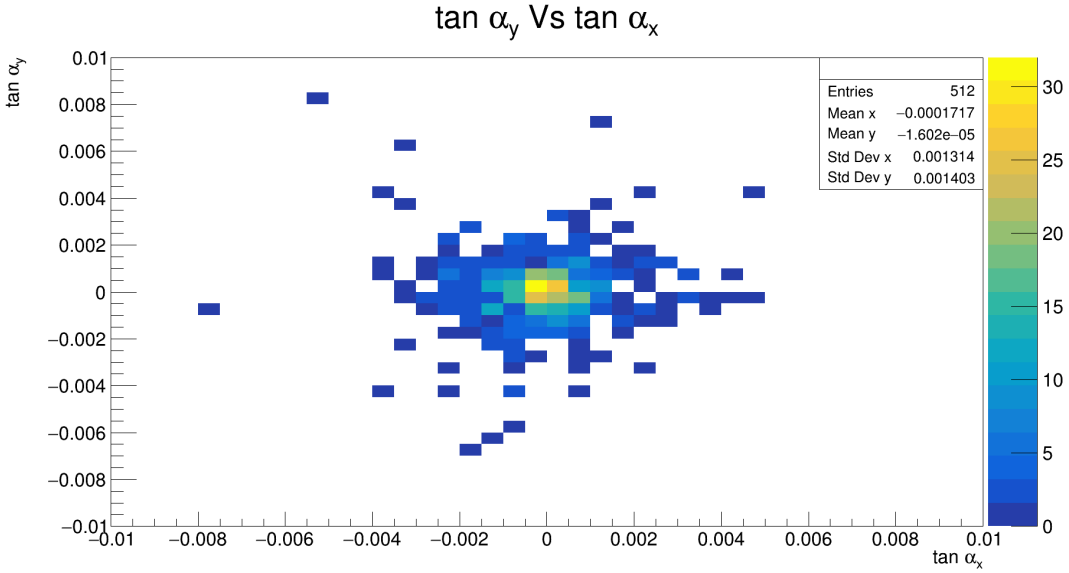

Figure 3.28: Scatter plot of $\tan\alpha_y$ versus $\tan\alpha_x$. No relevant correlation between these variables is evident.

3.4.7 Local Gas Tightness Test

The local Gas Tightness Test (GTT) is a pass/no pass test that allows us to verify that a particular part of the panel susceptible to gas leak is properly sealed or not. In particular the local GTT is used to check, for each DP cathode surface,

- the FR4 passive surface - lateral frame sealing in corrispondence of the 26 mesh-frame fixing holes;
- 4 FR4 - gas inserts sealing and gas insert junction between hallow cylinder and pipe;
- the goodness of the 8 groutings in corrispondence of the OR groove;
- the sealing of the 2 HV electrical connection holes;
- the 4 FR4 - IC insert sealing.

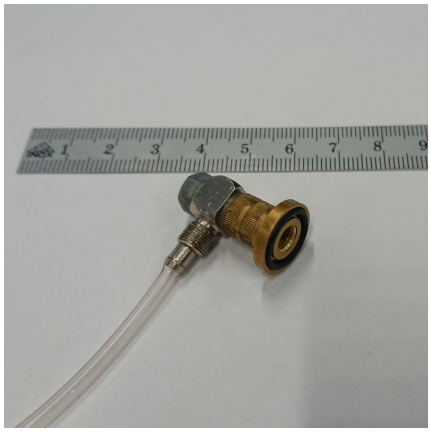

Figure 3.29: The vessel A.

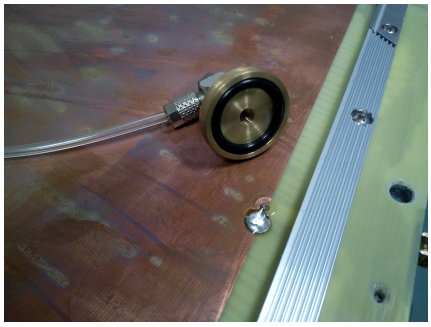

Figure 3.30: The vessel B.

Figure 3.31: The vessel C.

The test is based on the pressure drop method for indeformable volumes and uses three distinct indeformable vessels complete with O-Ring: A, B and C (Figg. 3.29, 3.30, 3.31). These vessels have been developed ad hoc for the different parts of the panel to be tested. A has a volume $V_A \simeq 0.3$ ml and it is used for the 26 mesh frame fixing holes, 4 gas inserts and for the 8 groutings in corrispondence of the OR groove. B has a volume $V_B \simeq 0.7$ ml and it is used for the 2 HV electrical connection holes. C with a volume $V_C \simeq 1.4$ ml is used to check the 4 FR4 - IC insert sealing.
Before starting the test, it is necessary, in some cases, to close one side of the through holes. The fixing holes of the mesh-frame on the CDP are plugged with Kapton tape; the gas distribution inserts are plugged by mean of a M3 brass screw complete with O-Ring. The holes of the interconnections are plugged using the brass end-plug for the ODPs, while Al end-plugs are used for the CDPs. Moreover, the air tightness test of the HV holes is performed only after the installation of the HV connectors which is the last process that is performed on the panel before being shipped to Frascati for mesh gluing and SM1 MM assembling. Then the vessels are positioned on the part to be tested in such a way as to create a closed volume. They must be in good contact with the part to be tested and the O-Ring must be well pressed against the surface in order to seal the internal volume of the vessels. A and B are held in place and pressed by means of a spring clamp (its clamping force is about 100 N), while the aluminum vessel C is screwed onto the IC spacer. The vessels are connected through a 1 mm internal diameter poliethylene tube to the differential pressure sensor HCLA12X5EU® (Figg. 3.32, 3.33, 3.34).

It has a 4 V Full Scale Span (FSS), from 0.25 to 4.25 V that correspond to an operating pressure from 0 to 12.5 mbar. Its analog signal is digital converted from the Successive Approximation Register Analog to Digital Converter (SAR ADC) of the STM32F3Discovery® micro-controller which has 12 bit resolution and a voltage reference of 3.3 V. Consequentley we can appreciate a $3 \cdot 10^{-3}$ mbar pressure variation and read a maximum pressure of 9.5 mbar before reaching ADC saturation. The micro-controller is serially connected to a PC where a Graphical User Interface (GUI) (Fig. 3.35) developed in LabVIEW® is available. It provides the trend of the pressure inside the test volume as a function of time and calculates the air loss of the tested part. To minimize the noise related to the differential pressure sensor analog signal and to the ADC, we perform an average on 50 signal samples for each pressure measurement. This GUI allows us to observe the trend of the pressure drop over time and also automatically provides the test result. Just connect the A or B vessel polyethylene tube to the differential sensor pressure port to obtain an overpressure, due to a volume reduction, of 8 or 6 mbar respectively. The C vessel is screwed into the spacer, so its internal overpressure depends on the torque applied. Generally the initial overpressure varies between 6 and 8 mbar. In both cases we remain below the 9.5 mbar limit imposed by the microcontroller ADC. Ten seconds after inserting the tube into the sensor port, the test begins. Ten overpressure values are recorded at intervals of about 3 seconds from each other. After 30 seconds the GUI calculates the difference between the initial overpressure p_0 ($t = 0$) and that recorded at t = 30 s, p_{30} and relates it to the overpressure of 3 mbar characteristic of the MM modules by multiplying the result by the factor $\frac{(p_0+p_{30})/2}{3}$. If the result is minor than $\frac{1.5}{30}$ $mbar/s$ the closed volume is considered tight, while if the result is greater than $\frac{1.5}{30}$ $mbar/s$ the closed volume is considered leak. The limit of $\frac{1.5}{30}$ $mbar/s$ for each gas leak source is well below the limit imposed by ATLAS. Indeed using the Eq. D.4 and then assuming that during a local GTT all the gas leak sources present the same pressure drop we can write:

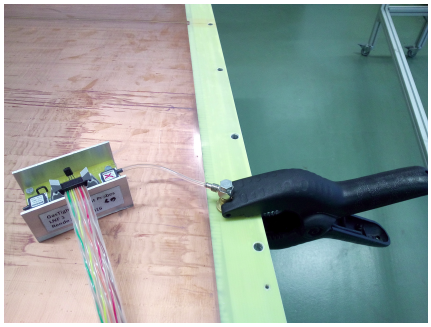

Figure 3.32

Figure 3.33

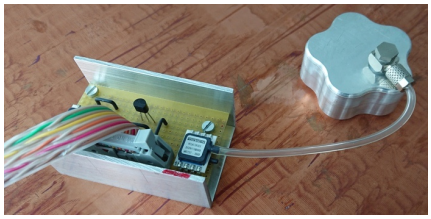

Figure 3.34

$$\frac{0.6}{3600}\ mbar/s \cdot 7.5\ l =$$

$$\frac{dp'}{dt}\ mbar/s\ (38 \cdot 3 + 2 \cdot 7 + 4 \cdot 14) \cdot 10^{-4}\ l \Rightarrow$$

$$\Rightarrow \frac{dp'}{dt} \simeq 0.07\ mbar/s\ or\ 2\ mbar/30\ s$$

that is, at an overpressure of 3 mbar, the pressure drop can reach a maximum of about $\frac{2}{30}$ $mbar/s$ for each gas leak source. It should also be noted that in the above equation the limit is understimated as the overpressure inside the closed volume during the test is always greater than 3 mbar.

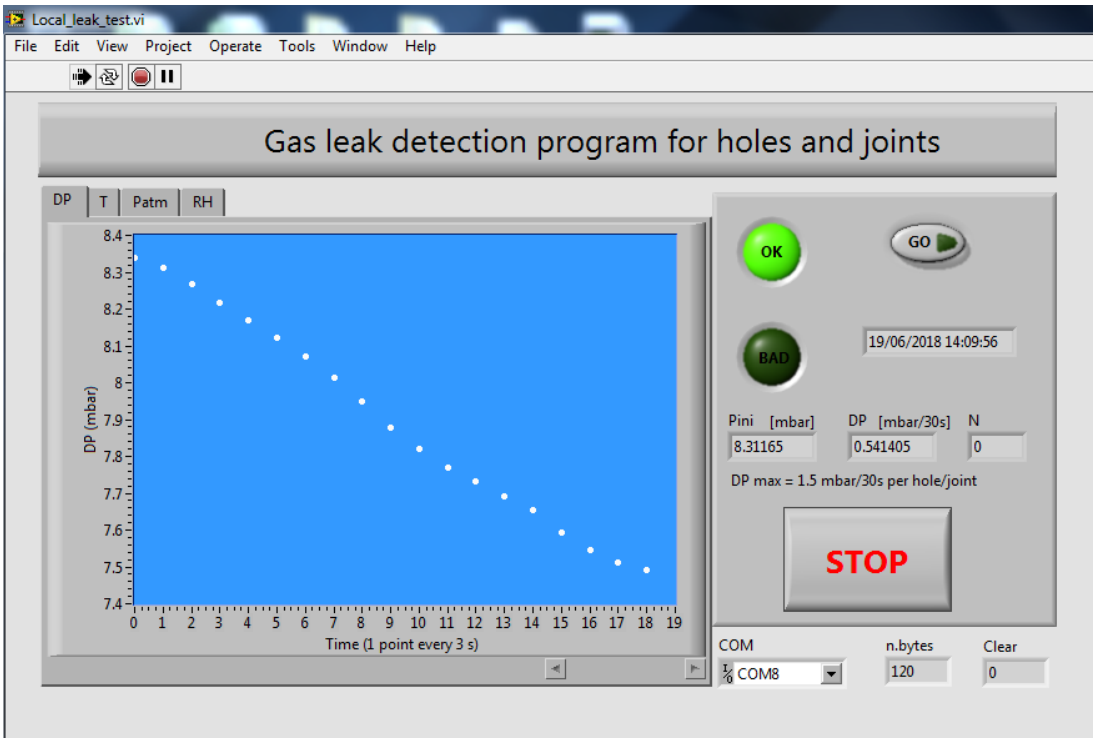

Figure 3.35: Screenshot of the LabVIEW GUI developed for the local GTT. If dp/30 s is smaller than 1.5 mbar/30 s the OK buttun is lightning.

Below we report the average values of several measurement samples with positive results performed on different sources of gas leak using the local GTT:

- 0.3 mbar/30 s for MF fixing hole;
- 0.2 mbar/30 s for grouting;
- 0.05 mbar/30 s for IC;
- 0.3 mbar/30 s for gas insert;
- 0.22 mbar/30 s for HV electrical connection hole;

Experience has taught us that in the case where there is a leak, two cases can occur: the closed volume overpressure goes to zero in a few seconds (3 - 5 s) or the initial overpressure does not reach the expected value.
Fig. 3.36a shows the part close to a mesh-frame fixing hole where poorly FR4 - lateral frame sealing is evident. In this case a gas leakage between the FR4 and the internal frame would be inevitable. The problem is fixed by enlarging the FR4 hole and inserting a drop of glue so as to seal the area. After the glue curing a new polishing is performed (Fig. 3.36b). A new local GTT is performed on the part in order to verify the correct outcome of the new sealing operation.

(a) (b)

Figure 3.36: (a): the mesh-frame fixing hole where poorly FR4 - lateral frame sealing is evident before the new sealing operation. The hole is enlarged so as to favor a better adhesion of the glue between FR4 and lateral frame. (b): the mesh-frame fixing hole after the new sealing operation and polishing.

3.4.8 Mesh-Frame Positioning

After carrying out the global GTT we move on to the mesh-frame positioning.
The profiles and corners used for the mesh-frame positioning on the panel are first of all subjected to a quality control check: their highest side is measured using a Mitutoyo 121-155® Bench Micrometer (Fig. 3.37). The height is measured in 5 points along each profile, in correspondence to the three fixing holes and in between each pair of holes. For the corners the height was checked in correspondence of the fixing holes. Only the components with height within the required limits [5.060 ± 0.030] mm are employed for the mesh-frame positioning. The rejection rate was a few per thousand.

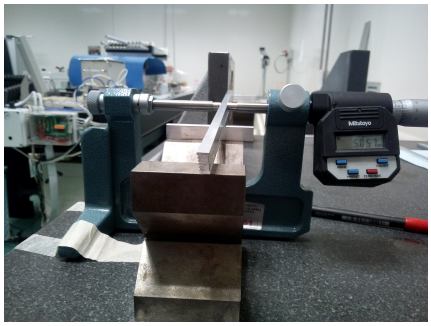

Figure 3.37

Mesh-frame must be positioned accurately on the FR4 passive surface at a distance of 19 mm from the lateral frame edges and at 9 mm to the copper surface. The specs. for the mesh-frame positioning are: ± 200 μm in the plane and ± 30 μm in height. The required accuracy is guaranteed both by the accuracy of precision in the machining of mesh-frame profiles and corners and by two aluminum rulers used to position the profiles at 19 mm from the lateral frame edges. This ensured that the gas gap frame is always flush with the internal frame edge, preventing it from invading the space intended for the electronic boards.

Figure 3.38

The DP is placed on the trapezoidal table and before starting the mesh-frame positioning a dry run (Fig. 3.38) is performed to verify that the fixing holes on the mesh-frame coincide with those on the internal lateral frame. Fig. 3.39 shows two mesh-frame profiles with its bottom side up during glue spreading. The employed plastic dispenser fills the groove with the right amount of glue. After fill the bottom groove with epoxy glue the mesh-frame profile/corner is turned upside down and positioned on the panel by the help of the aluminium rulers (Fig. 3.40). The highest side of the mesh-frame profiles/corners is oriented towards the cathode. The ground/fixing screws are inserted and tightened. The glue curing take place with the panel turned upside down on the granite table in order to put the upper side of the mesh-frame profile in contact with the granite table surface. Lead bricks (11 kg each) are placed on top of the panel near the boundary between each pair of mesh-frame fixing screws and in correspondence of each mesh-frame corner, to improve the contact between the panel and the mesh-frame (Fig. 3.41 shows two CDPs during mesh-frame curing on the granite table. The large surface of the granite table allowed us to glue and cure two mesh-frames a day).

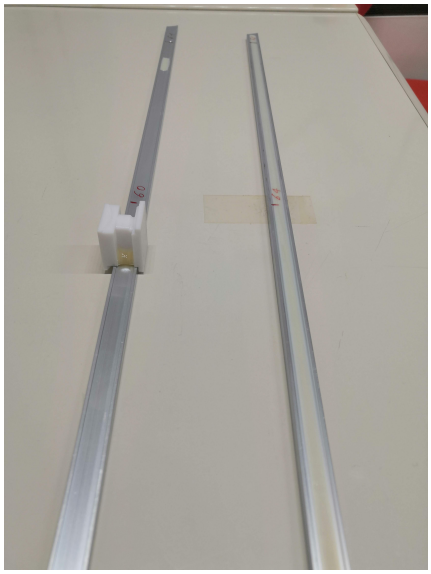

Figure 3.39

When the glue is completely cured the height of the mesh-frame was measured by means of a digital gauge (Borletti® Millesimal Comparator, Mitutoyo® Digital Indicator) mounted on a stainless steel tripod or on an arched holder as shown in Fig. 3.42. The first is used to measure the height of the mesh-frame profiles, while the second the height of the mesh-frame corners. In both cases the comparator is zeroed near the FR4 surface between the mesh-frame and the copper surface. Then it is placed on the highest point of the mesh-frame and data is recorded. This measurement is done close to the grounding/fixing screws (26 points) and, only for the mesh-frame profiles, in between each pair of fixing screws (10 points). Fig. 3.43 shows the distribution of mesh-frame height measurement for 64 ODPs and 32 CDPs. The distribution is centered to the expected value 5.060 mm, with a standard deviation of 10 μm, well below the required tolerance $\pm$ 0.030 mm. The few data outside the tolerance limits refer to measurements performed at the corners. In fact, the panel planarity near the corners was found to be, in some cases, poorer.

Figure 3.40

Figure 3.41

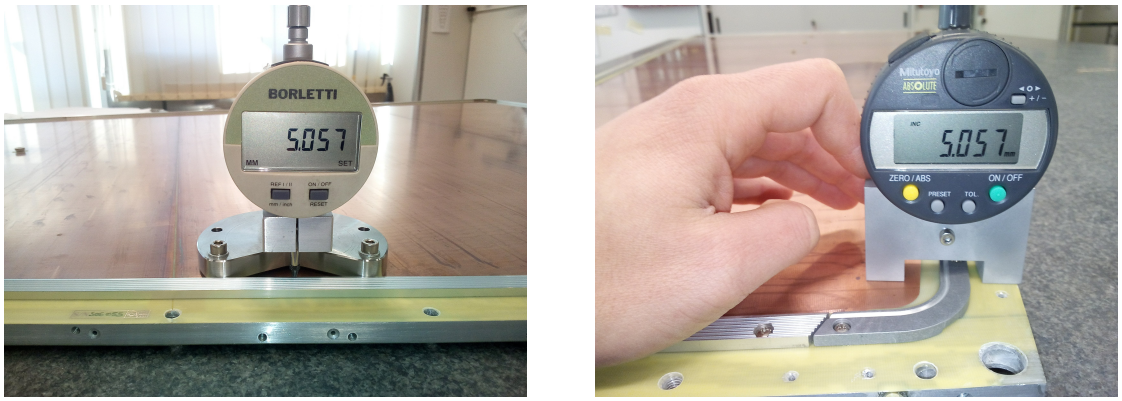

(a) (b)

Figure 3.42: (a): the digital gauge used to measure the mesh-frame profile height. (b): the digital gauge used to measure the mesh-frame corners height.

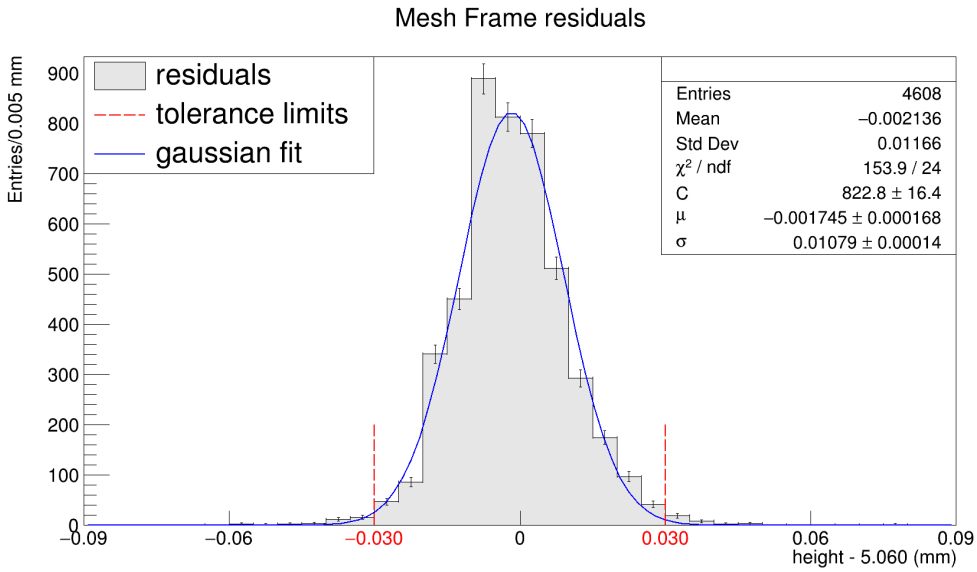

Figure 3.43: Distribution of the mesh-frame height residuals for 64 ODPs and 32 CDPs. The data are fitted with a gaussian function. The expected value and standard deviation are 2 μm and 11 μm, respectively. The red dash lines indicate the tolerance limits on the height of the mesh-frame with respect to the cathode plane.

3.4.9 Gas Distribution Pipes Positioning

Before positioning the gas distribution pipes on the DP, they must be completed with the L-shaped aluminum insert in a dedicated template (Fig. 3.44). It is divided into two sections, one for the tube length of 279 mm (below in the photo) and the other for the length of 1071 mm (above in the photo). An example of a mounted tube is placed on the granite table. To fix the L-shape insert to the tube the epoxy glue is used. After the glue curing, it is checked that the duct is not blocked by the glue trivially going to check that the air introduced by means of a syringe from one end of the pipe comes out smoothly from the other end. For each drift panel gas gap there are two gas distribution pipes: one connected to the gas inlet and the other to the gas outlet. The pipes run parallel to the panel bases. The pipes complete with the L-shaped inserts are glued in their respective seats and kept at a distance of 1 mm from the mesh-frame and 3 mm to the copper surface through the use of stainless steel spacers and Kapton tape with which the pipe is pressed against the spacers. At this time some points of glue are inserted between the pipes and the mesh-frame so to definetly position the pipes. Once the glue curing occurs the washers were removed and "w" shaped stainless-steel strips, 1.1 mm thickness, are inserted between the pipe and the mesh-frame. These "w" strips realize the electrical connection to mesh-frame that in turn is connected to the panel ground. Once inserted they are covered with epoxy glue to secure them in that position (Fig. 3.45).

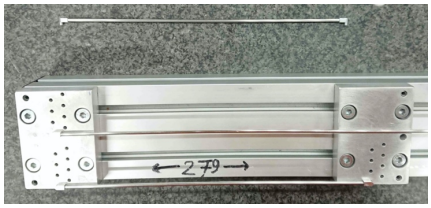

Figure 3.44

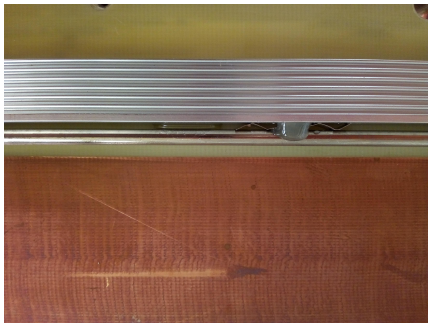

Figure 3.45

3.4.10 HV Connector Positioning and PCB-PCB Electrical Connection

The last step is to mount the High Voltage (HV) connector and make the electrical connections of the 5 cathodes. Two HV connectors per cathode are mounted on each DP in the dedicated lateral frame seats. The HV connectors are soldered on a small PCB which only allows the connection of the central pin (HV+) of the connector to the DP cathode via a HV cable. Ground connection (HV-) is missing. To create this connection, a small brass strip is welded to two of the four HV- pins of the connector body and bent under the PCB (Fig. 3.47 shows the HV connector, the HV cable and the brass strip). A M2.5 × 4mm brass or stainless-steel screw is used to lock the HV connector in the design position and connect electrically the ground of the connector to the ground of the DP or the lateral frame. Once the PCB is assembled with the brass strip and the HV cable, this latter is inserted into the HV hole of the lateral frame. A plastic feedthrough guides the wire toward the cathode plane. A drop of epoxy glue is inserted into the hole where the cable is inserted and the connector is pressed against the internal frame by means of the Kapton and left until the glue curing. Then the cable is welded to the cathode and the brass screw inserted for the ground connection and to mechanically fixes the connector in the design position. A layer of epoxy glue is spread on the HV PCB to insulate its pads and the copper track.(Fig. 3.46 shows the HV connector mounted on the DP). Soon after the connections between the HV connector and the panel is checked using a multimeter. Then the hole into the cathode is filled up to top with epoxy glue to make the panel gas-tight again. To check the gas tightness the dedicated gas leak closing cap B is used.

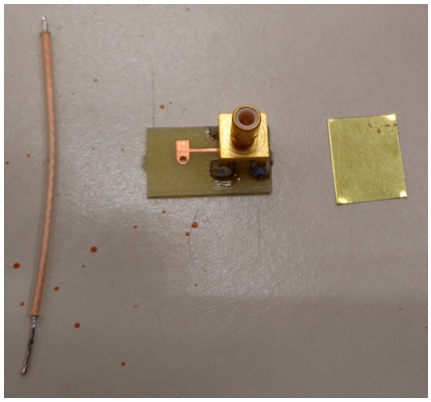

Figure 3.46

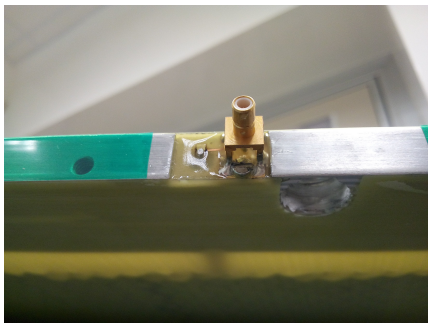

Figure 3.47

Figure 3.48

Finally, the 5 PCBs are electrically connected to each other to form a single cathode plane. Each PCB is connected to its adjacent by two electrical connections. The single connection is realized using 1 mm wide, 0.05 mm thick and 10 mm long, copper strip welded at both extremities to the panel pads. The weld is made flat and without any tip. The thickness of the weldering is typically inferior to 0.5 mm (Fig. 3.48). Then all the electrical connections (PCB-PCB, HV connector-cathode, mesh-frame-lateral frame, gas distribution pipe-lateral frame) are checked for continuity by means of the Digital Multimeter Fluke 116®.

3.4.11 HV Test

In order to verify that the electrical insulation between the DP cathode surface and the DP internal frame meets the ATLAS specification, i.e. it is greater than or equal to 50 GΩ, the so-called HV test is performed on each individual panel. The drift panel is therefore connected to a continuous voltage generator (HV power supply CAEN® SY546/A547) whose current resolution is equal to 1 nA. The generator voltage is set at 500 V (about 0.67 times greater than the working voltage of the detector drift region) with a ramp up of 10 V/s and a maximum current set to 150 nA. The DP works like a capacitor. At the end of the ramp up, after a certain electrical transient, the potential difference between DP cathode surface and internal frame tends to stabilize at the same voltage set on the generator, while the current gradually decreases until it stabilizes around to a minimum value. The main parameters to consider when carrying out the HV test are the relative humidity and the moisture present in the insulating material (FR4 and epoxy glue are higroscopic materials). In fact the excess of humidity can compromise the test. Unfortunately these are parameters that can hardly be kept under control since the DPs preparation and storage, as well as the HV test, do not take place in a clean room. The HV tests gave better results when at least 3/4 days passed from the last application of glue on the DP and when the tests were performed on days with a low relative humidity, typically less than 30%. Under these conditions (dry glue and RH $< 30\%$) the electrical transient is short. In fact, 5-7 minutes are enough so that the leakage current reaches values below 10 nA at a voltage of 500 V which corresponds to an insulation value equal to 50 $G\Omega$. If this result was not obtained on the panel, the test was repeated a few days later.
As an example we report the Fig. 3.49 that shows the leakage current recorded after 10 minutes test (ramp up + electrical transient) for 21 different DPs as a function of the relative humidity. There are two distinct areas: for RH $< 30\%$, the leakage current falls below 10 nA, for RH $> 30\%$ the current oscillates between 14 and 10 nA. A higher relative humidity leads to a small increase in leakage current.

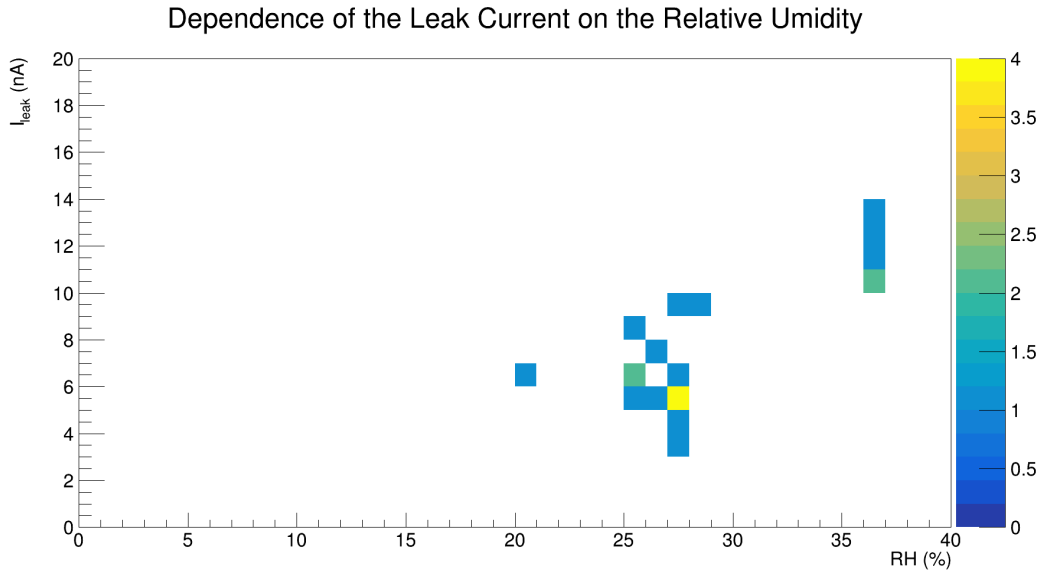

Figure 3.49: The bi-plot shows the leak current I_{leak} dependence on the relative humidity. For RH $< 30\%$ the leak current reaches values below 10 nA in a short electrical transient.

3.4.12 4 O-Rings Making

The 7 mm cross section diameter elastomer cord is delivered to the LAE in 100 m length rolls. The first step is cutting, mean a scissor, the cord in shorter strings ($\simeq$ 5900 mm for SM1 and $\simeq$ 5350 mm for SM2) with not clean ends. This operation is carried out with the aid of a 6 meter long V-shaped template in which the rope is carefully laid and then cut to the desired length.
Before joining the string ends it is necessary to make an ortogonally clean cut on each end of the string. We make this using a guillotine, a razor blade and propanol to lubricate the parts (Fig. 3.50a). After that we check the string ends match each other. If the ends match well, we move on to the next step.
We use the CONTI SECUR BFA® adhesive system for cold bonding applications to make the joints. We spread a thin adhesive layer on each string end three times, taking care to cover the entire edges surface. We wait 15 minutes between one application and another (Figg. 3.50b, 3.50c). Immediatly after the last glue application we plug in the string ends, put the part of the string with the joint in a closed mold (Fig. 3.50d) and leave to dry for 48 hours (Fig. 3.50e).

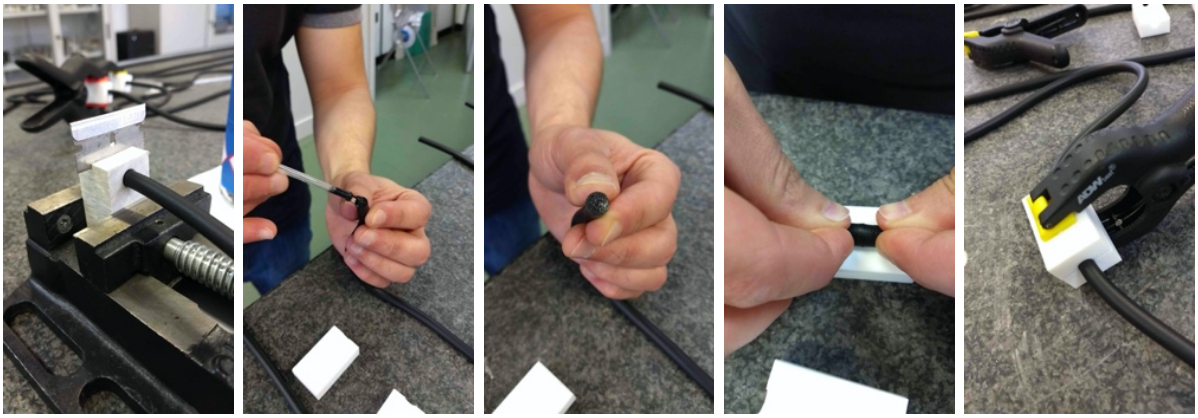

(a) (b) (c) (d) (e)

Figure 3.50: The O-Ring joint execution process.

Once the O-Ring joint has been made we check its regularity (absence of cracks and groove) by mean of the Dino Lite Microscope®. Then on a sample basis (one every 20) the O-Ring is placed in a test stand to verify its airtightness. Fig. 3.51 shows the test stand, which is capable to contain the entire length of the O-Ring (two test stands have been developed, one capable of accommodating the O-Rings for SM1 and another capable of accommodating the O-Rings for SM2). The volume enclosed by the O-Ring is about 100 ml for both test stands. Once the O-Ring was put into the test stand the volume is filled with 2 ml of air by means of a syringe and the pressure drop recorded for 10 min. Then the air leak rate is estimated as in the case of the local GTT.
Fig. 3.52 shows the result of a long-term air tightness test of one of the first produced O-Ring. It remained into the test stand for more than 2 months and time to time the air tightness checked. No degradation in air tightness was observed, demonstrating the goodness of the O-Ring joint execution process.

(a) (b)

Figure 3.51: (a): the path of the O-Ring inside the air tightness test stand. The groove is formed by synthetic glass 5mm height and 7mm wide. The white corners were developed using a 3D printer. (b): the test stand closed with its cover during the test. The same read-out electronics as for the local GTT were used.

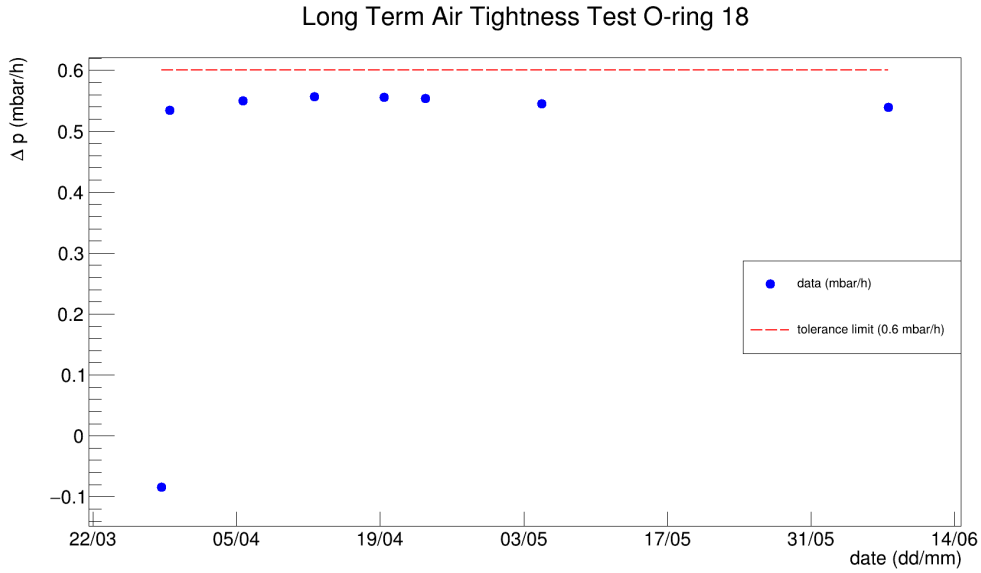

Figure 3.52: The result of a long-term air tightness test of one of the first produced O-Ring. The dashed red line show the ATLAS limit.

3.5 Micro-mesh Preparation

To avoid amplification gap inhomogeneities, due to sags between the pillars or to wrong positioning, the mesh must be properly tensioned and then glued on the mesh-frame. An excessive tension can induce large deformations in the panels and in the final module, and on the other hand a modest tension would give rise to significant sags. A nominal mesh tension in the range $7 - 10$ N/cm with a uniformity of $\pm 10\%$ is required for the mesh mounted on the DP just before the module assembly. The uniformity is defined as RMS/Average evaluated on the map of the measured mesh tensions.
For the SM1 modules (including prototypes and test modules) a total number of 175 meshes has been produced. The meshes are prepared in the laboratories of the INFN Roma 3 Section, where a dedicated clean-room has been built, along with specific equipment. In the preparation process each mesh is stretched to the desired tension, glued on an aluminum transfer frame, prepared with holes where the interconnections must pass through (punching), and finally packed and ready for shipment to LNF where they are washed and then glued onto the DPs.

3.5.1 Transfer Frame and Mesh Stretching

The transfer frame holding the tensioned mesh before its integration in the panel, has been designed according to the following prescriptions: it should be light enough to allow manipulations by two people without the use of a crane; its dimensions should be minimized for easy handling and interventions on the mesh surface, so that a trapezoidal shape, following the perimeter of the DPs could be the best choice; and finally it should be stiff and minimise the distortions induced by the tensions of the mesh.

Figure 3.53

Its design has been finalised after mechanical finite elements simulations, limiting the deformations to less than 300 μm for a mesh tension of 10 N/cm. The layout of the trapezoidal frames is shown in Fig. 3.53. Twelve aluminum transfer frames have been built to cope with the mesh production rate in Roma 3 and the workflow of mesh shipments to LNF.
For the tensioning of the meshes, a dedicated stretching table was built. As shown in Fig. 3.54, it is equipped with a total of 28 clamps, each 330 mm long, placed along the four sides.
Short sides have 5 clamps while long ones have 9 clamps. Only half of the total clamps are equipped with load cells and can be pulled, the remaining clamps (on the opposite sides) are fixed on the table. Moving clamps can be independently pulled through screwing nuts. Load cells are employed to measure the applied pulling force, which is acquired by an Arduino based DAQ system, then monitored live on a display and stored on a computer. During the process, the map of the tension of the mesh is regularly measured with the Sefar Tensocheck® 100 digital gauge. After a first regulation, the clamps are iteratively adjusted until the desired average value and uniformity are reached ("Step-1"). Then the transfer frame is raised from below until it touches the mesh on its perimeter for the gluing. Unavoidably a pressure on the mesh is applied, and a new map of the mesh tension is taken checking (and in case adjusting) the new values reached ("Step-2"). The

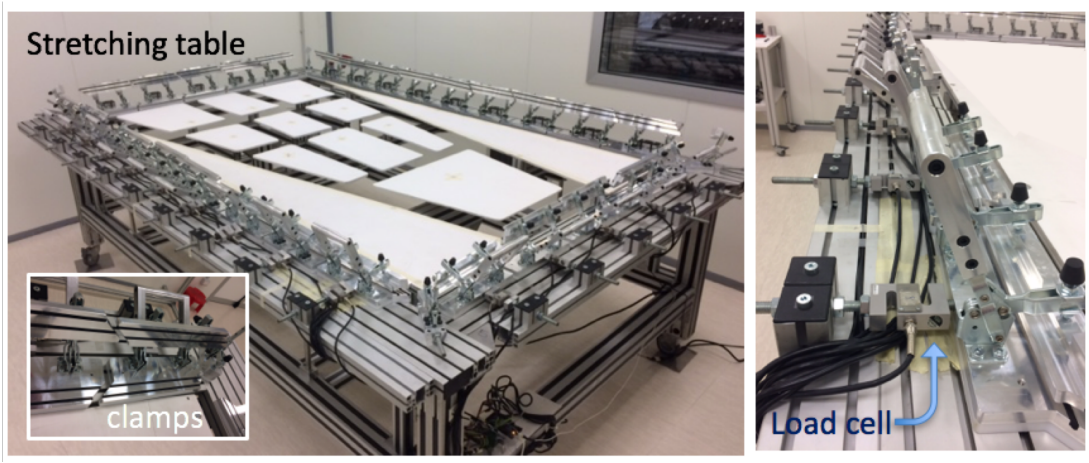

Figure 3.54: Overview of the mesh stretching table. The load cells and the clamps are shown in more detail.

mesh is then fixed on the transfer frame brushing the Ultrafix Plus Red® glue. When cured (after 5 hours), the clamps are released and the map of the mesh tension in this last step is taken ("Step-3"). After the clamps are released, the force of the mesh tension is transferred from the clamps to the frame, which slightly deforms, resulting to a decrease of the average tension of the mesh. The plots in Fig. 3.55 show the average tension and the uniformity reached for all processed meshes for the full production of the SM1 modules as a function of a mesh identifier related to the chronological sequence of production in the "Step-3" outlined above. The plots clearly show a "learning curve" as for the first ≃20 produced meshes, the average tensions are subject to larger variations and uniformities are slightly worse. Considering the final step (Step-3) of the mesh preparation on the transfer frame (deliverable of the Roma 3 Lab), an average tension of the full production, after the first 20 produced meshes is very stable around 8.2 N/cm; the average uniformity is about 6 % well within the requirements.
A systematic trend is observed in the average tension map for the meshes after initial stretching (Step-1) and on the transfer frame (Step-3) obtained by averaging over all production meshes. While in the stretching table on average slightly higher tensions are obtained in the central area, after lifting the frame, gluing the mesh and releasing the clamps an average higher tension is obtained close to the two bases of the trapezoid. In any case the RMS, as already shown in within specifications.

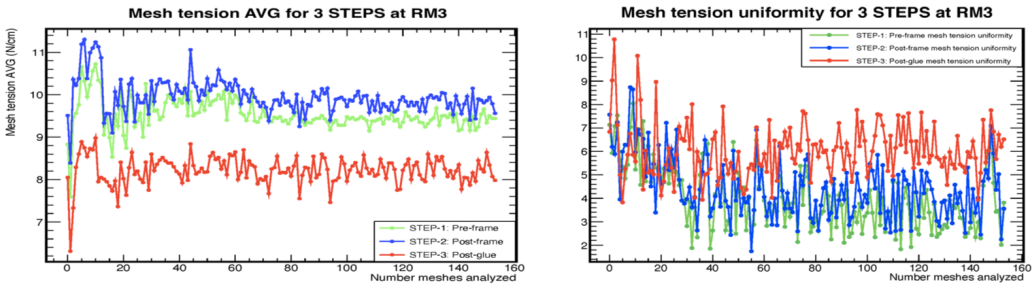

Figure 3.55: For all meshes stretched in chronological order (left) average tension and (right) average uniformity. The different colors correspond to the three steps in the stretching procedure described in the text.

3.5.2 Mesh Punching

The preparation of the meshes also includes their perforation in four positions allowing for the interconnection passing through the panels in the assembled quadruplets. The holes on the meshes are done with a punch through tool after local passivation of the mesh. These operations are carried out on a dedicated trapezoidal table also equipped with an alignment system and targets to properly define the locations of the holes on the mesh. The passivation, to prevent mesh fraying and/or filaments to stick-out, is obtained with a little drop of Araldite 2020, first dispensed on a tedlar foil, and then pressed and left curing on the mesh, with 5 kg weights (Fig. 3.56). The mesh punching is done after passivation (Fig. 3.57). It can be seen that the final hole is cut very precisely (Fig. 3.58, the rim edge is very clean and there are no loose wires that could create discharges within the amplification gap. A quality control measurement is made on the height of the removed (cut) circle of the passivated meshes in order to be sure that the thickness of the glue is as expected. In average, a mean value of about 79 μm is obtained for the full production, hence about 19 μm of glue are added to the 60 μm thickness of the non-passivated mesh. In the assembly of the panels this results in about 10 μm increase of the amplification gap, a small localised increase around the interconnection.
After the punching, the meshes are protected with polyethylene foils, sealed and stored on the transfer tray, ready for shipment to LNF.

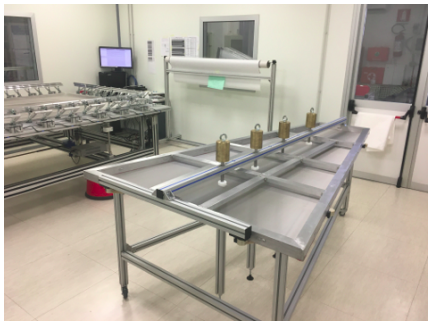

Figure 3.56

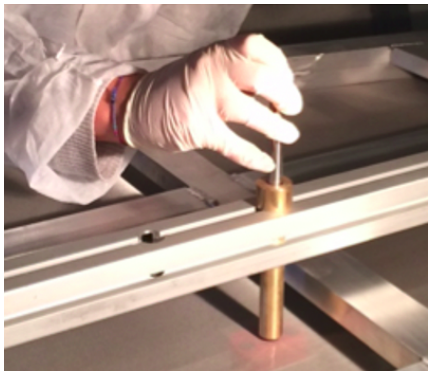

Figure 3.57

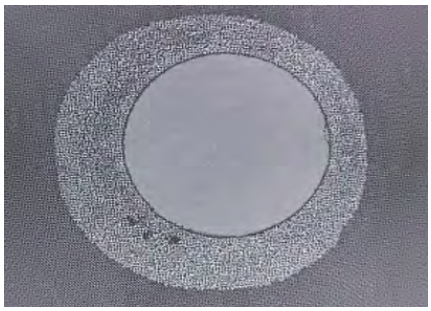

Figure 3.58

3.6 Drift Panel Finalization

The last step of DPs construction is performed in a clean room at the LNF, the so called CR2 where the DPs prepared at Cosenza are equipped with the washed meshes already stretched at Roma 3 (see Appendix C for the mesh washing procedure).
Two trapezoidal tables have been specially built for gluing the mesh. They have the same shape and dimensions of the drift panels. The tables can accommodate both an outer or a central drift panel complete with a mesh. In correspondence with the bases of each table there is an aluminum support connected to a system of screws that allows them to move up and down. Each table is also equipped with 6 screw clamps (2 for the minor base, 2 for the major base and 1 for each oblique side) that allow us to hold the transfer frame in the correct position during the mesh gluing phases.

Figure 3.59

The DP is placed on the trapezoidal table. A visual inspection and a check of the electrical connections is performed on the panel. A rapid dry test is performed first by placing the transfer frame on the two raised supports of the trapezoidal table in order to check the correct alignment between the mesh punched holes and the DP interconnection holes. The DP surface and the mesh frame are cleaned with isopropyl alcohol. The anti-static roller is then passed both on the DP cathodic surface and on the face of the mesh that will couple to the cathode. The glue (Araldite 2011) is distributed through a special dispenser along the entire knurling surface of the mesh frame. When the glue takes on a transparent and uniform color, the transfer frame complete with mesh is placed on the raised supports of the trapezoidal table. The table supports are then slowly lowered until the mesh rests on the mesh frame, obviously taking care to align the mesh punched holes with the interconnection holes (Fig. 3.59). The six clamps are then positioned so as to hold the transfer frame in place (Fig. 3.60). A first mapping, or step-1 mapping, of the mechanical tension of the mesh σ is then performed with the same type of digital gauge used at Roma 3 following the map shows in Fig. 3.61. This step allows us to adjust the tension of the mesh to the ideal value by acting on the transfer frame by means of the clamps. Once the best configuration is reached, the mechanical tension values are recorded. After some glue has passed through the mesh (the time it takes for the glue to pass through the mesh depends on the ambient temperature, but is generally 10-15 min) it is spatulated outwards. After 24 hours of glue curing in the CR2, the transfer frame is removed cutting the mesh along the transfer frame perimeter, and then the mesh is

Figure 3.60

cut accurately along the external edge of the mesh frame, smoothening any sharp point by mean of the cutter blade and 1000 grade fine sandpaper. Finally, the second and last (step-2) mapping of the mesh mechanical tension is performed following the same map of the step-1 measurement.
Fig. 3.62 shows the step-1 and step-2 distributions of the mechanical tension measured for 128 meshes (i.e. 64 ODPs and 32 CDPs). A slight relaxation of the mesh is evident, and expected, between the two measurements.

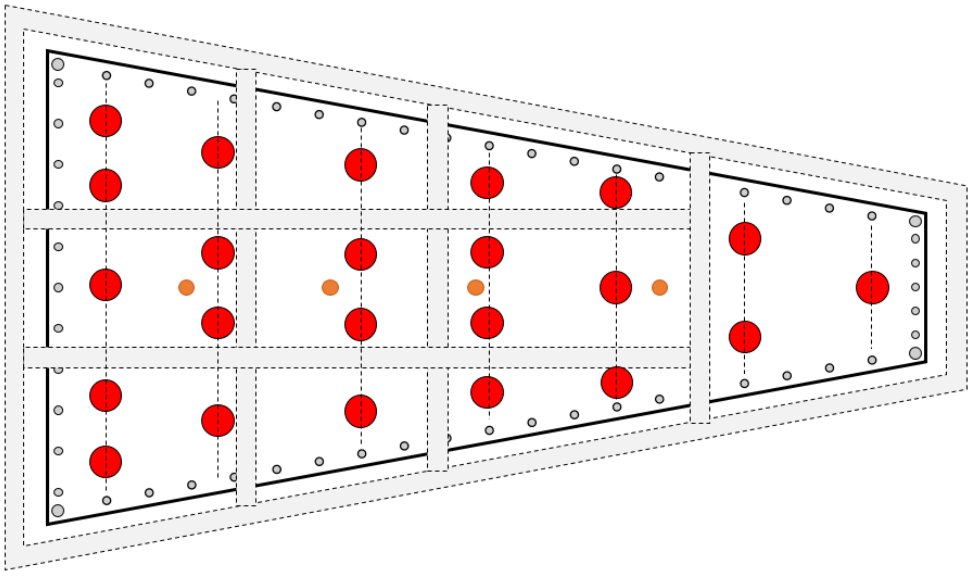

Figure 3.61: Mechanical tension map drawing. The red circles indicate the 23 points of the mesh where mechanical tension measurements are performed both before and after mesh cutting.

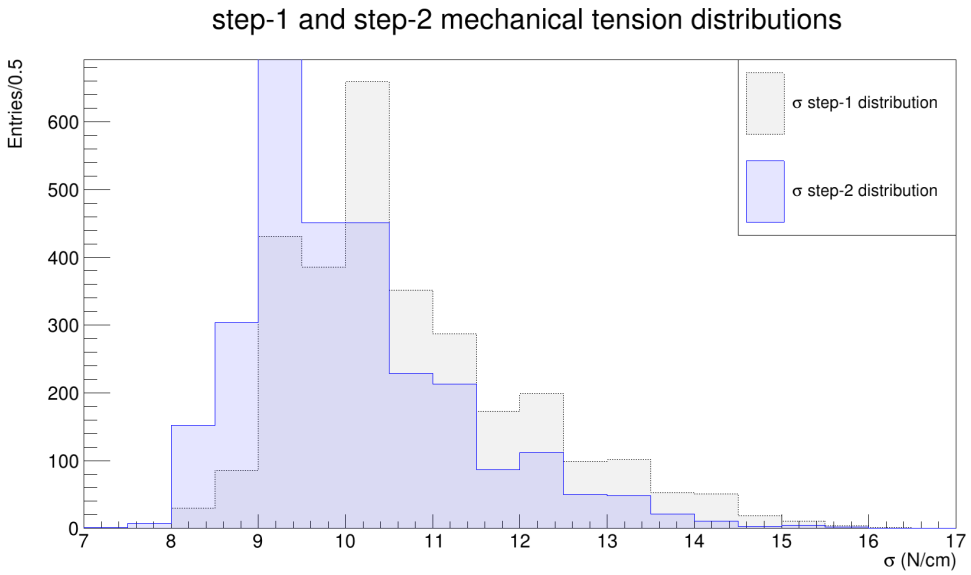

Figure 3.62: Mechanical tension distributions for 128 meshes before (gray) and after (blue) the cutting. The second distribution is shifted towards lower mechanical tension values.

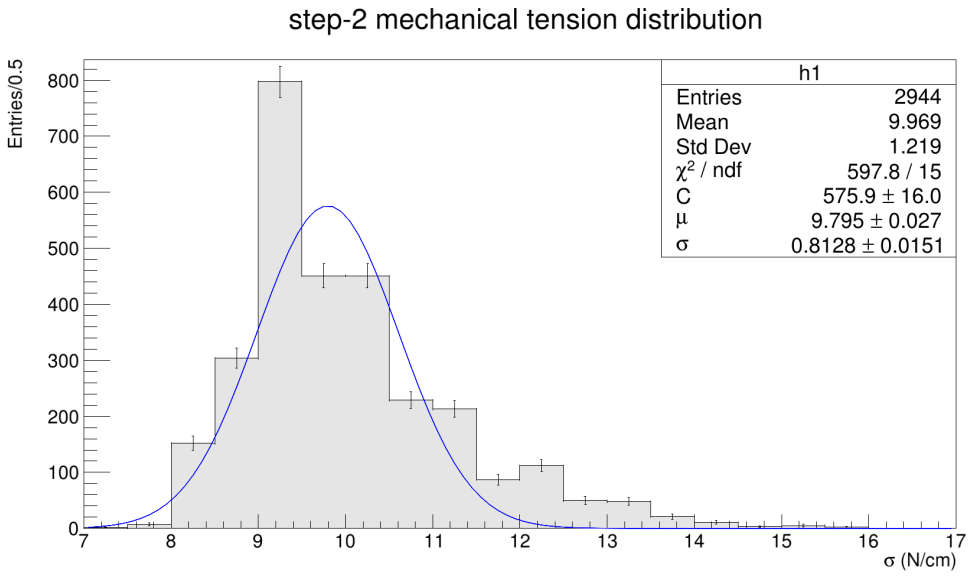

Figure 3.63: Mechanical tension distributions for 128 meshes after the mesh cutting. The average measured tension and its RMS are (9.969 ± 1.219) N/cm. The average uniformity is about 12%. From the gaussian fit we obtain an expected uniformity of about 8%.

Fig. 3.63 shows the step-2 mechanical tension distribution for 128 meshes. The average tension value is very close to 10 N/cm and the average uniformity is about 12%, significantly worse than the last measurement performed at Roma 3. The tension uniformity obtained from the gaussian fit is about 8%. This discrepancy is mainly due to the sistematically higher values of the mesh mechanical tension near the minor base and near the corners of the major base.
Before being assembled inside the 4-plet, the DP complete with mesh is again subjected to a high voltage test (same as described in the subsection 3.4.11) in order to verify the correct insulation between the mesh and the cathodic surface of the panel. Fig. 3.64 shows the drift panel finalized on a trapezoidal table.

Figure 3.64: An ODP complete with mesh on the trapezoidal table.

3.7 SM1 MM 4-plet Assembly and Quality Control

In this subsection we will describe the SM1 MM 4-plet assembly procedure and quality tests.

3.7.1 Micromegas 4-plet Assembly Procedure

After the preparatory phases described in Section 3.8 and in the Appendix C the five finalized and certified panels (ODP - STEREO ROP - CDP - ETA ROP - ODP) are assembled to form the 4-plet. The assembly of a full MM 4-plet is done in a dedicated clean room at the Frascati Laboratories, CR1 in the following, and takes about one week including all the assembly steps and the intermediate HV tests performed at each gap closure.
The assembly starts from the gap which represents the layer 4 in the SM1 nomenclature. The ODP is positioned on the stiff-frame placed on the granite table (see Fig. 3.65). The stiff-frame is a structure made with Al profiles glued with Al brackets with mechanical tolerances of 100 μm, and is used to guarantee the panel planarity during the assembly procedure. The panel is aligned to the stiff-frame border using adjustment screws. The stiff-frame with the panel is then moved on the assembly tool mounted on the granite table. The ODP is then put in vertical position on the granite table as shown in Fig. 3.65.

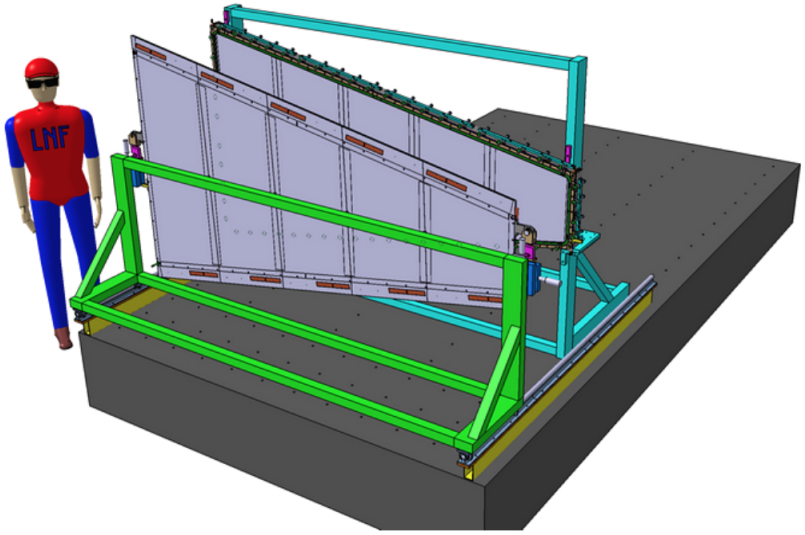

Figure 3.65: Schematic view of the Frascati assembly station during the assembly of layer 4. The external drift panel with the stiff-frame is mounted on the assembly tool (blue structure). The stereo RO panel is mounted on the assembly cart (green structure) on the sliding tracks.

The Or is inserted in its seat.
The stereo ROP is put in vertical position on the assembly cart, which is a movable assembly tool mounted on a trolley. The trolley is aligned with the rails on the granite table in which the cart have to slide. When both panels are in vertical position, a dry cleaning procedure is performed on the panel surfaces, removing the dust before with a vacuum cleaner and then with an anti-static roller. It should be noted that the choice of assembling the 4-plet keeping the panels vertical decreases the probability that the dust will settle again on the panel surfaces. The cart with the ROP slide along the rails to

approach the DP. To align the ROP and the DP, two Delrin 16 pins of 6 mm diameter are inserted in the holes for the closure of the gap.
The capacitors of the HV filters installed on the ROP are tested connecting the HV of each section of the layer. Then the two panels are connected using expansion rods (Fig. 3.66), on half of the screw holes. The expansion rods are designed to be fixed by turning the screw on one side and locking them with a wheel on the other side. In this way the panels are fixed and the Or compression is ensured without leaving metallic dust inside the gap.

Figure 3.66

When the first gap is closed, the HV test in air is performed. This test consists in carrying out a ramp up of the anode voltage from the value of 400 V until reaching voltage values equals to 750 V, higher than the detector operating voltage and requairing current values smaller than few nA. The purpose of the test is to verify the absence of imperfections in the amplification gap before closing the singlet. Good sections quickly reach stable voltage values, bad sections cause discharges with consequent current flow and voltage instabilities. It is possible that these discharges are determined by the presence of patches of humidity on the resistive layer or by the presence of impurities on the cathode mesh or on the resistive layer. To exclude the first issue, it is sufficient to introduce a flow of gas, e.g. N_2. For the second issue, it is possible to lengthen the HV conditioning times by trying to "burn" the dirt. If, after performed these two operations, the section continues to show instabilities, the singlet must be re-opened, check the absence of defects on the surfaces and than clean it again.
The procedure described for the first gap is repeated also for the other gaps, paying more attention to the alignment of the eta layers wrt the stereo layers. Before the 4-plet completion and the closure with the final screws, the gap is again closed with the expansion rods and interconnection plugs completed with Or are inserted on both sides of the module to minimise the gas leakage. A preliminary HV test in Ar:CO_2 is performed, ramping up the HV value up to 550 V. The test is not performed up to the operational HV value of 570 V given that the RH value in CR1 is usually quite high ($\simeq 40\%$) and the gas tightness of the module is not optimal. If the module passes this preliminary HV test, the expansion rods are substituted with the final screws. The chamber is then dismounted from the assembly tool and set in horizontal position on a granite table to start the QA/QC tests.

3.7.2 4-plet QA/QC

4-plet assembly is followed by validation tests. In particular, is checked the 4-plet thickness or planarity, its gas tightness, the alignment of the strips, the stability in HV operation and its efficiency.
The 4-plet thickness/planarity is measured when the chamber is on the granite table by means of the laser tracker Leica TD 840®. A height map with about 3000 points for each face of the chamber is carried out. From the cloud points a planar fit is performed to reconstruct the chamber surface wrt the reference plane (see Fig. 3.67). The thickness and the planarity of the chamber are extracted respectively from the mean value and from the RMS of all the measurements. Out of the total number of assembled chambers, only a few faces showed an out-of-spec planarity of 200 μm.
The 4-plet gas tightness test is performed by means of the pressure drop method. After

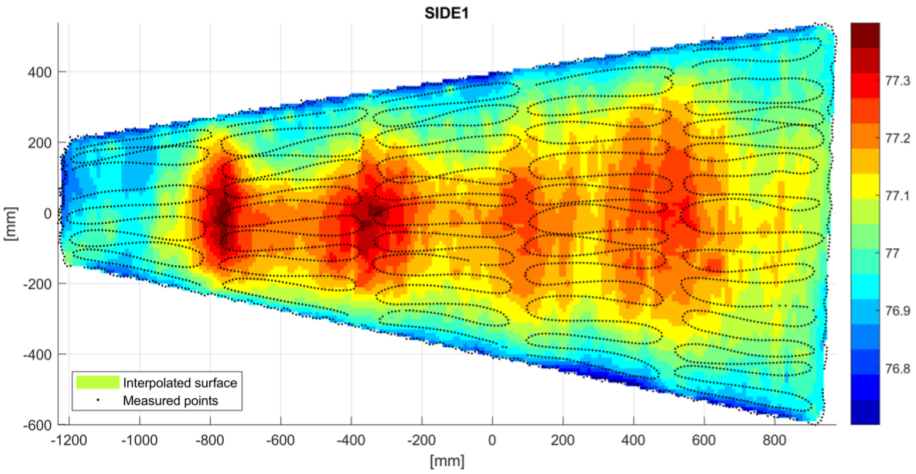

Figure 3.67: SM1 MM chamber planarity measurement with the laser tracker.

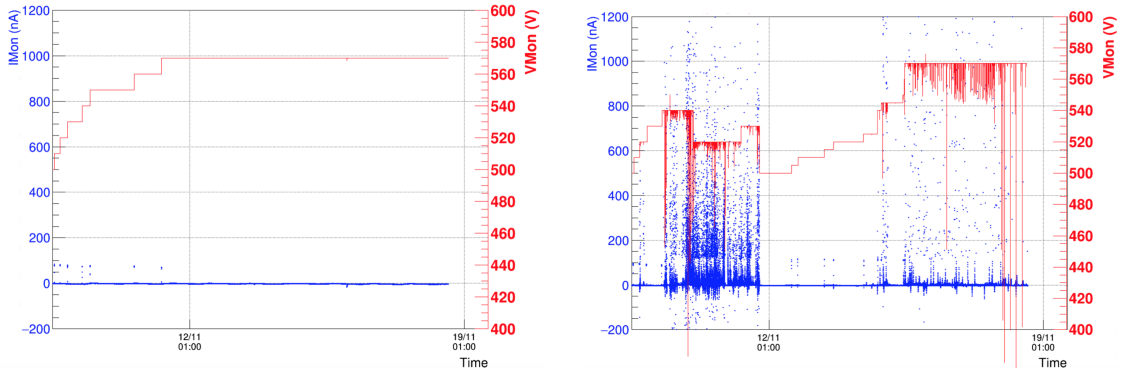

ht!

(a) (b)

Figure 3.68: Example of two distinct HV section behaviour. (a). A good section. The ramp up in HV is not accompanied by draw current and discharges. (b). A seriuosly problematic section.

reaching the overpressure of 3 mbar by inserting 300-400 ml of gas, the pressure drop is monitored for about 15-20 min. In this short period of time, both the temperature and the atmospheric pressure are considered constant. All the assembled chambers showed a pressure drop below the ATLAS limit and therefore less than 0.6 mbar/h.
The strips alignment from layer to layer and from panel to panel is done via the 4 channel rasfork tool [46], exploiting the localization precision of the Rasnik masks arranged on the RO-PCBs. From the reading of all 30 precision Rasnik masks, the map of the misalignments is performed and then used to reconstruct the chamber geometry and implemented in the reconstruction of the tracks.

The HV stability test is performed outside the CR1, in the area of the cosmic-ray-test stand. The HV is supplied to the detector anodes through the 40 independent HV sections. The 4 cathode channels, one per drift layer (2 external and 2 central), are supplied with the nominal -300 V value. The meshes are grounded.
The more interesting parameters, i.e the monitored HV (V_{mon}) and the monitored current (I_{mon}), are recorded. The HV test is performed flushing the chamber with a 20 l/h of

Ar:CO_2 (93:7) gas mixture. Then each section is ramped up by steps from 400 V to the operational value HV_{max} = 570 V. The time necessary for the sections to reach HV stability for each ramp up step depends on several factors that will analize in Section 3.8. For a good section 3.68a the HV stability achievement, for each ramp up step, take about 5-10 min. For problematic sections 3.68b the times are extended and, in several cases, can not reach the HV operational value. The identification of the maximum HV value at which a section is stable is based on the drawn current and by the spark rate, defined as the frequency at which I_{mon} goes above the defined current threshold of 100 nA. Since the current is sampled every second, the spark rate is defined as the number of seconds with a current exceeding the threshold in one minute. When the spark rate exceeds the value of 6/minute, the HV is lowered until a stable condition is reached. To meet the ATLAS HV acceptance requirement for a SM1 chamber, at least 85% of the sections (34/40) must be stable at the nominal HV value of 570 V.

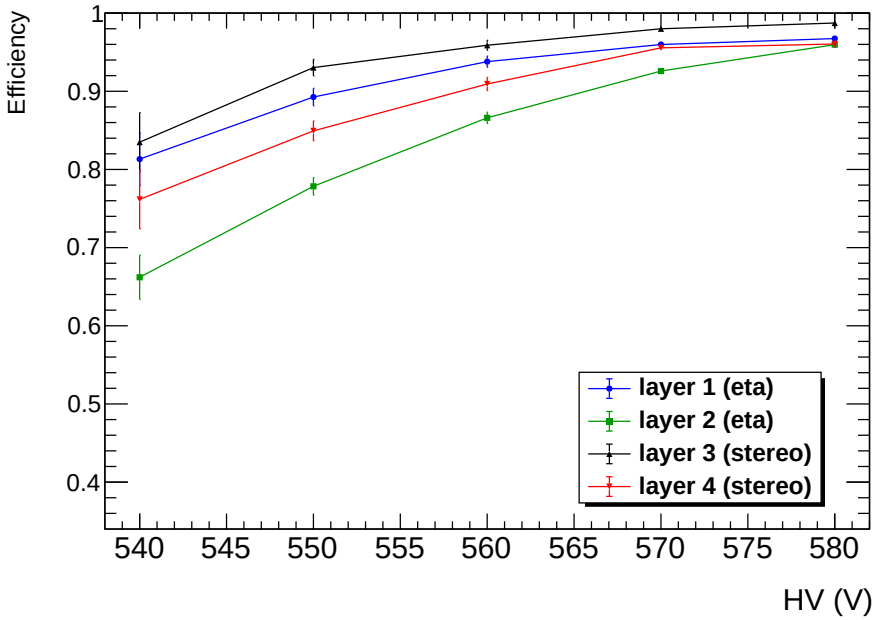

Figure 3.69: Efficiency as function of the anodic HV for the four RO layers of a SM1 chamber, operated with the standard gas mixture Ar:CO2 (93:7).

As final QA/QC step, the SM1 MM chambers are installed in the Cosmic-Ray Stand (CRS) composed by: two upper planes of plastic scintillators; a 35 thick iron absorber plate providing an energy cut of 0.6 GeV; the MM chamber; two lower planes of plastic scintillators. The trigger is provided by the four planes of scintillators, covering an area of about 1 m^2 each.
In order to compute the tracking efficiency in a RO layer, a track is reconstructed in the other 3 RO layers, being the so called control layers. Only events with one and only one cluster in each control layer are considered. Then a possible cluster in the RO layer under study is compared with the position of the track in that layer. The total surface of the RO layer is divided in 50 bins of 43 mm each in the precision coordinate. Defining N_i^{trk} as the number of tracks extrapolated in the i-th bin and N_i^{clu} the sub sample for which a cluster is found in a window of a given size, the RO layer efficency is defined as:

$$\epsilon_i^{layer} = \frac{N_i^{clu}}{N_i^{trk}}$$

Fig. 3.69 shows the efficiency as a function of the HV. For all the 4 layers of a typical SM1 MM module, $\epsilon >$ 90% starting from HV = 560 V. At the nominal voltage of HV_{max} = 570 V, efficiencies in the range (94, 98)% are obtained. For all the built SM1 MM modules, the overall efficiency is above 90% whith an operating voltage equals to HV_{max} = 570 V using Ar:CO_2 (93:7) gas mixture.

3.8 SM1 MM HV instabilities

The main problem that afflicted the entire production phase of all NSW MM 4-plets is the HV section instability characterized by discharges beetwen mesh cathode and anode strips with consequent anode current of intensity even of the order of μA. An unstable section limits the detector operating HV to values lower than the working point, thus giving rise to a non negligible efficiency loss and in the worst case involves the non-operability of the detector. The origin of these discharges is to be associated with several detector weak points, such as

1. the presence of spikes and other imperfections on the cathode mesh surface;
2. impurities on the electrode surfaces resulting from industrial processing and the inevitable manipulation of the detector components during the construction phases;
3. presence of moisture and other contaminants within the active region of the detector;
4. resistive layer issues.

A qualitative description of the listed issues and the solutions adopted in order to reduce their impact on the detector HV stability will be given below.

3.8.1 1. Mesh Pointy → Polishing

Fig. 3.70a shows the numerical simulation of the electric field in the proximity of the mesh when a potential difference of 540 V is applied between the anode and the cathode mesh. A non-uniformity of the field is clearly observed, especially near the cylindrical surfaces. There the field strength can reach values close to 100 kV/cm. Fig. 3.70b shows a magnification of the mesh in which a tip with a length of approximately 8-10 m is evident. The radius of curvature of the tip will be approximately 1/100 of its length. ù This implies a further increase in the electric field near the tip and a further electric field uniformity degradation. This obviously increases the discharge probability. Moreover, in such a situation, an electron field emission is more probable (see e.g. [48]). In order to minimize the discharge probability, it was considered appropriate to perform a wet polishing with fine sandapaper (tipically grade 2000/2500) on the mesh cathode surface before the 4-plet assembly [45]. The procedure is carried out before washing the drift panel and takes about an hour for each mesh.

3.8.2 2. Impurities on Electrode Surfaces → Careful Cleaning Procedure

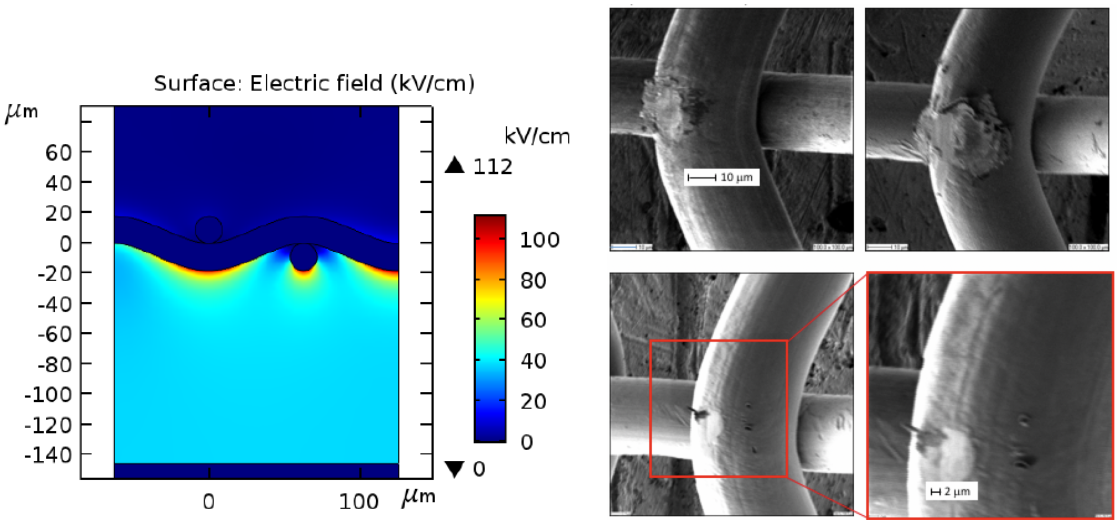

(a) (b)

Figure 3.70: (a): the surface plot, derived from a numerical simulation, of the electric field for a woven micro-mesh [6]. The figure is presented for illustrative purposes only. (b): the magnification of a micro-mesh that highlights a small tip.

In order to carry out a careful washing procedure, a special washing cabine (Fig. 3.71) is built, equipped with vertical supports capable of hosting both the mesh on the mesh frame and the single drift and RO panels.
For the mesh and therefore also for the DP complete with mesh, the focus was on eliminating the grease present on the mesh. A degreasing product was therefore used, i.e. NGL. Washes with NGL were followed by rinsing with hot tap water and then with deionized water.
As regards the RO panel surface, the main attention was paid to the elimination of impurities which could be found in the most disparate points such as for example at the base of the pillars or near of the pyralux rim or coverlay. In this situation it was preferred to adopt a detergent product containing micro-crystals, such as CIF, so as to facilitate the elimination of these deposits. Obviously, the washes with CIF were followed with rinses of hot tap water and then deionized water (see Appendix C for the complete washing procedure).
Then each panel, RO and drift, is transported and mounted directly in the drying station (Fig. 3.72), which is a custom-made structure able to host the 5 panels needed for a MM 4-plet in vertical position. The drying station, is equipped with a ventilation system to filter the air and keep the temperature around (38-40)° C. The panels are left to dry a minimum of two full days before 4-plet assembly. The 4-plet panels washing and drying procedure takes a total of 3/4 days to complete.

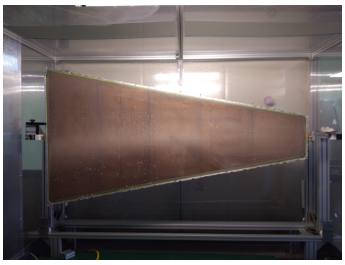

Figure 3.71

Figure 3.72

Note that a carefull washing procedure like the one adopted for the SM1 MM panels is not the only way to get clean detector electrode surfaces. During the NSW MM construction

different ROP cleaning techniques in the several European construction sites were tested, e.g. ethanol or NaOH baths and brushing treatment with pumice powder. Fig. 3.73 shows some details of impurities present on the base of the pillars or stucked in the mesh. The results of the cleaning operations on the pillars are also shown.
Even if all cleaning techniques showed good results in terms of dirt removal, a clear correlation with improvements in HV stability was not found.

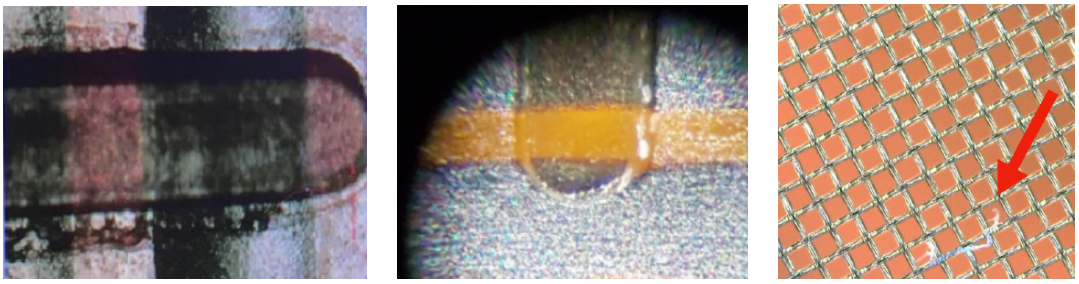

(a) (b) (c)

Figure 3.73: (a). A dirty pillar. (b) A pillar after an ethanol bath. (c). A thread stucked in the mesh. [37]

3.8.3 Contaminants → Gas Volume Changes

Outgassing studies [30] conducted on the main MM materials (Kapton, Araldite 2011, FR4, Cu, etc.) have shown a clear prevalence of H_2O. In fact, these materials have a non-negligible hygroscopicity. The water vapour affects the first Townsend coefficient of the gas mixture as shown by [6]: the humid gas mixture, at 45 KV/cm, has the same Townsend coefficient as the dry gas has at 55 kV/cm, with only 1000 ppm of water vapour. It is also known that the gas circuit is also a source of contaminants, mostly O_2 and H_2O. Moreover it was observed by T. Alexopoulos et al. [15] that there is a clear correlation between ambient temperature variation and the O_2 contamination inside the detector active volume mainly due to a drop in the Or sealing power.
In order to keep the moisture and other contaminant concentration at values that allow the good detector operation, it is advisable to carry out numerous gas volume changes before applying a high voltage to the electrodes. It has also been shown that by applying a flushing not less than 20 l/h, it is possible to keep the relative humidity inside the detector below 15-10% ensuring a good detector operation. Fig. 3.74 reports measured RH as a function of time on two SM1 chambers connected in series at the cosmic-ray-test stand. The gas mixture is monitored by a RH analog sensor, located at the output of each chamber. A clear reduction of the RH after the change of gas flux is visible, on top of the oscillations due to the day/night cycles.

3.8.4 Resistive Layer Issues → Edge Passivation or Grinding?

Since the first MM 4-plets HV conditioning a clear correlation emerged between the discharges and the RO-PCB resistive layer layout. Obviously the discharges preferred the regions of the layer with lower resistance values. Fig. 3.75 shows the effect of discharges in different regions of different resistive layers. All three regions are close to the silver line and/or close to the ladders. In particular Fig. 3.75c shows the effect of the discharges on the ladders away from the silver line.

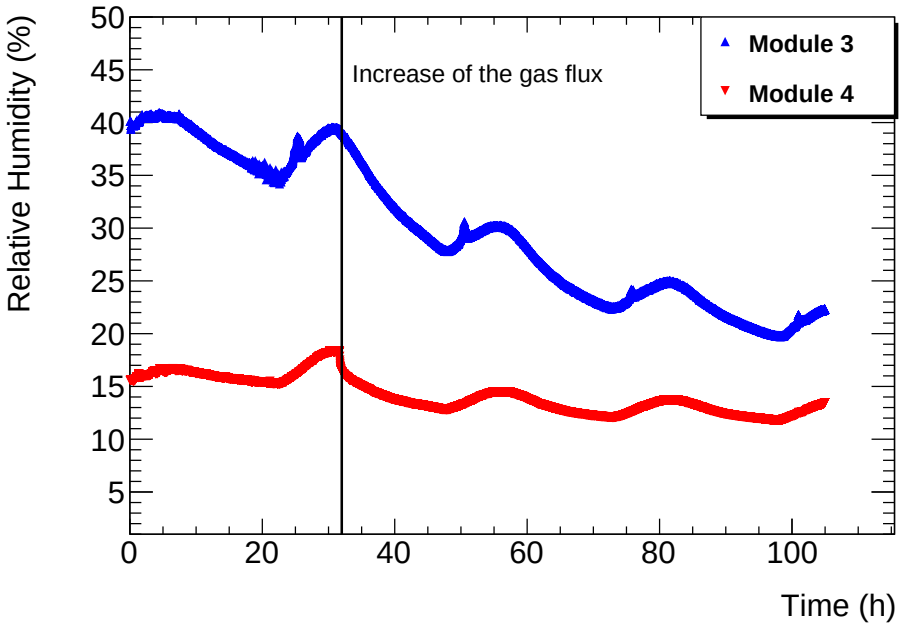

Figure 3.74: Measurement of the RH as a function of time of the M3 and M4 SM1 chambers connected in series (M3 → M4). The vertical line indicates the moment when the gas flux is increased from 10 to 20 l/h.

There also appears to be a clear difference in the resistive layout between the SM1 ETA and STEREO RO-PCB. In particular, the first column of ladders on STEREO RO-PCBs is closer to the silver line than in the case of ETA boards and in fact the number of STEREO problematic sections is higher than the ETA ones.
In order to better understand the relationship between discharges and resistive layout as well as the uniformity of the single strip resistance in all the employed SM1 RO-PCBs a systematic work has been carry out in LAE on 10 spare RO-PCB.
To measure the resistance between the silver line and the strip at a defined distance from the silver line itself, a multimeter and a probe capable of resolving the single strip are employed. The resistance measurement was carried out for all strips of a RO-PCB at a distance zero from the pyralux rim edge, while at a step of 1 cm (every 25 strips) for the distance from the coverlay 1, 2, ..., 20 cm.
Fig. 3.77 shows, as an example, the resistance value measured along the strip starting

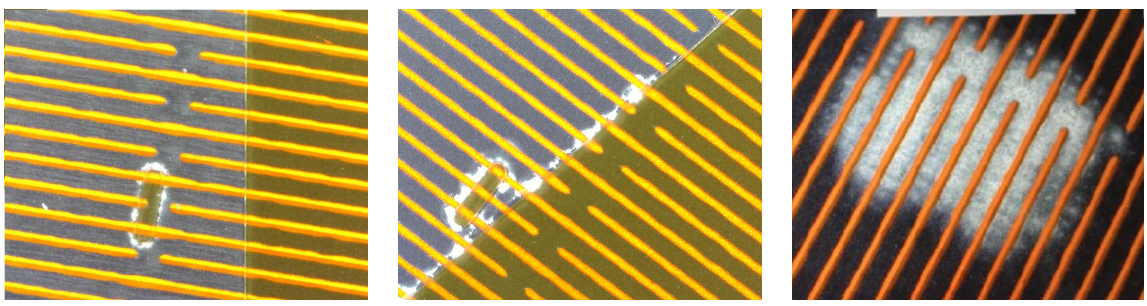

(a) (b) (c)

Figure 3.75: Magnification of three distinct region damaged by discharges. All three regions are close to the silver line and/or ladders.

from the pyralux rim. Measurements show clearly the effect of the ladder network, with an overall increase of the resistance moving from the pyralux rim or coverlay toward the center of the PCB and sudden drops in correspondence of each ladder. The arcs extend from one ladder to the next. At the end of the strip (close to the middle of the PCB) the periodical arc behavior disappears.
Fig. 3.78 shows the 3-dimensional plots of the single strip resistance value for eight different sections: $SS1_{086}$ L, $SS2_{103}$ L, $SE3_{097}$ L, $SE3_{097}$ R, $SE4_{098}$ L, $SS4_{095}$ R, $SE5_{120}$ L and $SE5_{120}$ R. The pedix number refers to the production bacth. Other resistance mappings have been made and are showed in Appendix B.

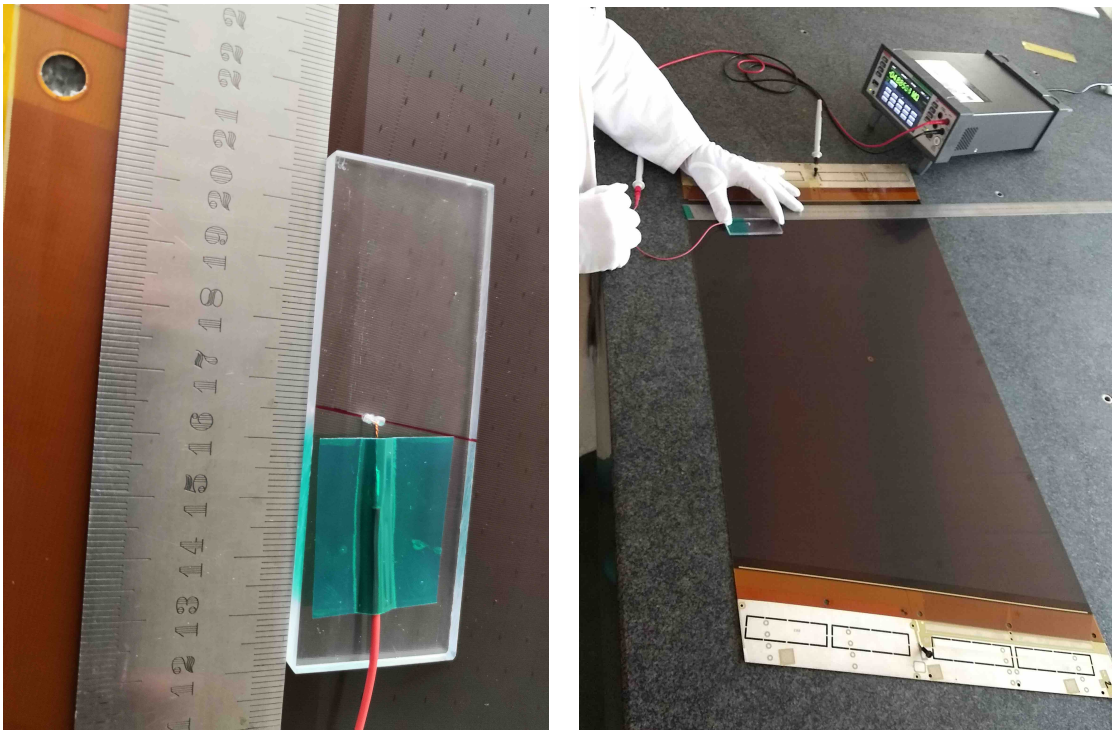

(a) (b)

Figure 3.76: (a). The probe: a copper wire of 0.19 mm in diameter passes through two contiguous holes, located 1 mm away from each other, present in the center of a plexiglass plate. On one face of the probe the wire exits from one hole and enters the other, while on the other side the wire is soldered to a connector. The probe is placed in contact with the PCB and the piece of wire 1 mm long is the electrical contact with the strip. The probe is placed next to and in contact with the ruler and made to slide along it (b). Probes have been built for each types of strips (eta and stereo) because the wire probe must be parallel to the strip to avoid that it touches the neighboring strips.

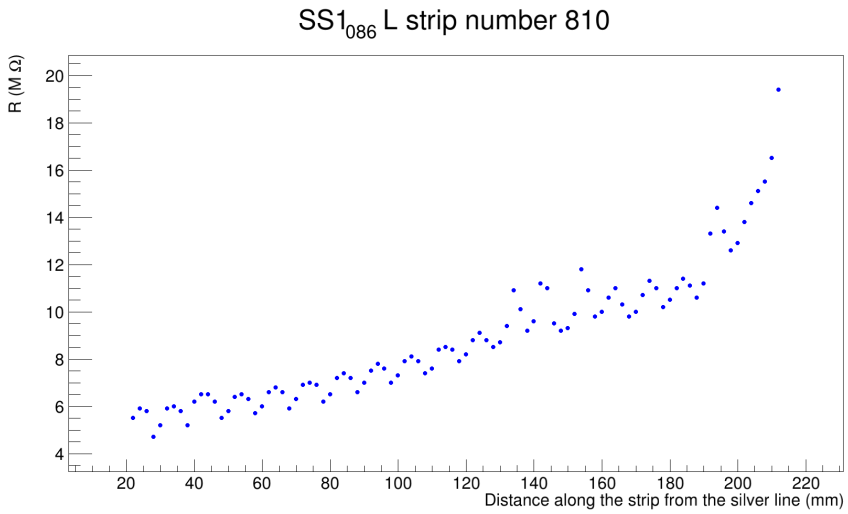

Figure 3.77: The electric resistance of one strip measured wrt the silver line as a function of the distance from the silver line itself. The arcs extend from one interconnection to the next.

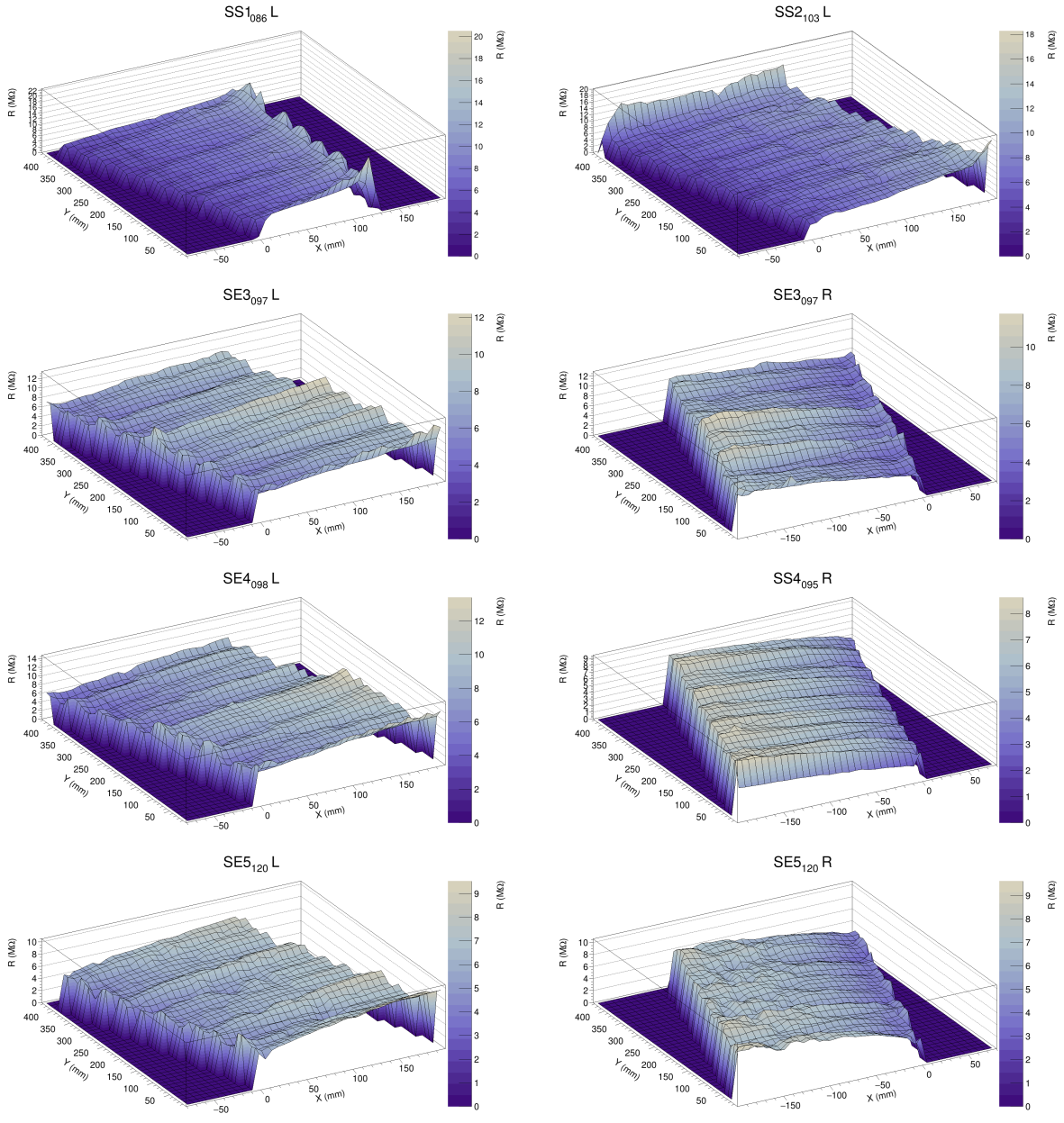

Figure 3.78: Resistance mappings for 8 distinct RO-PCB sections. Each 3-dimensional plot report as title the section ID.

From 3-dimensional plot we can deduce that:

- the arc trend due to the presence of the ladders is evident in all cases and the resistance values tend to increase moving away from the silver line;
- the defects of the resistive paste which alter the arc behaviour are also evident, especially for $SE5_{120}$ R;
- the smaller the section surface, the greater the average resistance values recorded, in fact it goes from a range of (0.5, 20) MΩ for SS1 section to a range of (0.5, 9) MΩ for SE5. This turns out to be a very trouble for the resistive layers of the other sectors, e.g. SM2, LM1 and LM2 which have much larger surfaces than the SM1 sections;
- resistance local maximums in the ETA sections near the pyralux rim are registered. This, as already noted, is due to the absence of ladders near the silver line, in fact the local maximums are not present in the STEREO sections.

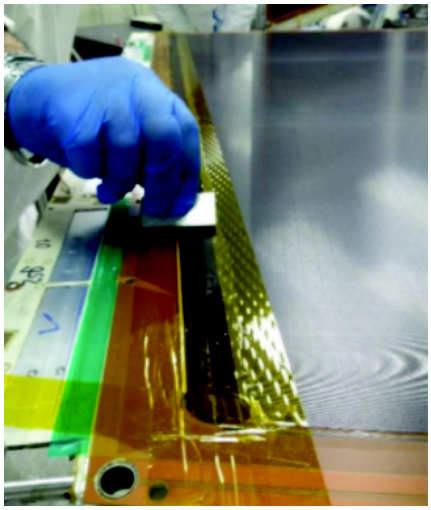

Figure 3.79

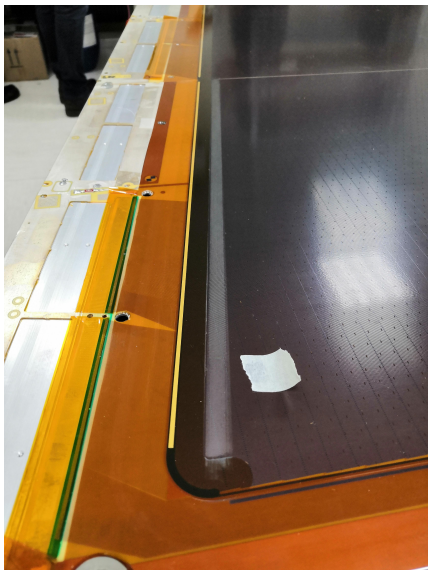

Figure 3.80

In order to mitigate the HV instability issues related to resistance layout, the so-called "edge-passivation" technique was introduce. The procedure consists in the passivation of a region along the side of the active area through the deposit of a thin layer ($\simeq 50\ \mu$m) of Araldite 2011. It is applied to the already build ROPs at the LNF. The passivated area running all along the sloped sides of RO-PCBs (see Fig. 3.79).
The resistance measurements prior the passivation is performed by means of a 1×1 cm^2 surface probe. The Fig. 3.81 shows typical resistance values measured for a spare RO-PCB using this probe. Obviously the probe short-circuits several strips and the arc behavior observed in the measurements on a single strip is considerably suppressed, but it is still distinguishable. The transverse extension of the passivation begins at the pyralux rim edge and ends where the resistive layer assumes values not lower than 0.8 MΩ. Typical values of transverse passivation extension are 0-1 cm for ETA PCBs and 1-3 cm for STEREO PCBs.
Obviously there are alternatives to the edge-passivation procedure described above, e.g. the so-called "grinding" technique. This procedure consists in lowering, by means of fine sandpaper (tipically 2000/2500), the height of the resistive strips near the coverlay. The technique involves repeated passages of the fine sandpaper on the region until the desired resistance value is reached. Once the optimal resistance is obtained, the grinded region is passivated. This procedure is less invasive than the previous one as it always has a standard transverse extension, of about 1 cm, that is equal to the width of the tool used to perform the grinding. Fig. 3.80 shows the result of a grinding procedure before the passivation. On the other hand, this procedure requires much more time as each single grinding process must be followed by a new resistance measurement so as not to risk

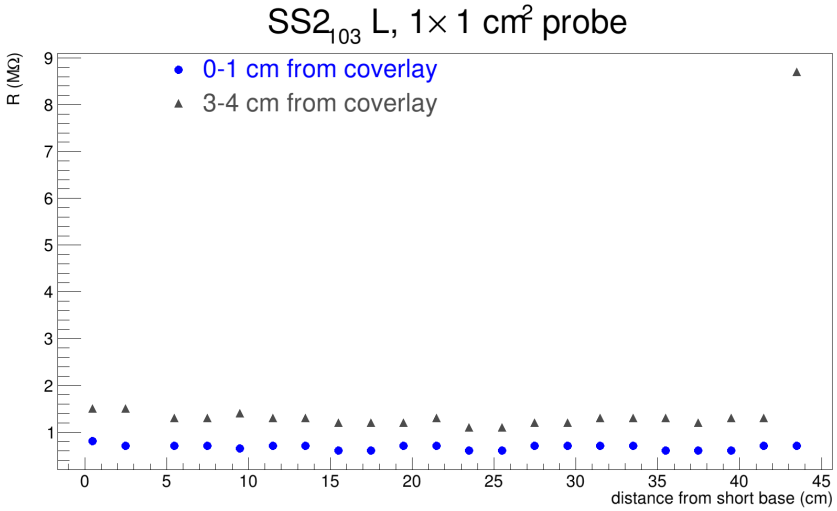

Figure 3.81: The electric resistance for a spare STEREO PCB measured by means of the 1×1 cm^2 probe.

excessively lowering the height of the strips resulting in an excessive increase in resistance. Fig. 3.82 shows the result of a grinding operation on a spare section. The resistance values were taken immediately after the region subjected to grinding before (blue dots) and after (grey triangle) the procedure, by means of a 1x1 cm^2 surface probe at steps of about 2 cm from the RO-PCB minor base. The resistance values before grinding vary between 0.6 and 0.8 MΩ, while after grinding we obtain an average value of approximately 1.7 MΩ. The negative point of the procedure, as evidenced by the 0 degree polynomial fit, is the dispersion of the resistance values after the grinding.

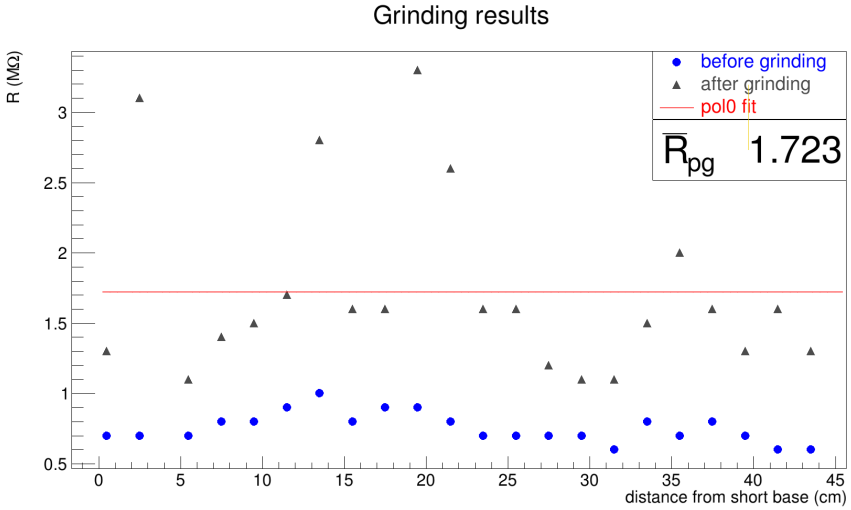

Figure 3.82: The electric resistance for a spare RO-PCB measured by means of the 1×1 cm^2 probe before (blue dots) and after (grey triangle) that the grinding technique is performed. The red line is a pol0 fit.

The behavior in HV stability is significantly better after the edge-passivation of the problematic sections, but it does not zeroed the discharge probability. In fact some sections continue to show HV stability issues. It was therefore decided to start using gas mixtures different from the standard ones. In particular Ar/CO_2/iC_4H_{10} (93:5:2) mixture seems to

give good results. The presence of iso-butane allows to obtain good gains in the amplification gap with lower electric fields, in fact the maximum anode voltage with the use of this mixture has been reduced to 500-520 V. By lowering the electric field the force that attracts the mesh towards the anode is lower and therefore the resistive layer work is more effective. In addition, the photo-absorption cross section of iso-butane is relatively high and this goes against the formation of streamers and therefore of discharges. Fig. 3.83 shows a comparison of the current stability versus time when operating with the standard gas mixture at HV_{max} = 570 V or with $Ar/CO_2/iC_4H_{10}$ (93:5:2) mixture at HV = 520 V is shown for a given HV section. A clear impact on the stability of the section is shown. Moreover no detector efficiency loss, wrt the standard gas mixture and operating voltage, is observed.

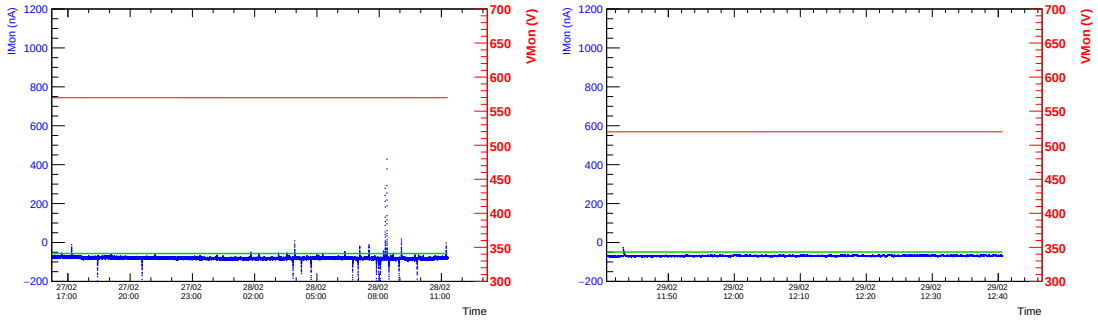

Figure 3.83: (left): I_{mon} and V_{mon} as a function of time for one section of a SM1 chamber at standard operating voltage and gas mixture. (right): the same plot for the same section, with the $Ar/CO_2/iC_4H_{10}$ (93:5:2) gas mixture at 520 V operating voltage.

Chapter 4

Global Gas Tightness Test

The presence of contaminating gases within the detector active volume reduces its efficiency and accelerates its aging process.
The MM modules, as well as almost all the gas detectors, work with gaseous mixtures placed at a pressure higher than the atmospheric one. Obviously it is not possible to create perfectly hermetic systems, that is, without gas leak sources. Such sources are the main cause not only of the dispersion of the gaseous mixture towards the outside but also of air contamination inside the active volume of the detector. In fact, despite the fact that the pressure of the gaseous mixture is higher than the atmospheric pressure the probability that air enters the detector is never zero.
In order to keep air contamination to the minimum it is necessary to minimize the detector gas leak rate and at the same time perform a continuous exchange of the gas mixture. The higher the detector gas leak rate, the greater the total changes of the gas mixture volume must be.
In the next paragraphs we will see what are the main causes related to the gas leak rate of the MM modules. Moreover the method developed at the LAE for estimating the gas leak rate of the drift panels will then be presented.

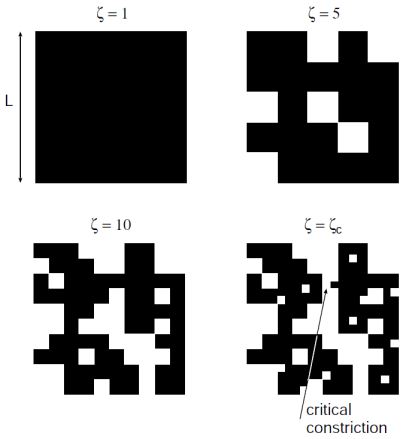

Figure 4.1

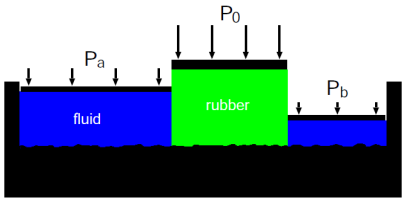

Figure 4.2

The feasible sealing level of a device depends primarly on the seal structure or on the effective contact surface between O-Ring and hard surface. The theoretical prediction of the feasible sealing level is huge sensitivity to particular variables and parameters such as the squeezing pressure P_0 and the plane elastic modulus of the O-Ring rubber E. The other crucial parameters are referred to the hard surface topographical properties, the rms roughness and the roll-off wave number which have to be determined experimentally. A theory that takes into account the parameters listed above and through which a rough estimate of the leak rate of a system can be given is that developed by Persson et al. [47]. The theory is based on studying the interface between the rubber and the hard countersurface at different magnifications ζ. At low magnification the surfaces appears flat and the contact between them appears to be complete, i.e. no leak channels can be ob-

served. However, when we increase the magnification we observe surface roughness at the interface, and, in general, non-contact regions. As the magnification increases or at short wavelenght, we will observe more and more roughness, and the apparent contact area between the solids will decrease (Fig. 4.1). At high enough magnification, for $\zeta = \zeta_c$, a non-contact percolation channel will appear, through which fluid will flow, from the high pressure side (pressure P_a) to the low pressure side (pressure P_b), Fig. 4.2.

An estimate of the leak-rate is obtained by assuming that all the leakage occurs through the critical percolation channel, and that the whole pressure drop $\Delta P = P_a - P_b$ occurs over the critical constriction. Thus for an incompressible Newtonian fluid which the fluid velocity satisfies the Navier-Stokes equation, the volume flow per unit time through the critical constriction will be

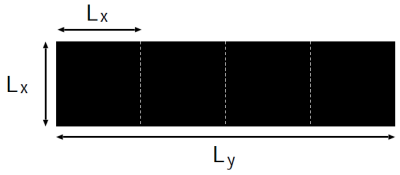

Figure 4.3

$$Q_l = \frac{L_y}{L_x}\left(\alpha \frac{{u_1}^3(\zeta_c)}{12\eta}\right)\Delta P \tag{4.1}$$

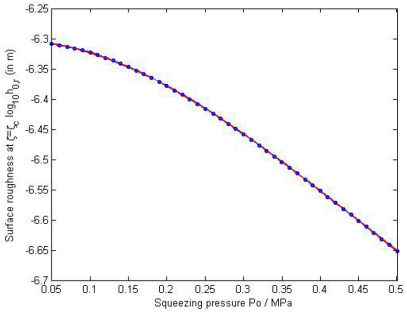

Figure 4.4

where L_x and L_y are the width and lenght of the rectangular nominal contact region between the rubber and the hard countersurface respictivley with dimension $L_x \times L_y$ (Fig. 4.3, their ratio $N = L_x/L_y$ express approximatly the number of squares area along the sealing), α is a factor which depends on the exact shape of the critical constriction, but which is expected to be of order unity, $u_1(\zeta_c)$ is the separation of the surfaces at the critical constriction and η is the dynamic fluid viscosity. The interfacial separation at critical constriction $u_1(\zeta_c)$ can be approximated to the root mean square roughness $h_{rms}(\zeta_c)$. In fact, the difference between these two quantities as the squeezing pressure varies, is very small.

Eq. 4.1 was used by Alexoupolus et al. [14] in order to determine the minimum gas sealing level for the MM modules. Obviously for such systems, which work at an overpressure of just 3 mbar, it is legitimate to consider the dynamics of the fluid in the percolation channels as incompressible (Mach number $<<$ 0.3) and consider their flow as a laminar flow (Reynolds number $<$ 1000). Their analisys was mainly aimed to determining the L_x and u_1 parameters for the particular case.

The L_x is calculated based on the Hertz theory of elastic contacts. They estimate that the effective contact strip width is given by

$$L_x = \frac{0.3 \times 4P_0R}{E^*} = \frac{1.2P_0R}{E^*} = \frac{1.2P_0R(1-\nu^2)}{E} \tag{4.2}$$

where the factor 0.3 is based on empirical knowledge that the maximum pressure is applied only mainly in the centre over a region approximately of order of 0.3 of the width of the effective contact strip, R is the O-Ring radius, E^* the plane elastic modulus, E and ν the viscoelastic modulus and the Poisson ratio of the O-Ring respectively.

The roughness of the hard surfaces of the system, FR4 and Kapton, was measured using the Atomic Force Microscope (AFM). From the analysis of the results it emerged that the roughness of the Kapton surface is much lower than that of the FR4 therefore it contributes very little to estimating the gas leak rate. Fig. 4.4 shows the logarithm in basis ten of the roughness $h_{0,r}(\zeta_c)$ ($h_{0,r}(\zeta_c) \equiv h_{rms}(\zeta_c)$) at the critical magnification ζ_c as a function of the squeezing pressure P_0.

4.1 The MM Quadruplet GTT

Developing a measurement method for determining the gas leak rate of MM modules turns out to be a very difficult task. Let's try to get an idea of the factors that contribute to the complexity of the measure. The geometric volume of the modules is not rigid. In fact, despite the presence of the interconnections, the external walls of the detector tend to swell towards the outside when the internal pressure increases. This implies a dependence of the overpressure inside the detector on the atmospheric pressure. The temperature variations affect the pressure inside the detector. If these two factors are not taken into account, the measurement of the gas leak rate can be overestimated or underestimated. The sealing system of the MM modules is extremely sensitive and this greatly affects the repeatability of the measurement:

- The O-Rings have a length of several meters, it is therefore difficult to identify any defects on its surface.
- The O-Rings elastomer do not have a uniform density (it is produced through extrusion process) and this affects its elastic modulus.
- The elastomer elastic modulus depends on ambient temperature.
- The FR4 and Kapton contact surfaces are, as we saw in the subsection on "Polishing", subjected to processes which, even if slightly, alter their average roughness.
- The gas gap frame is fixed to DP by screws without using glue. Consequently it is possible that over time it will move from its design position by relaxing the O-Ring.

The gas tightness of the MM quadruplet is tested twice before mounting them in the NSW. The first test is performed at the quadruplet assembly laboratory, while the second and last test is performed at the building 899 (BB5) at Cern. As for the MM SM1 quadruplets, these are tested inside the clean room (CR2) at the Gran Sasso shed of the LNF using the pressure drop method without taking into account the elasticity of the quadruplet walls and the temperature variations effect on the gas volume. The last test, to which all MM quadruplets are subjected (SM1, SM2, LM1, LM2) is not performed inside a clean room and uses the Flow Rate Loss method with constant pressure. In this case the quadruplet is connected to the gas mixture line and the gas leak rate is determined by the difference between the inlet and outlet flow from the volume through the use of two mass flow sensors (Omron® D6F-P0001A1). Also this method to date does not take into account the temperature and atmospheric pressure variations effect on the gas leak rate. Moreover it bases its measurement on a mass flow-meter which are obviously sensitive to the mass of the gas passing through them and therefore also sensitive to contaminant molecules (O_2, H_2O, ...) trapped on the active volume surfaces and which are torn from them by the passage of the gaseous mixture.

4.2 SM1 DP Global GTT

The SM1 DP global GTT, completely conceived and developed at the LAE, is based on the pressure drop method used in the case of rigid volumes and contains the corrections to systematic errors induced by atmospheric pressure and temperature variations on the gas leak rate estimation. It can be used in all cases where the vessel containing the gas is susceptible to elastic deformations.
In the next sections some results obtained from tests conducted on a rigid volume with and without calibrated loss will be shown first. From this analysis we learned how to extend the corrections in atmospheric pressure from the case of rigid volume to the case of elastic volume and what is the sensitivity of the method adopted. The stand used for the global GTT and the methodology used to estimate the air leak rate related to the deformable volume will then be described. Furthermore, we will compare the measurement of the air leak rate linked to the calibrated loss in the case of the deformable volume with that linked to the non-deformable volume. Finally, the results of the tests conducted on a DP set will be presented.

4.2.1 Air Leak Rate in a Rigid Volume

The rigid volume used for our tests is a stainless steel cylindrical vessel with a capacity of 8 l. The differential pressure sensor is connected to the vessel internal volume by means of a propylene pipe. The temperature sensor is placed in close contact with the vessel and to reduce the effects that changes in room temperature have on the pressure inside the vessel, the latter has been closed in a wooden box together with the temperature and differential pressure sensor (Fig. 4.5). The barometric sensor is placed outside of the wooden box but near it. The sensors and the ADC are of the same type as those described in Appendix A.

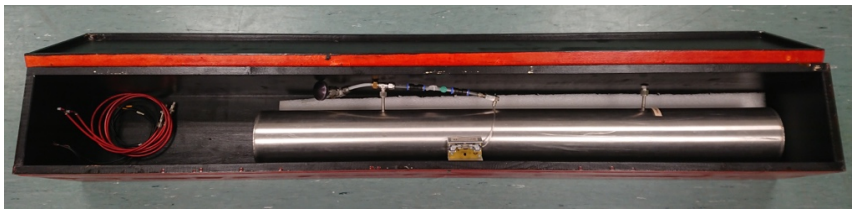

Figure 4.5: The stainless steel cylindrical vessel complete with differential sensor pressure and temperature sensor in the wooden box.

To obtain the overpressure inside the rigid volume we insert a small quantity of air by mean of a syringe, about 30 ml. In the case of a rigid volume there are no volume deformations but only an increase in internal volume pressure.
Five long tests (lasting a few days) were carried out on the vessel and obviously the trend over time of overpressure, temperature and atmospheric pressure were recorded.
First let's see what are the corrections in atmospheric pressure to be made to our measurement. We measure the overpressure Δp using a differential pressure sensor, so the absolute pressure inside the volume p_{abs} is equal to

$$p_{abs} = P_{atm} + \Delta p$$

If we consider the equation of perfect gases for two different p_{abs} values and leave the number of moles and temperature unchanged we can write

$$\begin{aligned} p^0_{abs} V &= nRT \\ p^1_{abs} V &= nRT \end{aligned} \tag{4.3}$$

from this we can simply deduce

$$P^0_{atm} + \Delta p^0 = P^1_{atm} + \Delta p^1 \implies \Delta p^0 = P^1_{atm} - P^0_{atm} + \Delta p^1 \tag{4.4}$$

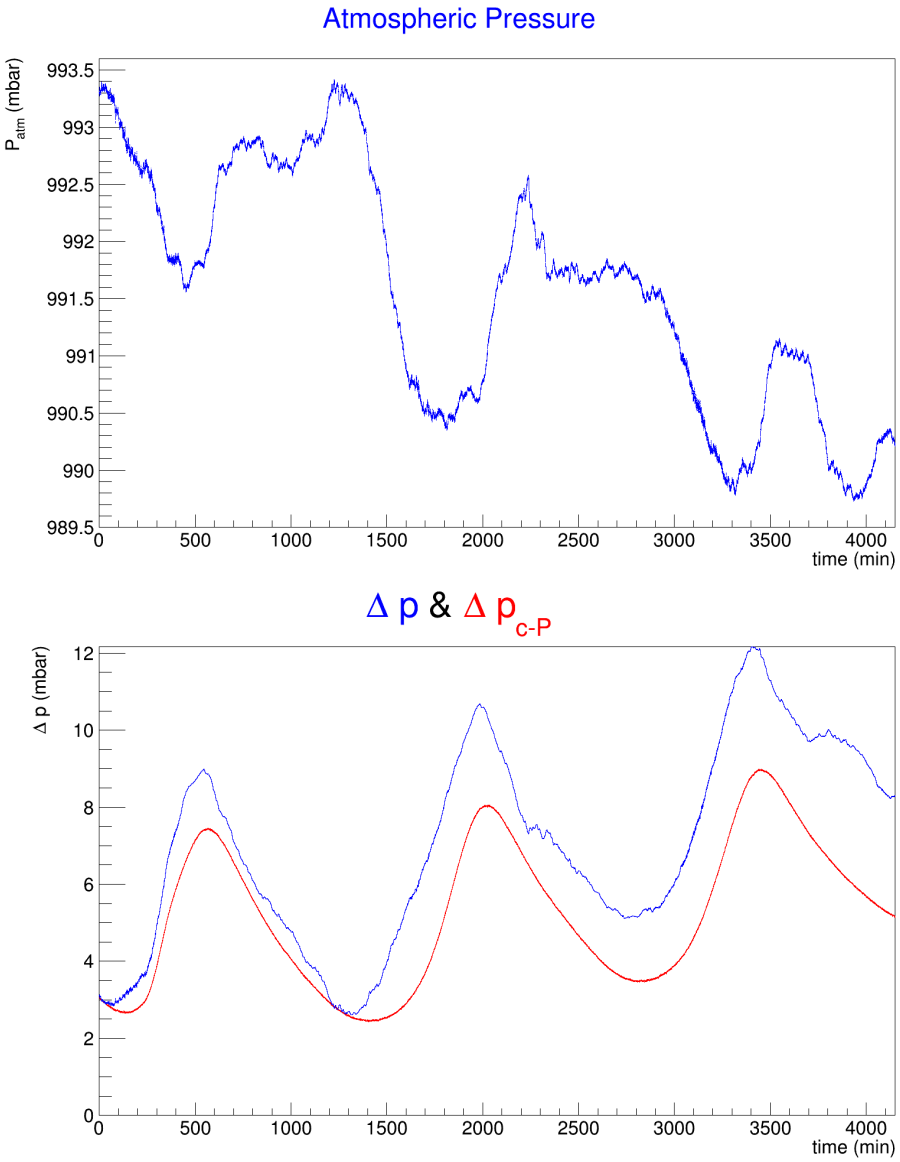

Figure 4.6: Atmospheric pressure and overpressure trend over time in the case of the rigid volume for the test number 4.

Fig. 4.6 shows the trend over time of the atmospheric pressure (top) and overpressure Δp (center) inside the vessel for the we will call test number 1. We pushed in the rigid volume 0.03 l of air by means of a syringe obtaining a maximum overpressure of about 3.5 mbar.

The overpressure varied in anticorrelation with the atmospheric pressure. Full periods of about 20 hours are also evident. The overpressure graph shows both the overpressure not corrected for atmospheric pressure (in blue) and the correct one Δ p_{c-P} (in red) using the equation 4.4 or

$$\Delta p_{c-P}(t) = P_{atm}(t) - P_{atm}(0) + \Delta p(t) \tag{4.5}$$

where $P_{atm}(0)$ is the initial atmospheric pressure.
Now let's move on to determine the corrections in temperature. Fig. 4.7 shows the superimposition between the overpressure inside the volume and the temperature trends over time. The first thing that is observed is a delay between the temperature changes and the overpressure changes (Fig. 4.7, top).

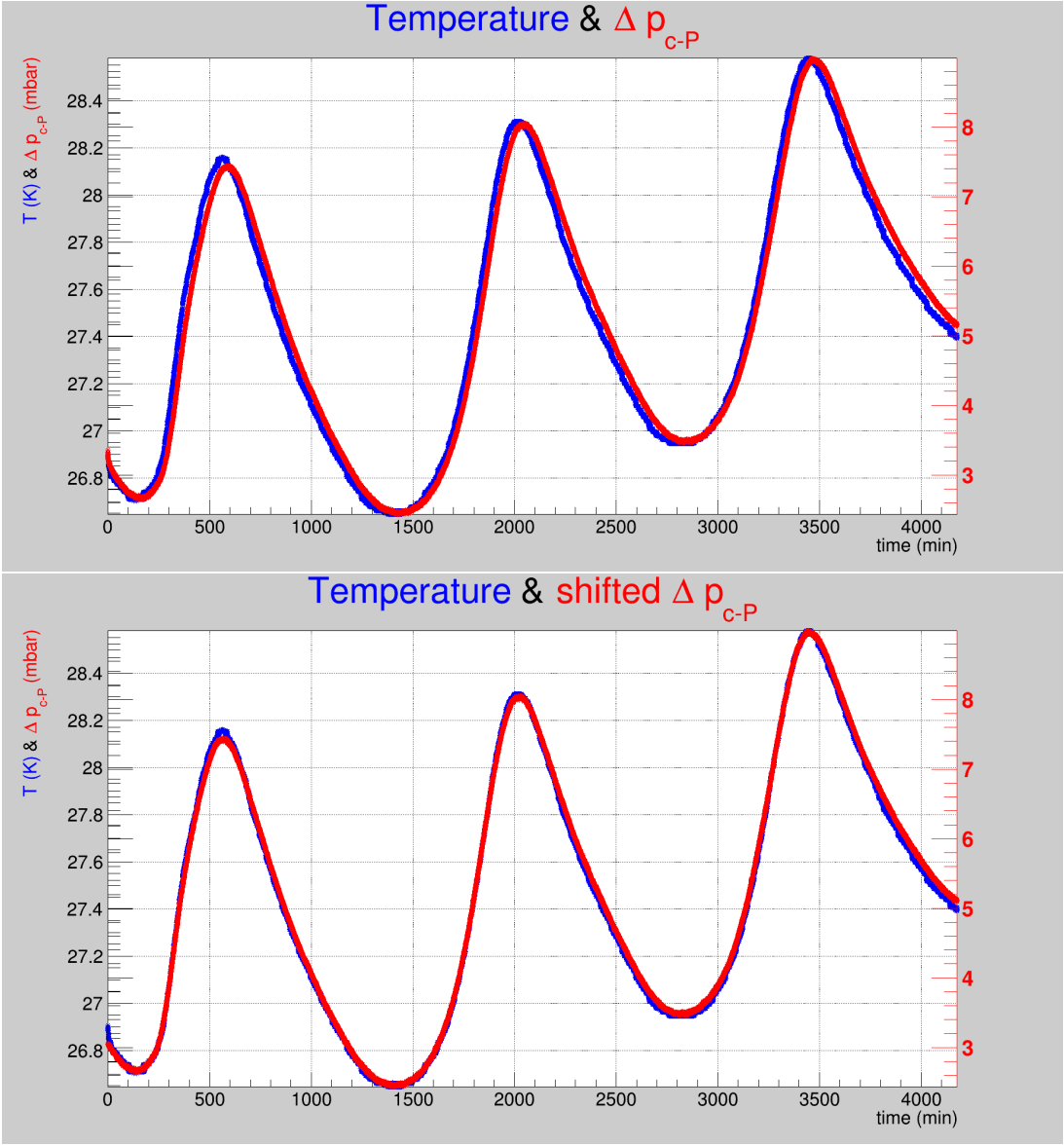

Figure 4.7: The graphs show the overlap of the temperature (blue) and overpressure (red) trend over time for the test number 1. At the top, a phase shift between the two curves is evident which is reduced to zero with a temporal translation of the overpressure of about 22.5 minutes (bottom).

Obviously the volume inside the vessel takes a certain time to see the changes in temperature outside it, i.e. the heat meets a certain impedance represented by the stainless steel walls of the vessel. It is therefore necessary, before applying the temperature correction, to perform a time shift on the overpressure values in order to align them with the temperature values. An overpressure values time shift of about 22.5 minutes (time $\rightarrow$ 0) leads to a perfect overlap between the two curves (Fig. 4.7, bottom). Obviously the last 22.5 minutes of data taking will be lost. The Fig. 4.8 instead shows the temperature and overpressure (after the time shift) correlation before (left) and after (right) the correction for atmospheric pressure. In the case of the correct one we obtain, as expected, a perfect linear correlation between the two quantities.

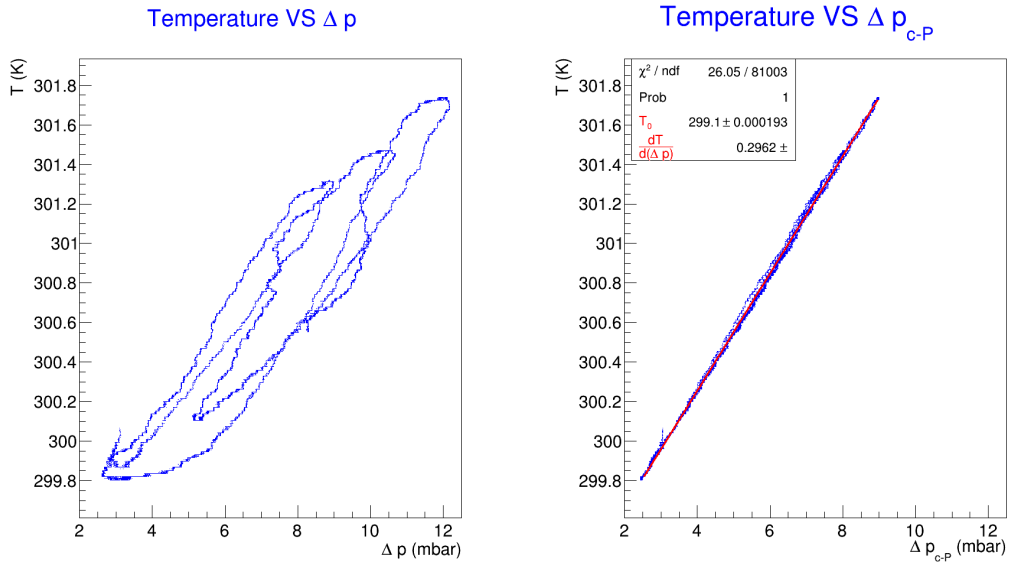

Figure 4.8: The temperature and overpressure correlation before (left) and after (right) the correction for atmospheric pressure in the case of the rigid volume. We can exploit the functional relationship between temperature and overpressure to make ourselves independent from the temperature sensor.

From the linear fit of the latter we obtain

$$T(K) \;=\; 0.2962\ \Delta p_{c-P} \;+\; 299.1 \tag{4.6}$$

The slope equal to 0.296 K/mbar is in excellent agreement with the ratio $\frac{V}{n_0 R}$, deriving from the equation of ideal gases, where n_0 is the number of initial moles at temperature T = 303.1 K and atmospheric pressure P_{atm} = 993.4 mbar contained in the rigid volume. Assuming that the rigid volume overpressure changes only due to a change in temperature, from ideal gas equation, we can write

$$\begin{aligned} (P^0_{atm} \;+\; \Delta p^0)V \;&=\; nRT^0 \\ (P^0_{atm} \;+\; \Delta p^1)V \;&=\; nRT^1 \end{aligned} \tag{4.7}$$

From term to term ratio we obtain

$$\Delta p^0 \;=\; (P^0_{atm} \;+\; \Delta p^1)\frac{T^0}{T^1} \;-\; P^0_{atm} \tag{4.8}$$

hermetic stainless steel cylindrical vessel					
n. test	$\frac{d\Delta p}{dt}(mbar/min)$	Δp^0 (mbar)	P^0_{atm} (mbar)	Q_l (l/min)	Q_l (l/min) @ 3 mbar
2	$-4.2 \cdot 10^{-4}$	4.2	989.5	$-3.4 \cdot 10^{-6}$	$-2.4 \cdot 10^{-6}$
3	$-5.4 \cdot 10^{-5}$	5.1	993.7	$-4.4 \cdot 10^{-7}$	$-2.5 \cdot 10^{-7}$
4	$-1.1 \cdot 10^{-5}$	3.6	988.3	$-8.6 \cdot 10^{-8}$	$-7.3 \cdot 10^{-8}$
5	$-4.2 \cdot 10^{-7}$	4.4	990.2	$-3.4 \cdot 10^{-9}$	$-2.3 \cdot 10^{-9}$

Table 4.1: Air leak rate tests results for the hermetic stainless steel vessel.

As before, generalizing for all instants time of data taking and obviously exploiting the already corrected overpressure Δp_{c-P} for atmospheric pressure we have

$$\Delta p_{c-P,T}(t) \;=\; (P_{atm}(0) \;+\; \Delta p_{c-P}(t))\frac{T(0)}{T(t)} \;-\; P_{atm}(0) \tag{4.9}$$

Moreover, given the almost perfect correlation between temperature and overpressure rigid volume, we can express the term T(t) as a function of $\Delta p_{c-P}(t)$ using the relation 4.6 and making us independent of the temperature sensor whose resolution is limited.
The Fig. 4.9 shows the trend of temperature (top) and the overpressure (bottom) Δp_{c-P} with (red) and without (green) the temperature correction. The linear fit of the overpressure $\Delta p_{c-P,T}$ corrected also for temperature has a slope close to zero. It is in good agreement with the expected results of a hermetic vessel.
Under the same experimental conditions, another 4 air tightness measurements of the hermetic rigid vessel were carried out and the results are shown in the table 4.1. The table shows the pressure drop over time equivalent to the Q_l (mbar/min); the initial overpressure Δp^0 resulting from the linear fit of data taking; the atmospheric pressure value P^0_{atm} recorded at the start of the test; the equivalent Q_l (l/min) and the Q_l (l/min) related to the overpressure of 3 mbar. The average air leak rate of this system and its uncertainty (RMS) amount to $(-6.74 \pm 11.5)\cdot 10^{-7}$ l/min at 3 mbar overpressure. The RMS obtained represents the air leak rate resolution of the exposed measurement method which is about 65 times smaller than the ATLAS gas leak rate tolerance imposed for the SM1 DPs.
To verify that the described method is capable of reconstructing a defined air leak, a medical hypodermic 32G needle with 0.24 mm diameter is used as a calibrated leak. It is inserted in the polyethylene pipe that connects the needle valve to the differential pressure sensor, as shown in Fig. 4.10. Five tests were performed using the calibrated leak and making the corrections in atmospheric pressure and in temperature introduced previously to the data taken. It should be noted that the presence of the hole does not allow us to be able to exploit the relation 4.6 to extrapolate the temperature trend over time from the overpressure. In fact, in this case the overpressure also depends on the loss of air and not only on the temperature. In this case we used the temperature values obtained from the sensor.

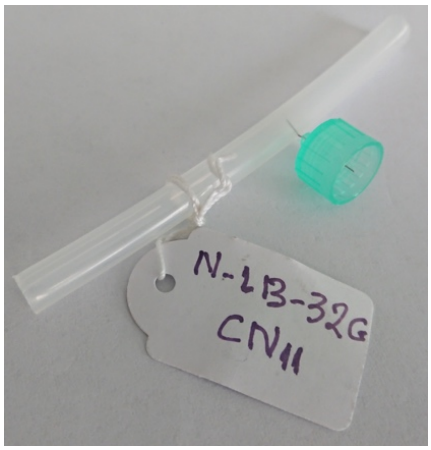

Figure 4.10

The Fig. 4.11 shows the raw overpressure values (in blue), those corrected for atmospheric pressure (in red) and those corrected also for temperature (in green) for the test number

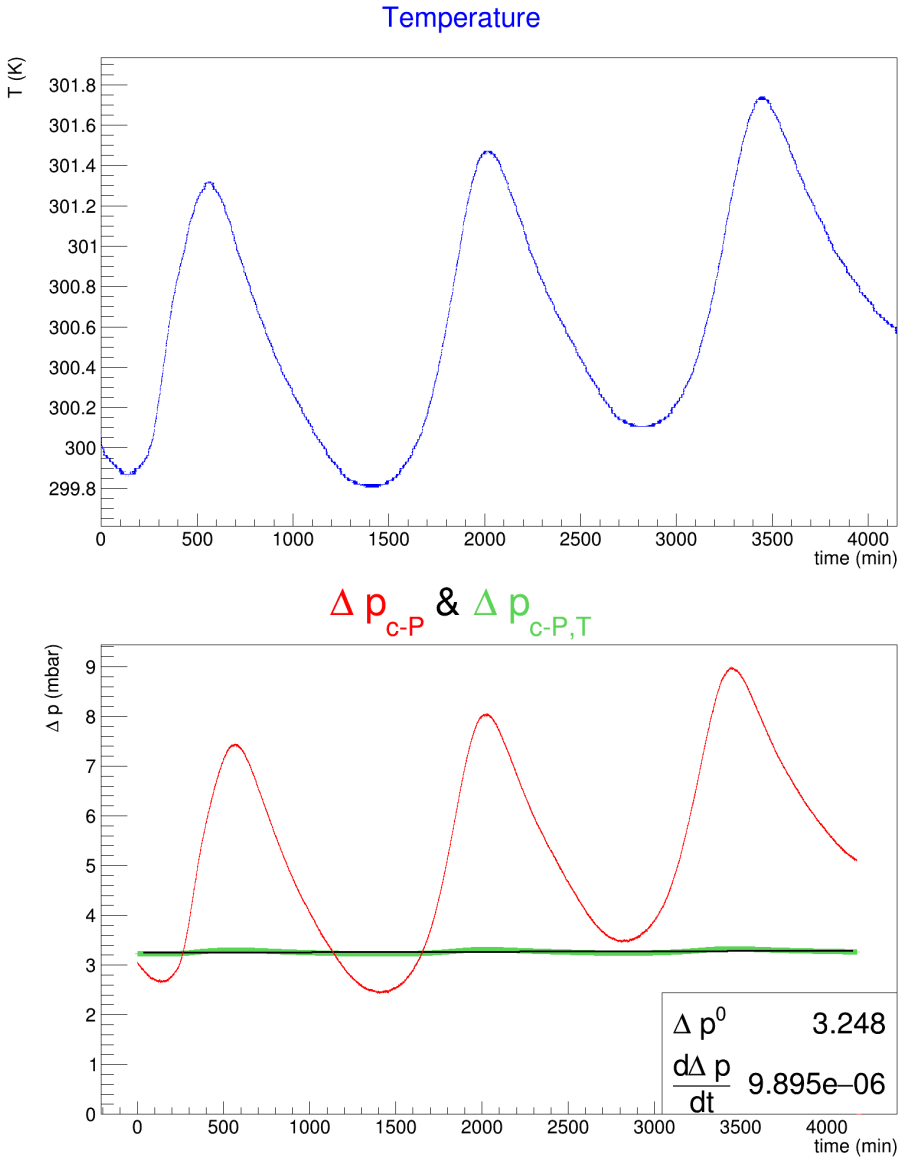

Figure 4.9: Temperature (top) and overpressure (bottom) trend over time for the rigid volume. The overpressure graph show the overpressure inside the volume corrected for atmospheric pressure (red) and overpressure corrected for atmospheric pressure and temperature (green). The linear fit (black line) give us a slope close to zero demonstrating the good air tightness of the rigid vessel.

2. An exponential fit ($e^{(C\,+\,\lambda t)}$) was performed on the latter in order to determine the calibrated air leak rate Q_l. In particular we have

$$Q_l \;=\; \frac{d}{dt}(e^{(C\,+\,\lambda t)})|_{t=0} \;=\; C\lambda \tag{4.10}$$

The same procedure was also carried out in the case of the other tests. The results are shown in the table 4.2
where $\Delta p^0 \;=\; e^C$. The air leak rate of the stainless steel vessel with 32G needle is then the average value of these 5 measurements: $Q_l^{RV} \;=\; (-6.5 \;\pm\; 2.8) \cdot 10^{-5}$ l/min, where the uncertainty is the RMS of these 5 measurements.

stainless steel cylindrical vessel with calibrated leak						
n. test	$\lambda(min^{-1})$	Δp^0 (mbar)	Q_l (mbar/min)	P^0_{atm} (mbar)	Q_l (l/min)	Q_l (l/min) @ 3 mbar
1	$-2.3 \cdot 10^{-3}$	4.1	991.7	$-9.5 \cdot 10^{-3}$	$-7.7 \cdot 10^{-5}$	$-5.6 \cdot 10^{-5}$
2	$-2.7 \cdot 10^{-3}$	4.2	993.0	$-1.2 \cdot 10^{-2}$	$-9.3 \cdot 10^{-5}$	$-6.6 \cdot 10^{-5}$
3	$-4.0 \cdot 10^{-3}$	4.4	991.7	$-1.8 \cdot 10^{-2}$	$-1.4 \cdot 10^{-7}$	$-9.7 \cdot 10^{-5}$
4	$-3.4 \cdot 10^{-3}$	3.3	988.3	$-1.1 \cdot 10^{-2}$	$-9.1 \cdot 10^{-5}$	$-8.2 \cdot 10^{-5}$
5	$-9.5 \cdot 10^{-4}$	3.8	991.4	$-3.6 \cdot 10^{-3}$	$-2.9 \cdot 10^{-5}$	$-2.3 \cdot 10^{-5}$

Table 4.2: Air leak rate tests results for the stainless steel vessel with the calibrated leak.

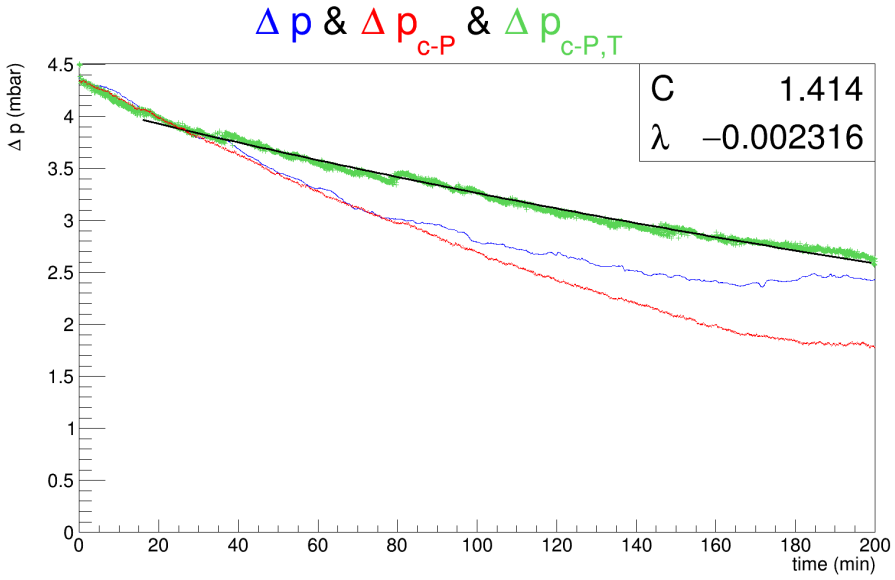

Figure 4.11: The overpressure trend over time for test number 2. In blue the raw overpressure data; in red the overpressure corrected for atmospheric pressure and in green the overpressure corrected for atmospheric pressure and temperature. From the exponential fit (black line) we can extrapolate the air leak rate of the vessel generated by the calibrated leak.

4.2.2 Global GTT Stand

To perform the DP global GTT the DP is paired with dummy panels to form a closed vessel with the gas gaps equal to the real ones. For the ODPs, only one dummy panel (d-TOP) is used. Instead, two are used for the central one (d-BOT and d-TOP). The dummy panels have been designed to have a 1 cm thick aluminum honeycomb sandwiched between two full 1 mm thick aluminum sheets with polished surfaces. A 40 × 10 mm aluminum bar is inserted inside the panel along its height. They result much stiffer than drift ones. The d-TOP is instrumented with a temperature and differential pressure sensors. In particular, the temperature sensor is inserted in the panel to be in direct contact with the gas inside the gap. Fig. 4.12 shows the two dummy panels. While Fig. 4.13 shows the detail of the panel internal face with the temperature sensor (top) and the hole (bottom) that connect the gas gap to the differential pressure sensor. Both dummy panels are completed with mesh-frame and gas gap-frame to house the O-Ring. Also in the case of dummy panels the mesh frame is fixed with screws and glue, while the gas gap frame is fixed only with screws. Three over four DP gas distribution holes were plugged with Kapton tape to make them airtight. Only one DP gas distribution hole is left open in order to plug the gas insert directly connected to it to a valve. The ODP paired with the d-TOP or the sandwich d-BOT/CDP/d-TOP is enclosed into an aluminum profile exoskeleton and put on the trapezoidal table (Fig. 4.14a). The exoskeleton is formed by 12 aluminum profiles connected in pairs through screws passing through the DP assembling holes. To gaurantee a uniform distribution of the O-Ring squeezing pressure 45 spring clamps (each with a clamping force of about 100 N) are placed along the entire O-Ring groove length. Experience has taught us that it takes several hours for the sealing system to stabilize or the O-Ring takes several hours to squeeze to the optimal point imposed by the O-Ring groove. To generate an overpressure of just over 3 mbar it is sufficient to insert 100 ml of air into the gas gap, both in the case of the ODPs and in the case of the CDPs. The air is inserted by means of a syringe with a capacity of 100 ml through the gas distribution hole of the panel that has remained open (Fig. 4.14b). The introduction of air into the gas gap must be done slowly so as not to subject the system to stress.

Figure 4.12

Figure 4.13

The temperature and pressure inside the gas gap together with the atmospheric pressure are monitored for no less than 2 h (by mean of the three sensors described in Appendix A). The analog signal of the sensors is converted into digital by means of the 16-bit ADC (see

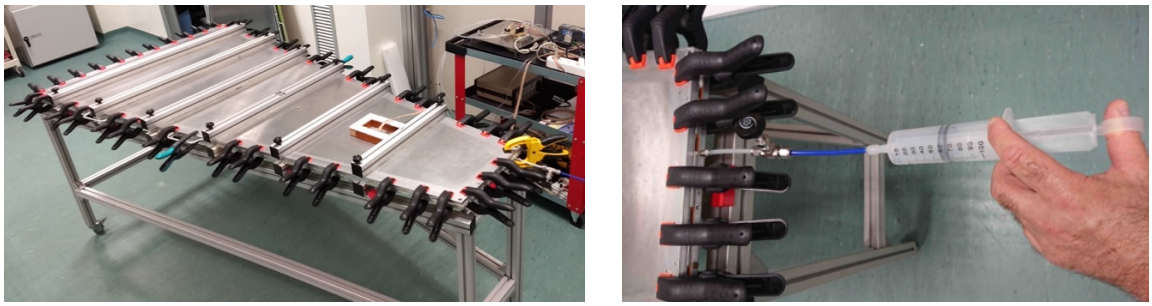

(a) (b)

Figure 4.14: (a): An outer drift panel paired with the d-TOP completed with exoskeleton and the spring clamps mounted along the entire O-Ring length. (b): To increase the pressure inside the gas gap 100 ml off air is introduced by means of a syringe. The needle valve is open when air enters the volume and closed immediately after emptying the syringe.

Appendix A)) and then sent via serial connection to the PC where a GUI developed in LabVIEW is available. It provides the graphs of the gas gap overpressure and temperature and the atmospheric pressure as a function of time and it record the data in a .txt file for their subsequent foundamental analysis. The GUI overpressure graph is needed especially at the beginning of the test. As it allows us to verify that the entire system has been correctly mounted. Indeed the presence of dirt on the O-Ring contact surfaces, a clamp loose, an element of the exoskeleton not tightened well or a gas distribution hole not well sealed can generate a rapid decrease of the overpressure inside the gas gap at the beginning of the test. In the event that a similar situation arises, the gas gap is opened, the necessary checks are carried out and then everything is reassembled.
For the entire duration of the test it is essential that the system remains isolated to avoid sudden changes in temperature and/or atmospheric pressure.
Once the global GTT is finished, the data are analyzed and in the event of a gas leak rate above specifications or in the case of sudden changes in the overpressure due to sudden changes in the experimental setup, such as the loose of an exoskeleton screw and/or a clamp, the test is repeated.
We are interested in determining the losses related only to the cathode side of the DPs, therefore the losses related to the d-TOP and/or the d-BOT must be subtracted from the total air leak rate. To determine the zero of the measurement many tests were carried out using one aluminium dummy panel at a time (d-TOP or d-BOT) coupled with a dummy Drift Panel (dDP) whose surface is formed by a single FR4 sheet without holes. The dDP has a trivial internal aluminium structure and it has not assembled using the vacuum bag technique, consequently it is less rigid than a standard DP.

4.3 Air Leak Rate in an Elastic Volume

4.3.1 Vessel Overpressure Carachterization

The SM1 DP vessel used for the global GTT do not have a rigid volume. In fact, despite the presence of the exoskeleton, the increase in pressure inside the gas gap causes the walls of the vessel to swell. For overpressures of the order of the mbar (up to 10 - 12

mbar) the vessel, both in the case of an ODP and of a CDP, deforms elastically, i.e. the relationship that exists between the overpressure inside the gas gap Δp and the volume of air inserted ΔV remains linear as in the case of non-deformable geometric volumes but with a different slope m. Fig. 4.15 shows a vessel overpressure carachterization performed on an ODP. 0.1 l of air at the pressure of 985.8 mbar and at the temperature of 299.1 K in steps of 0.02 l was inserted into the gas gap using a syringe. The corresponding overpressure was recorded at each step. The maximum overpressure reached is 3.3 mbar. The functional relationship between the two quantities can be written as follows

$$\Delta p = m\ \Delta V \tag{4.11}$$

where we have neglected the offset Δp_0. The same overpressure would have been reached, in the case of an equivalent non-deformable volume, with just under 0.03 l. This means that about 70% of the air inserted inside the gas gap does not generate an overpressure but rather inflates the vessel. The term m depends mainly on the elastic constant of the system or on the mechanical constraints of the gas gap volume.

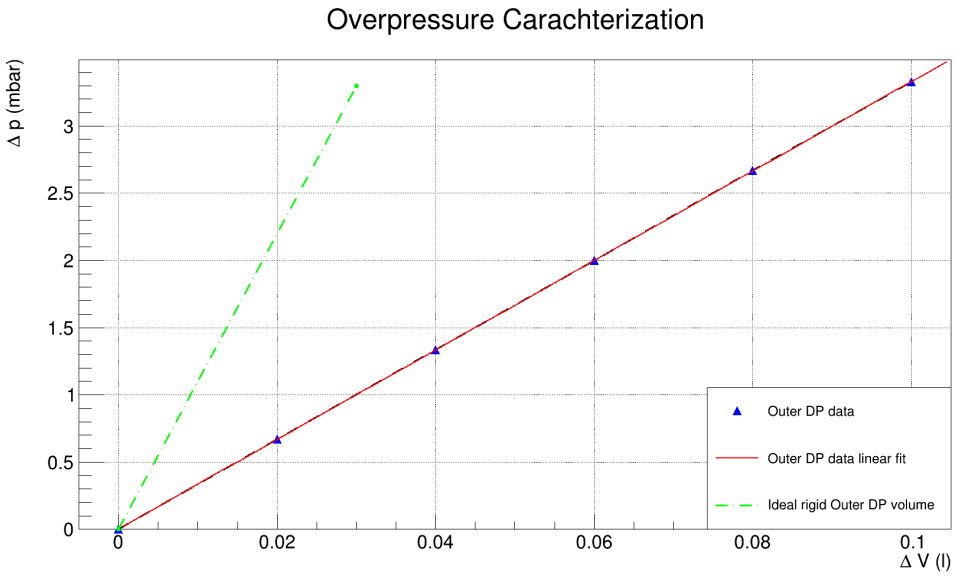

Figure 4.15: A vessel overpressure carachterization example. The blue triangles refer to our vessel carachterization data. They are fitted with a linear polynomial (red line). The elastic behavior of the vessel is evident. The green dotted line refer to an ideal rigid vessel with the same volume as the previous one (7.5 l).

The calibration takes place in a short time. We assume that during this time the atmospheric parameters do not vary and that the vessel air leak is negligible.
We start from this relation to estimate the SM1 DP gas leak rate. In fact, once a ΔV(0) = 0.1 l of air has been inserted into the gas gap and the corresponding maximum overpressure reached Δp(0) is recorded, we can use the slope $m' = \frac{1}{m} = \frac{\Delta V(0)}{\Delta p(0)}$ to determine istant by istant how the volume of air inserted varies

$$\Delta V(t) = \frac{\Delta V(0)}{\Delta p(0)}\ \Delta p(t) \tag{4.12}$$

Obviously, under ideal conditions, or in the hypothesis in which both the atmospheric pressure and the temperature remain constant during the data taking, the equation 4.12

alone would give us the possibility to determine the vessel gas leak rate. But during the global GTT both the atmospheric pressure and the temperature will vary affecting the measurement of the overpressure inside the gas gap. They represent systematic errors on the measured $\Delta p(t)$ that must be evaluated and then subtracted. Otherwise said it is necessary to make corrections that allow us to observe the evolution of the $\Delta V(t)$ as if the temperature and atmospheric pressure had not changed over time. In this way we have the possibility to determine what is the true quantity of air that has remain in the vessel and therefore what is the vessel air leak rate.

4.3.2 Atmospheric and Temperature Corrections for the SM1 DP Vessel

Let us now determine the corrections for atmospheric pressure to be made to the Δp(t) term contained in the equation 4.12. To do this, we should start from the case of a rigid volume and then generalize the relationship to the case of an elastic volume.
In the case of our vessel that has an elastic volume, a damping factor of the correction for atmospheric pressure must be introduced into the equation 4.5. In fact, the differential pressure sensor is sensitive only to changes in atmospheric pressure which affect the overpressure inside the volume. When we insert a known quantity of air inside an elastic volume, part of the inserted air inflates the volume, while another part generates the overpressure. As a consequence of the air insertion into the volume V this latter change to (V + ΔV) and pressure from P^0_{atm} to (P^0_{atm} + Δp^0). Corrections for atmospheric pressure must be applied to this last component. This component is obtained, as usual, from the law of perfect gases and expresses the percentage of the syringe volume that generates the overpressure inside the volume. This factor, which we will call α, can be extracted from the ratio between the number of moles n contained in the volume V at atmospheric pressure P^0_{atm} and temperature T^0 and the number of moles n$'$ contained in the volume V$'$ = V + Δ V at the pressure P^0_{atm} + Δ p^0 and temperature T^0

$$\frac{n}{n'} = \frac{(P^0_{atm} + \Delta p^0)(V + \Delta V)}{P^0_{atm}\, V} \Longrightarrow V + \Delta V = \frac{P^0_{atm}\, V}{P^0_{atm} + \Delta p^0}\frac{n'}{n} \tag{4.13}$$

the ratio n$'$/n can also be written in terms of the volumes of air, i.e. in terms of the volume to be tested at atmospheric pressure and the volume of air V_s at atmospheric pressure inserted inside the latter by mean of the syringe to obtain the desired overpressure

$$\frac{n'}{n} = \frac{P^0_{atm}\,(V + V_s)}{P^0_{atm}\, V} = \frac{V + V_s}{V}$$

inserting this last term in the equation 4.13 we obtain

$$\Delta V = \frac{P^0_{atm}}{P^0_{atm} + \Delta p^0}(V + V_s) - V$$

the dumping factor α is therefore equal to

$$\alpha = 1 - \Delta V$$

The α factor give a measure of the elasticity of the volume and can assume values between 0 and 1. For α equal to zero we are in the presence of a perfectly elastic volume. This

means that it is not possible to generate an overpressure within this volume. Vice-versa for α equal to 1 we are in the presence of a perfect rigid volume.

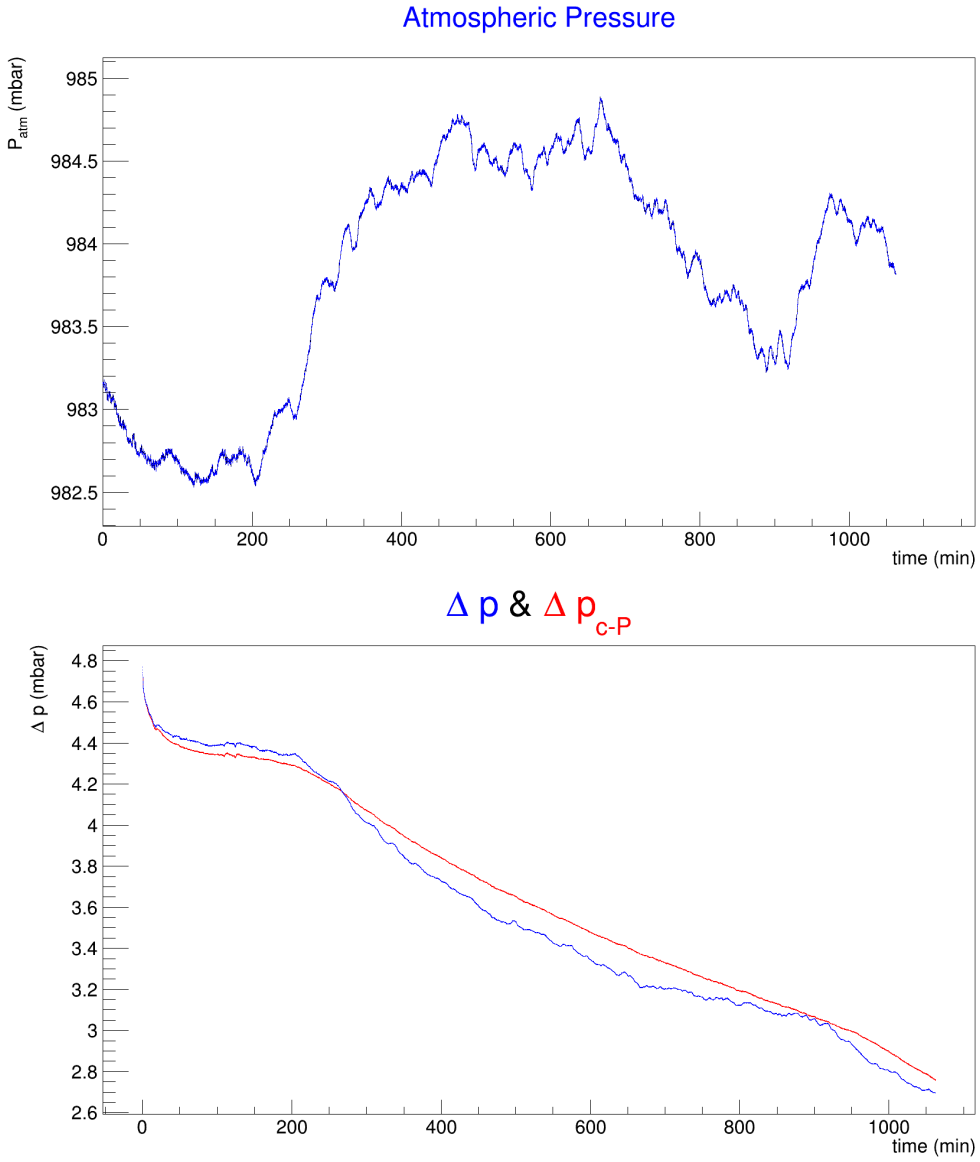

Figure 4.16: Atmospheric pressure and overpressure trend over time for the d-Top/dDP vessel.

Fig. 4.16 shows the trend over time of the atmospheric pressure (top) and overpressure Δp (bottom) inside the d-Top/dDP vessel during about 16.5 hours data taking. We pushed in the volume 0.4 l of air by means of a syringe obtaining a maximum overpressure of about 4.5 mbar. The overpressure varied according to the temperature and it is anti-correlated with the atmospheric pressure. The overpressure graph shows both the overpressure not corrected for atmospheric pressure (blue) and the correct one (red) using

$$\Delta p_{c-P}(t) \;=\; \alpha\;(P^{atm}(t) \;-\; P^{atm}(0)) + \Delta p(t) \tag{4.14}$$

The α dumping factor is equal to 0.095.
We now proceed to determine the temperature corrections to be made to the equation 4.12.

We consider n moles of air at atmospheric pressure and at different temperatures T_0 and T_1. The same number of moles will occupy a different volume at different temperatures. Let these volumes be $V_0 = V + \Delta V_0$ and $V_1 = V + \Delta V_1$. Using the perfect gases equation we can write

$$\begin{aligned} P_{atm}\ V^0 &= nRT^0 \\ P_{atm}\ V^1 &= nRT^1 \end{aligned} \tag{4.15}$$

subtracting member from member we obtain

$$V^0 = V^1 + \frac{nR}{P_{atm}}\ (T^0 - T^1)$$

The term $\frac{nR}{P_{atm}}$ can be written for our vessel as $\frac{V_v + V_s}{T_0}$ where V_v and V_s are the vessel and syringe volumes, respectivley. So we have

$$\Delta V_0 = \Delta V_1 + (V_v + V_s)\frac{T_0 - T_1}{T_0} \tag{4.16}$$

this last equation represents the temperature correction necessary to bring the volume ΔV_1 to the temperature T_0.
Putting together the equations 4.12, 4.14 and 4.16 we obtain the relation that allow us to determine the air leak rate of our vessel

$$\Delta V(t) = \frac{\Delta V(0)}{\Delta p(0)}\Delta p_{c-P}(t) + (V_v + V_s)\left(\frac{T(0) - T(t)}{T(0)}\right) \tag{4.17}$$

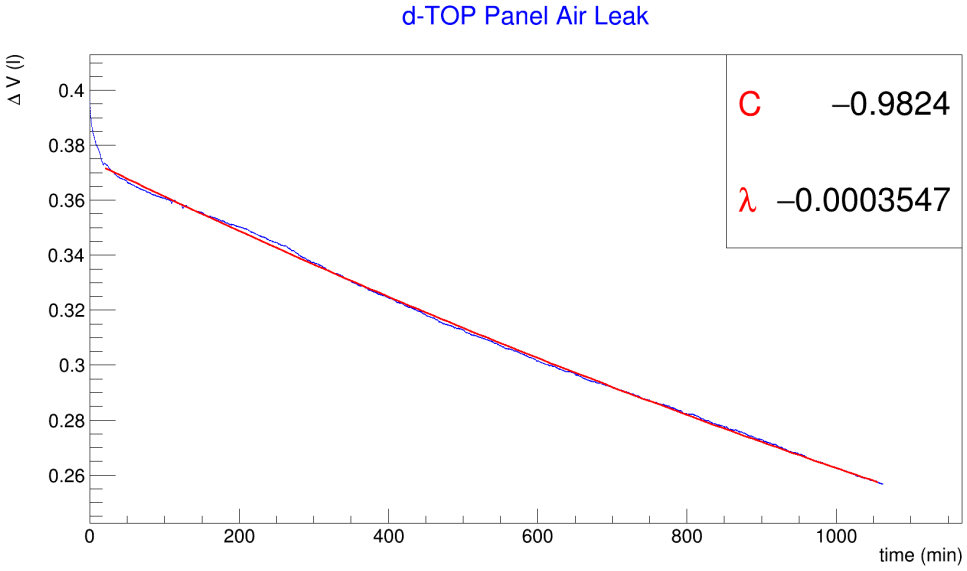

Figure 4.17: The remaining air volume ΔV(t) for the d-TOP/dDP vessel. The air leak rate is determined from the parameters C and λ extrapolated from the data exponential fit (red line).

Fig. 4.17 shows, as an example, the remaining air volume ΔV(t) of the d-TOP/dDP vessel. Data show, soon after the insertion of air into the gas gap with the syringe, a rapidly decrease lasting 15 minutes. The cause of this rapid variation is to be linked to the increase

in air temperature during the air insertion and its subsequent thermalization to the vessel walls temperature. The recorded data are well represented by an exponential function of the form $\exp(C + \lambda t)$, tending to a linear trend due to the small value of the decay constant. The air leak rate is determined as in the case of the rigid volume or $Q_l = C\lambda$. From the equation 4.17 it is possible to extract the trend of the overpressure inside the volume corrected for atmospheric pressure and temperature $\Delta p_{c-P,T}(t)$ (Fig. 4.18). In particular we have

$$\Delta p_{c-P,T}(t) = \frac{\Delta p(0)}{\Delta V(0)} \Delta V(t) \tag{4.18}$$

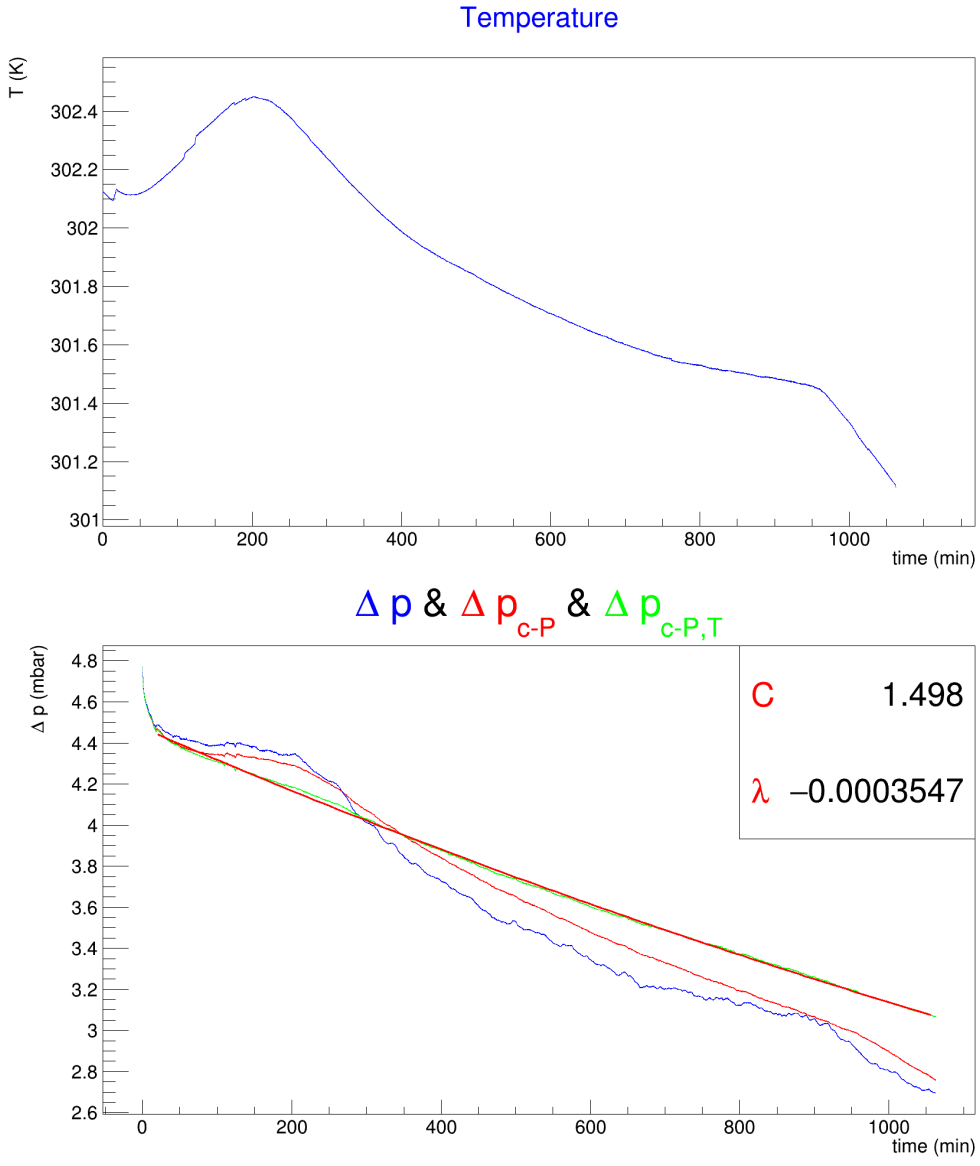

Figure 4.18: Top: temperature trend over time for the d-TOP/dDP vessel. Bottom: the overpressure inside the d-TOP/dDP vessel as a function of time. In blue the Δp raw data; in red the Δp_{c-P} data and in green the overpressure corrected for atmospheric pressure and for temperature $\Delta p_{c-P,T}$. An exponential fit (red line) is performed on the last.

4.3.3 Air Leak Rate Offset and Calibrated Leak for SM1 DP Vessel

In order to determine the zero of our measurement or the minimum leakage value for our stand, 9 air leak rate tests were performed for the vessel composed of d-BOT and dDP and 11 for the vessel composed of d-TOP and dDP through the same procedure described previously. The tables 4.3 and 4.4 show the results obtained. It reports the value of the dumping factor α, decay costant λ, the extrapolated initial overpressure $\Delta p^0 = e^C$, the air leak rate Q_l and its error and lastly the equivalent Q_l at 3 mbar overpressure.

d-BOT/dDP vessel						
n. test	α	$\lambda(min^{-1})$	Δp^0 (mbar)	Q_l (l/min)	ΔQ_l (l/min)	Q_l (l/min) @ 3 mbar
1	0.089	$-9.3 \cdot 10^{-5}$	4.2	$-3.5 \cdot 10^{-5}$	$2.1 \cdot 10^{-7}$	$-2.5 \cdot 10^{-5}$
2	0.091	$-1.1 \cdot 10^{-4}$	4.3	$-4.1 \cdot 10^{-5}$	$4.1 \cdot 10^{-8}$	$-2.8 \cdot 10^{-5}$
3	0.092	$-1.4 \cdot 10^{-4}$	4.4	$-5.2 \cdot 10^{-5}$	$1.5 \cdot 10^{-7}$	$-3.5 \cdot 10^{-5}$
4	0.092	$-5.8 \cdot 10^{-5}$	4.5	$-2.2 \cdot 10^{-5}$	$9.0 \cdot 10^{-8}$	$-1.5 \cdot 10^{-5}$
5	0.092	$-1.0 \cdot 10^{-4}$	4.3	$-3.8 \cdot 10^{-5}$	$4.3 \cdot 10^{-8}$	$-2.6 \cdot 10^{-5}$
6	0.095	$-1.4 \cdot 10^{-4}$	4.6	$-5.2 \cdot 10^{-5}$	$2.4 \cdot 10^{-8}$	$-3.4 \cdot 10^{-5}$
7	0.093	$-1.1 \cdot 10^{-4}$	4.4	$-4.0 \cdot 10^{-5}$	$1.0 \cdot 10^{-7}$	$-2.8 \cdot 10^{-5}$
8	0.095	$-1.2 \cdot 10^{-4}$	4.7	$-4.9 \cdot 10^{-5}$	$1.2 \cdot 10^{-8}$	$-3.1 \cdot 10^{-5}$
9	0.094	$-1.0 \cdot 10^{-4}$	4.6	$-4.0 \cdot 10^{-5}$	$1.1 \cdot 10^{-7}$	$-2.6 \cdot 10^{-5}$

Table 4.3: Air leak rate tests results for the d-BOT/dDP vessel.

d-TOP/dDP vessel						
n. test	α	$\lambda(min^{-1})$	Δp^0 (mbar)	Q_l (l/min)	ΔQ_l (l/min)	Q_l (l/min) @ 3 mbar
1	0.090	$-4.6 \cdot 10^{-4}$	4.2	$-1.7 \cdot 10^{-4}$	$4.9 \cdot 10^{-8}$	$-1.2 \cdot 10^{-4}$
2	0.093	$-6.9 \cdot 10^{-4}$	4.4	$-2.6 \cdot 10^{-4}$	$1.7 \cdot 10^{-7}$	$-1.8 \cdot 10^{-4}$
3	0.096	$-6.2 \cdot 10^{-4}$	4.4	$-2.3 \cdot 10^{-4}$	$7.5 \cdot 10^{-8}$	$-1.6 \cdot 10^{-4}$
4	0.096	$-4.9 \cdot 10^{-4}$	4.7	$-1.8 \cdot 10^{-4}$	$2.9 \cdot 10^{-8}$	$-1.2 \cdot 10^{-4}$
5	0.095	$-3.6 \cdot 10^{-4}$	4.5	$-1.3 \cdot 10^{-4}$	$1.9 \cdot 10^{-8}$	$-8.9 \cdot 10^{-5}$
6	0.096	$-4.7 \cdot 10^{-4}$	4.4	$-1.7 \cdot 10^{-4}$	$1.7 \cdot 10^{-7}$	$-1.2 \cdot 10^{-4}$
7	0.099	$-5.3 \cdot 10^{-4}$	4.8	$-2.1 \cdot 10^{-4}$	$1.9 \cdot 10^{-7}$	$-1.3 \cdot 10^{-4}$
8	0.098	$-4.9 \cdot 10^{-4}$	4.6	$-1.8 \cdot 10^{-4}$	$1.2 \cdot 10^{-7}$	$-1.1 \cdot 10^{-4}$
9	0.099	$-4.2 \cdot 10^{-4}$	4.6	$-1.6 \cdot 10^{-4}$	$7.1 \cdot 10^{-8}$	$-1.0 \cdot 10^{-4}$
10	0.096	$-5.2 \cdot 10^{-4}$	4.4	$-1.9 \cdot 10^{-4}$	$1.3 \cdot 10^{-7}$	$-1.3 \cdot 10^{-4}$
11	0.096	$-4.6 \cdot 10^{-4}$	4.5	$-1.7 \cdot 10^{-4}$	$6.4 \cdot 10^{-8}$	$-1.1 \cdot 10^{-4}$

Table 4.4: Air leak rate tests results for the d-BOT/dDP vessel.

From the results obtained it can be observed that the damping factor α assumes values between 0.09 and 0.1, which means that about 90% of the 0.4 l of air inserted inside the vessel both in case d-TOP/dDP and in case d-BOT/dDP only inflates the vessel walls. From the average values of the air leak rate obtained for the two vessels that are $Q_l^{d-BOT} = (-2.8 \pm 0.6) \cdot 10^{-5}$ l/min and $Q_l^{d-TOP} = (-1.3 \pm 0.2) \cdot 10^{-4}$ l/min at 3 mbar overpressure, where for the statistical error the RMS is used, it can be seen that the d-TOP/dDP has a greater loss than the other, probably due to a badly positioned mesh frame angular insert on the d-TOP panel or a defect, not visible to the naked eye, present on the surface of the d-TOP in contact with the O-oring. We assume that our zero or the

minimum detectable air leak rate value for our test stand is equal to $Q_l^{d-BOT} \equiv Q_l^0$. Several tests were also conducted using the same calibrated loss (32G needle) used in the case of the rigid volume, both for the d-BOT/dDP and for the d-TOP/dDP. The tables 4.5 and 4.6 show the results obtained.

d-TOP/dDP vessel with 32G calibrated leak						
n. test	α	$\lambda(min^{-1})$	Δp^0 (mbar)	Q_l (l/min)	ΔQ_l (l/min)	Q_l (l/min) @ 3 mbar
1	0.096	$-4.5 \cdot 10^{-4}$	4.7	$-1.8 \cdot 10^{-4}$	$3.6 \cdot 10^{-8}$	$-1.1 \cdot 10^{-4}$
2	0.093	$-5.0 \cdot 10^{-4}$	4.5	$-1.9 \cdot 10^{-4}$	$1.5 \cdot 10^{-7}$	$-1.3 \cdot 10^{-4}$
3	0.095	$-5.1 \cdot 10^{-4}$	4.6	$-1.9 \cdot 10^{-4}$	$1.3 \cdot 10^{-7}$	$-1.3 \cdot 10^{-4}$
4	0.095	$-4.3 \cdot 10^{-4}$	4.6	$-1.7 \cdot 10^{-4}$	$5.5 \cdot 10^{-8}$	$-1.1 \cdot 10^{-4}$
5	0.094	$-5.9 \cdot 10^{-4}$	4.5	$-2.2 \cdot 10^{-4}$	$2.2 \cdot 10^{-7}$	$-1.5 \cdot 10^{-4}$
6	0.093	$-5.3 \cdot 10^{-4}$	4.5	$-2.0 \cdot 10^{-4}$	$1.4 \cdot 10^{-7}$	$-1.4 \cdot 10^{-4}$

Table 4.5: Air leak rate tests results for the d-BOT/dDP vessel with 32G calibrated leak.

d-TOP/dDP vessel with 32G calibrated leak						
n. test	α	$\lambda(min^{-1})$	Δp^0 (mbar)	Q_l (l/min)	ΔQ_l (l/min)	Q_l (l/min) @ 3 mbar
1	0.093	$-4.7 \cdot 10^{-4}$	4.4	$-1.8 \cdot 10^{-4}$	$5.9 \cdot 10^{-8}$	$-1.2 \cdot 10^{-4}$
2	0.092	$-6.3 \cdot 10^{-4}$	4.3	$-2.4 \cdot 10^{-4}$	$2.0 \cdot 10^{-7}$	$-1.6 \cdot 10^{-4}$
3	0.091	$-5.0 \cdot 10^{-4}$	4.3	$-1.9 \cdot 10^{-4}$	$4.8 \cdot 10^{-8}$	$-1.3 \cdot 10^{-4}$
4	0.093	$-4.3 \cdot 10^{-4}$	4.4	$-1.6 \cdot 10^{-4}$	$4.4 \cdot 10^{-8}$	$-1.1 \cdot 10^{-4}$
5	0.095	$-6.6 \cdot 10^{-4}$	4.5	$-2.5 \cdot 10^{-4}$	$2.3 \cdot 10^{-7}$	$-1.7 \cdot 10^{-4}$
6	0.092	$-6.3 \cdot 10^{-4}$	4.5	$-2.4 \cdot 10^{-4}$	$1.3 \cdot 10^{-7}$	$-1.6 \cdot 10^{-4}$
7	0.092	$-5.0 \cdot 10^{-4}$	4.4	$-1.9 \cdot 10^{-4}$	$7.4 \cdot 10^{-8}$	$-1.3 \cdot 10^{-4}$
8	0.093	$-6.2 \cdot 10^{-4}$	4.4	$-2.4 \cdot 10^{-4}$	$2.1 \cdot 10^{-7}$	$-1.6 \cdot 10^{-4}$
9	0.093	$-6.3 \cdot 10^{-4}$	4.5	$-2.4 \cdot 10^{-4}$	$7.7 \cdot 10^{-8}$	$-1.6 \cdot 10^{-4}$
10	0.095	$-5.0 \cdot 10^{-4}$	4.3	$-1.9 \cdot 10^{-4}$	$6.2 \cdot 10^{-8}$	$-1.3 \cdot 10^{-4}$
11	0.096	$-4.6 \cdot 10^{-4}$	4.5	$-1.7 \cdot 10^{-4}$	$6.4 \cdot 10^{-8}$	$-1.1 \cdot 10^{-4}$

Table 4.6: Air leak rate tests results for the d-TOP/dDP vessel with 32G calibrated leak.

The mean values and the statistical errors associated with the air leak measurements at 3 mbar overpressure are $Q_l^{d-BOT32G} = (1.3 \pm 0.1) \cdot 10^{-4}$ l/min and $Q_l^{d-TOP32G} = (1.4 \pm 0.2) \cdot 10^{-4}$ l/min.
Comparing these results with those obtained previously in the case of the vessels without calibrated leakage, a net increase in the air leak rate is observed. Thus we can say that the developed method is sensitive to the additional loss generated by the 32G needle. We can also compare, by means of the Fisher test, the variance of the measurements relating to the vessels with calibrated leak with the variance of the sum between Q_l^{d-BOT} or Q_l^{d-TOP} and Q_l^{RV}. Obviously, having only 5 measurements available in the case of the rigid volume with calibrated leak in the sum only the first five measurements for the vessels without calibrated leak will be consider. So we have $Q_l^b = Q_{l,5}^{d-BOT} + Q_l^{RV} \simeq (-9.1 \pm 2.9) \cdot 10^{-5}$ l/min and $Q_l^t = Q_{l,5}^{d-TOP} + Q_l^{RV} \simeq (-19.8 \pm 4.2) \cdot 10^{-5}$.
For the d-BOT/dDP vessel the calculated test statistic F_b is equal to $F_b = (\sigma_l^b)^2/(\sigma_l^{b32g})^2 = 3.7$ to be compared with the critical value F_c for 4/5 degrees of freedom for $\alpha/2 = 0.025$ area that is equal to 7.39. For the d-TOP/dDP vessel the calculated test statistic F_t is equal to $F_t = (\sigma_l^t)^2/(\sigma_l^{t32g})^2 = 4.0$ to be compared with the critical value F_c for 4/9 degrees of freedom for $\alpha/2 = 0.025$ area that is equal to 4.72. In both cases the calculated value

of the statistic is lower than the critical value. This allows us to accept the null hypothesis, i.e. we can say that the samples come from populations with equal variances.
We can compare the results obtained with the theoretical one predicted by equation 4.1, using equation 4.2. Assuming the following parameters for our system

- squeezing pressure $P_0 = 0.32$ MPa;
- Oring cord radius $R = 3.5$ mm;
- Oring Poisson ratio $\nu = 0.493$;
- Oring elastic modulus $E = 0.675$ MPa;
- Oring total lenght $L_y = 5.96$ m;
- the factor $\alpha = 1$;
- the root mean square roughness $h_{rms} = 3.5 \cdot 10^{-7}$ m;
- the dynamic viscoelastic air modulus at 20°C $\eta = 1.81 \cdot 10^{-}5$ Pa s;
- the in-out pressure difference $\Delta P = 300$ Pa.

we obtain an $L_x = 1.51 \cdot 10^{-3}$ m and a $Q_L \simeq 2.34 \cdot 10^{-10}$ $m^3/s \equiv 1.4 \cdot 10^{-5}$ l/min. The order of magnitude is the same as in the case of the d-BOT and close to that of the d-TOP.

4.3.4 SM1 DPs Global GTT Results

Fig. 4.19 and Fig. 4.20 show the air leak rate of a DP set (53 ODPs and 26 CDPs) as measured with the described pressure drop method. All these measurements have been converted to the overpressure of 3 mbar, using the correction factor $3/\Delta p(0)$. The difference between Q_l^0 and Q_l^{d-TOP} was subtracted from the result obtained. The most part of them shows leak rate close to the minimum detectable ($2.76 \cdot 10^{-5}$ l/min). Only a few have leak rate above the limit. The main reason of these over-threshold values is related to the corrections for atmospheric pressure and temperature, the effect of which was added only after the test. In fact, without the corrections the leak rate was in the specification.

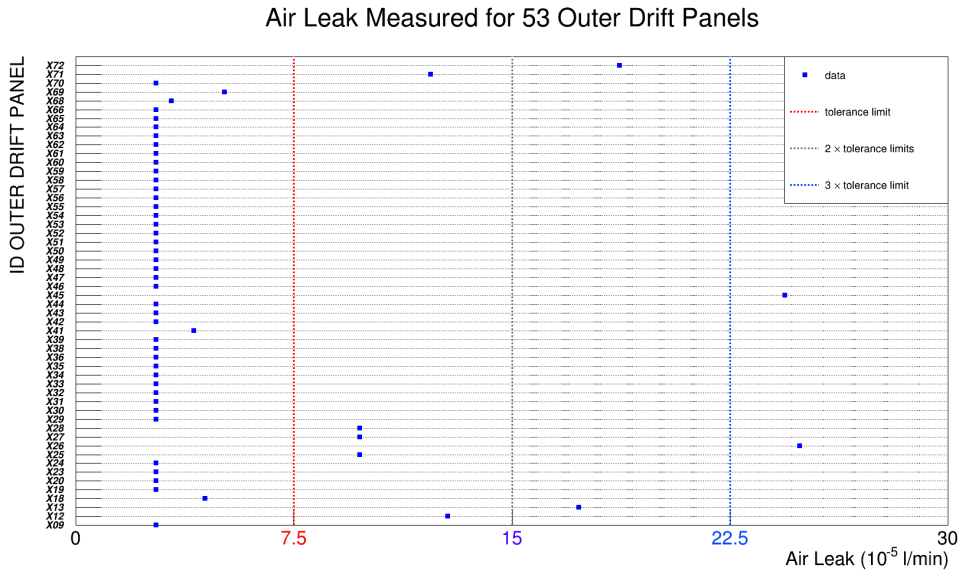

Figure 4.19: Air leak rate converted to 3 mbar overpressure of 53 tested ODPs.

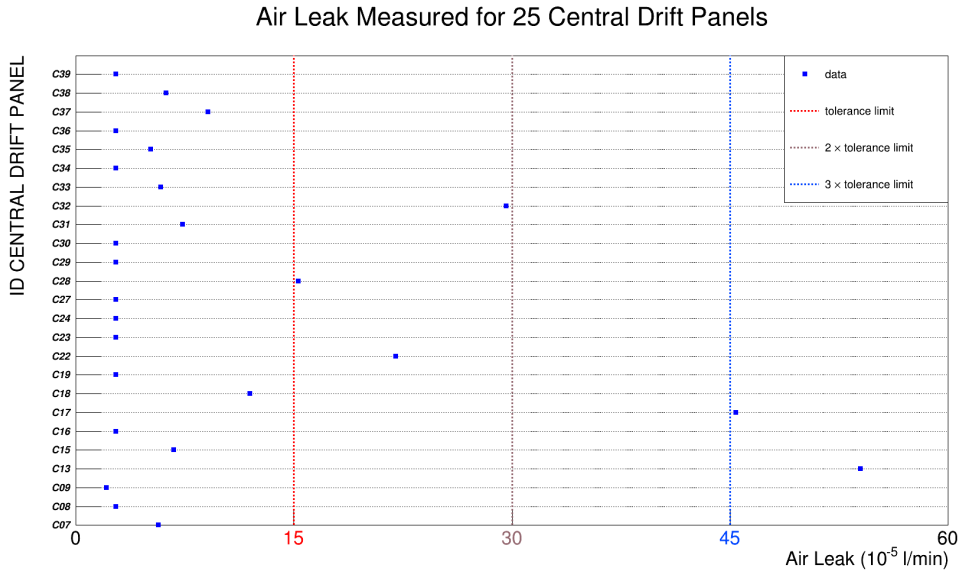

Figure 4.20: Air leak rate converted to 3 mbar overpressure of 25 tested CDPs.

Chapter 5

Cosmic Background Studies with Muon Spectrometer System

Background sources inside the ATLAS detector are several. A background signal can be triggered in coincidence with a proton bunches collision by merging with signals from the IP. Therefore it is of fundamental importance to be able to recognize and discriminate such background events. We will refer to these events by the name of Non Collision Background (NCB).
We can distinguish three main sources of NCB: inelastic hits of protons with residual gas molecules upstream, and in the vicinity of the detector, producing showers of secondary particles; protons with high transverse amplitude, lost before reaching the IP, hitting the tertiary collimators and producing background leaking in the detector; cosmic muons travelling downwards from the IP, or energy deposits in the calorimeters, inducing fake jets. Therefore, although cosmic muons are used extensively in the, e.g., chamber calibration or alignement phases, they become annoying during normal p-p collisions, especially when looking for very rare events, or minimum bias events.

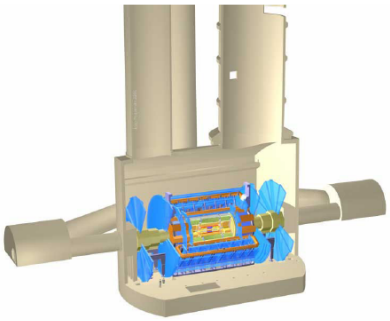

Figure 5.1

In this chapter we will describe the topological and timing differences between muon tracks arising from cosmic muon and from p-p collision in the MS RPC chambers using the CosmicCalo 2016 and the Main streams respectivley. We will therefore show how it is possible to discriminate cosmic muons from those deriving from p-p collisions using only the RPCs timing information.

5.1 Cosmic Muons in ATLAS

Cosmic muons come mainly from the decay of secondary charged pions and kaons originating from primary cosmic rays. The most important decay channels and respective branching ratios are

$$\pi^{\pm} \rightarrow \mu^{\pm} + \nu_{\mu} \quad (\simeq 100\%)$$
$$K^{\pm} \rightarrow \mu^{\pm} + \nu_{\mu} \quad (\simeq 63\%)$$

in which the produced muons take on the average 79% and 52% of the energy of the pion and kaon, respectively. The contribution of K decays to muon production is a function of the energy and ranges from 5% at low energies to an asymptotic value of 27% for E $>$ 1 TeV. At very high energies a small contribution arises from charmed particles [50].
In the Earth's atmosphere, the typical muon production height is approximately 15 km. The energy loss for muons is about 2 MeV per g/cm^2. The interaction depth of the atmosphere is about 1000 cm^2, so muons lose about 2 GeV in passing through the 15 km atmosphere. A muon only requires an energy above 2 GeV for its decay length to be longer than its production height. The cosmic muons flux and energy depends on several factors: altitude, longitude, latitude, atmosheric pressure and temperature, the time of the year,... As a first approximation it can be stated that most cosmic muons that reach the Earth's surface have a momentum between 1 and 10 GeV, and that the flux of more energetic cosmic muons decreases as their energy increases following the Gaisser parameterization [36].
The ATLAS detector is shielded from most of the lower energy cosmic muons because it is almost 100 m underground. However, the two main access shafts 5.1 (12 and 18 m diameter placed on top of the ATLAS detector as Fig. 5.1 shows) to the ATLAS cavern allow for a higher integrated intensity of muons to reach the detector than the areas where there is only solid rock above it. The cosmic muon flux for muons with transverse momenta above 20 GeV at almost 100 m underground is measured to be constant, i.e. 1 s^{-1}m^{-2} [40]. This value is of the same order of magnitude as the approximated flux of cosmic muons with energies above 20 GeV at sea level at an angle of 75° from the zenith.

5.2 Run 2 RPC Trigger Coverage

The Run 2 data taking session considered in the following started in June 2015 and lasted until November 2018. Several runs have been collected with different beam intensities, integrated luminosity, and event rate. Each run is divided in several Luminosity Blocks (LB) of about 60 seconds of length that can be considered having stable conditions in terms of detector, beam, and luminosity.
Events were selected using several different trigger criteria which were based on the presence of a muon candidate, a high-p$_T$ hadronic jet, or significant missing transverse momentum. The majority of the selected events come from the Drell–Yan production of W and Z bosons decaying into a muon and neutrino or into a muon pair, respectively. A smaller fraction of events are due to production of top quark pairs, electroweak vector-boson pairs and decays of hadrons containing bottom or charm quarks. Selected events were recorded in a dedicated data stream, i.e. the Main stream. This data includes the reconstructed muon candidates, the L1Muon trigger information and the full information related to muon detector system, including all hits recorded by the RPC detector in the 200 ns window centred on the selected bunch crossing.
Figg. 5.2a and 5.2b show the RPC coverage in the ϕ-η plane for mu and single jet trigger respectivley. The Figg. 5.2c and 5.2d instead show the distribution of the same hits in the x-y plane. A good uniformity of the hits is evident, demonstrating a good coverage of the barrel L1Muon trigger system. In particular, in Run 2, the acceptance of the RPC system has been increased by equipping with RPC four new muon stations installed in holes of the acceptance of Run 1 in the sector between the ATLAS supports or feet, i.e. the ϕ sector 13. These stations are referred as BME and BOE and they belong logically to the middle layer and outer layer of muon chambers respectively, although they are physically

at a different radius with respect to the other chambers of the corresponding layer. In addition, in ϕ sectors 12 and 14 or in corrispondence of the ATLAS feet the outer muon stations consist of two RPC chambers instead of one like in the other 14 sectors.

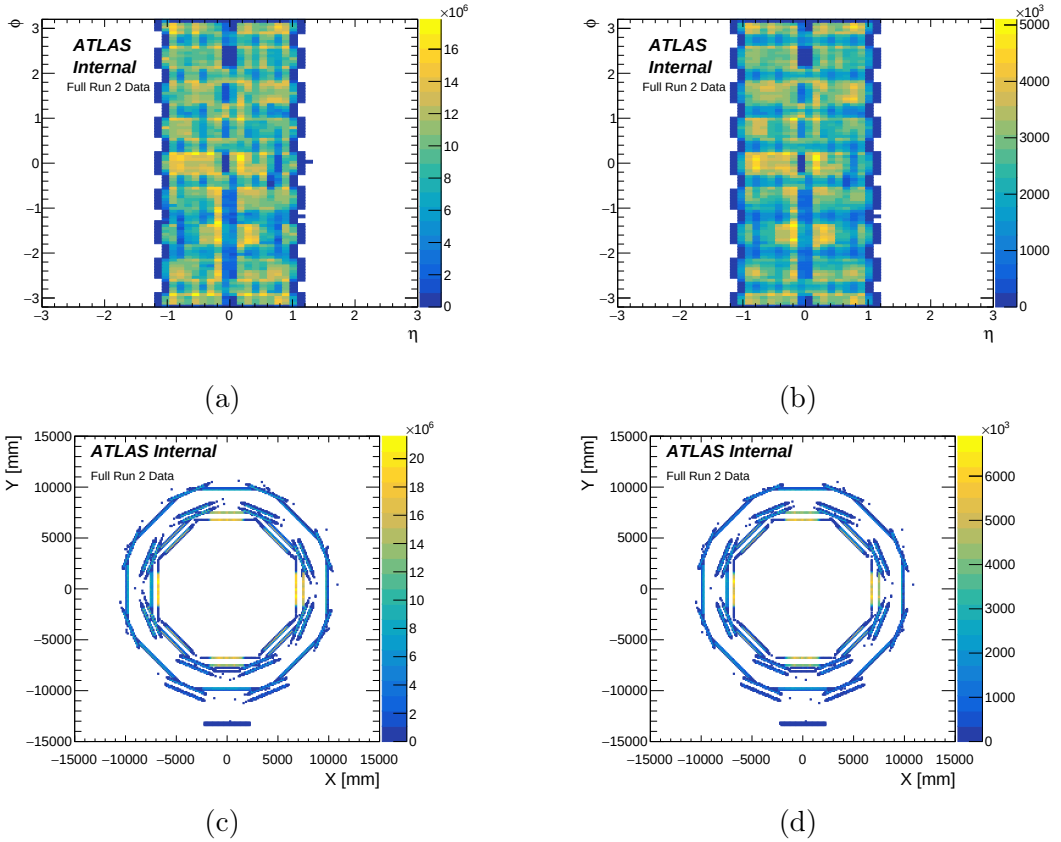

Figure 5.2: (a) and (b): distribution of RPC hits shown in terms of the η and ϕ coordinates for mu and single jet triggers respectivley. (c) and (d): the same distributions seen in the x-y plane where the RPC chambers of sectors 12, 13 and 14 inserted for Run 2 are well visible.

5.3 Run 2 RPC time

Muons from p–p collisions come from the IP region to the outer part of the detector. The timing requirements of the trigger algorithms are calibrated for muons from collisions [23], so RPC hit times are corrected taking into account the Time-of-Flight (ToF) of particles as originated from the IP: then for each muon from p-p collisions, a time equal to zero is recorded for each layer. Consequently the timing differences between two layers are expected to be 0. Figg. 5.3a and 5.3b show the RPC system time distribution for mu and single jet trigger respectivley. The zero time of the time axis corresponds to the arrival time of an ultra-relativistic particle produced at the IP in the bunch crossing selected by the trigger system. The zero-centered distribution covers a time interval corresponding to the 25 ns time window between two consecutive bunches. The distribution is divided into 8 clearly distinguishable bins of about 3.125 ns amplitude, or equal to the 320 MHz RPC clock (see Fig. 5.3c). The small humps on the sides of the central distribution that are spaced by 25 ns from each other refer to previous and subsequent bunches. The low

frequency of these distributions illustrates the typically good performance of the RPC time calibration for assigning muon hits to the correct bunch crossing.

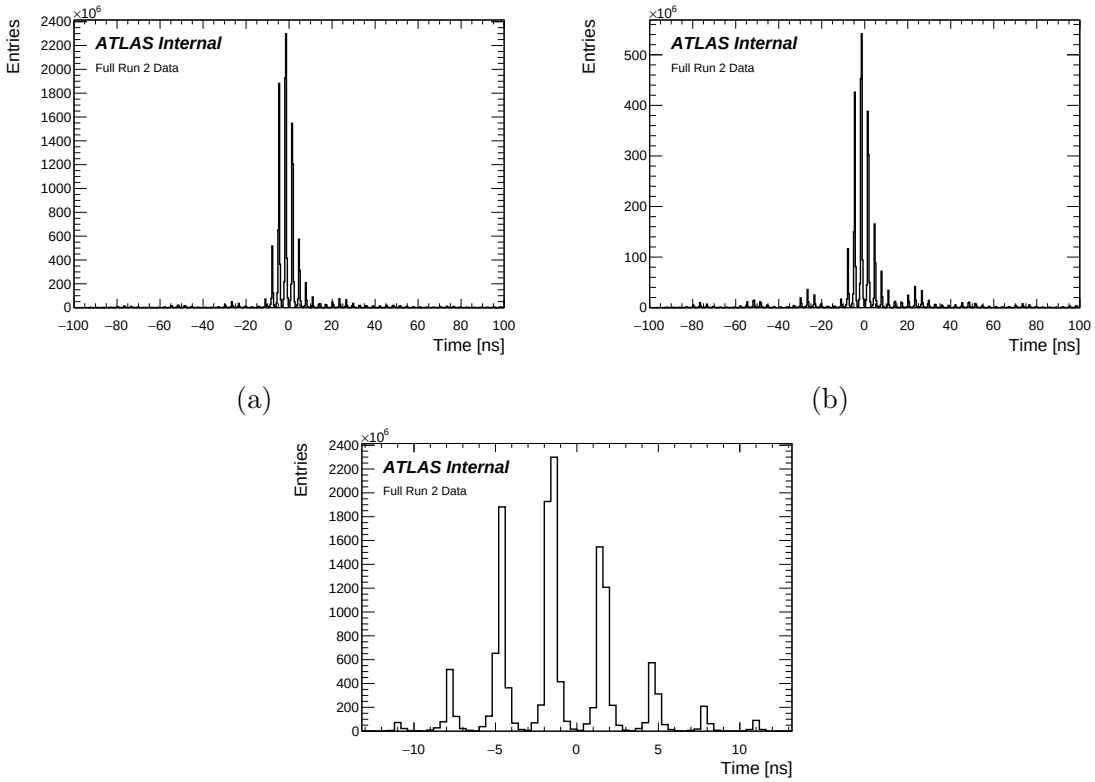

Figure 5.3: RPC time distribution for mu (a) and single jet (b) triggers. The time is centered to zero as expected. (c): the zero centred distribution where is clearly visible the RPC clock.

We define three layers within the RPC system so as to subdivide the RPC hits based on their distance from the beam, i.e. R_{hit} in cylindrical coordinates. Basically we consider all the hits coming from the high-p_T, pivot and low-p_T without requiring any conditions on the transverse momenta:

- layer 1: $R_{hit} > 9000$ mm. It corresponds to the BOL and BOS RPC hits;
- layer 2: $R_{hit} > 7750$ mm. It corresponds to the BML hits;
- layer 3: $R_{hit} < 7750$ mm. It corresponds to the BMS hits.

Fig. 5.4 shows the hits recorded by the three layers in the case of p-p collisions in the top and bottom ATLAS hemisphere, i.e. for $\phi > 0$ and $\phi < 0$. Obviously the distributions are all zero-centered.
Figg. 5.5a and 5.5b instead show the distribution of the differences in time Δt between the layer 3 and layer 2 or 1 for top and bottom hemisphere respectivley.

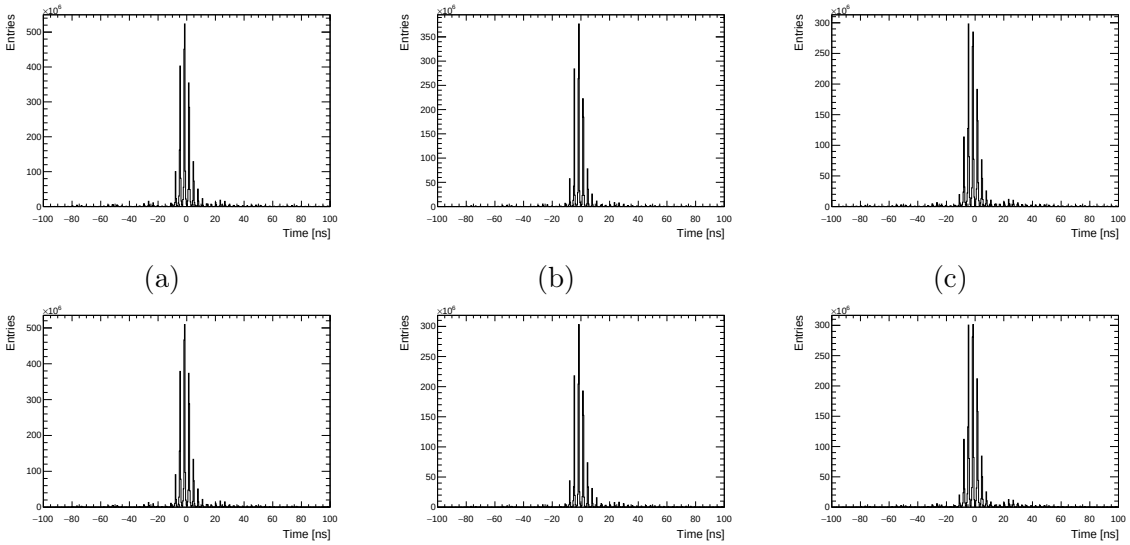

Figure 5.4: (a),(b),(c): RPC time distribution in the top hemisphere for layer 1, 2 and 3 respectivley in the mu trigger case. (c),(d),(e): RPC time distribution in the bottom hemisphere for layer 1, 2 and 3 respectivley in the mu trigger case.

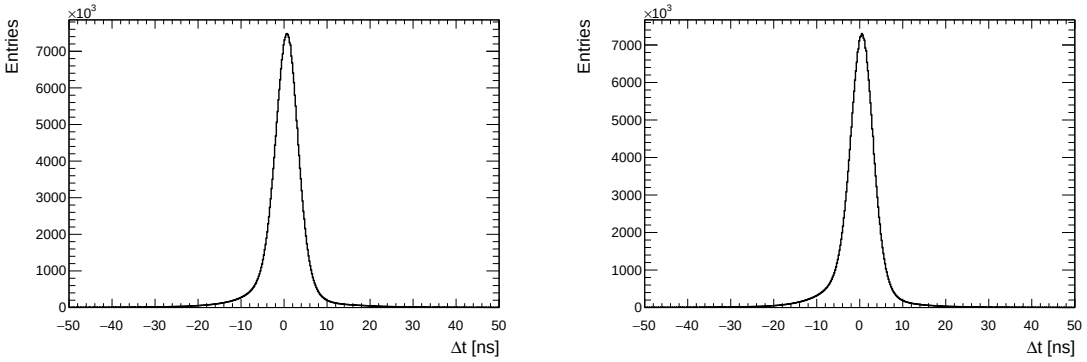

Figure 5.5: Δt distribution for the top and bottom ATLAS hemisphere.

5.4 Cosmic Muons in the RPC System

The study on cosmic rays background uses the CosmicCalo 2016 stream with empty bunches. Also in this case the mu and single jet triggers are considered. Fig. 5.6 shows the distribution of hits generated by cosmic muons in the RPC trigger system. The distributions in the x-y and y-z planes are shown for both mu and single jet triggers.
Clearly the distributions turn out to be very different wrt the case of p-p collisions. The RPC chambers are mainly hitted in the sectors at $\phi = \pm\pi/2$, as expected, that is, by muons crossing the ATLAS shafts.
The L1 trigger system in ATLAS is designed and calibrated for muons from collisions but cosmic muons will still cause the triggers to fire. In general, the muon triggers for the empty bunches work exactly the same way as the muon triggers for the filled bunches. The timing requirements of the trigger algorithms are also calibrated for muons from collisions

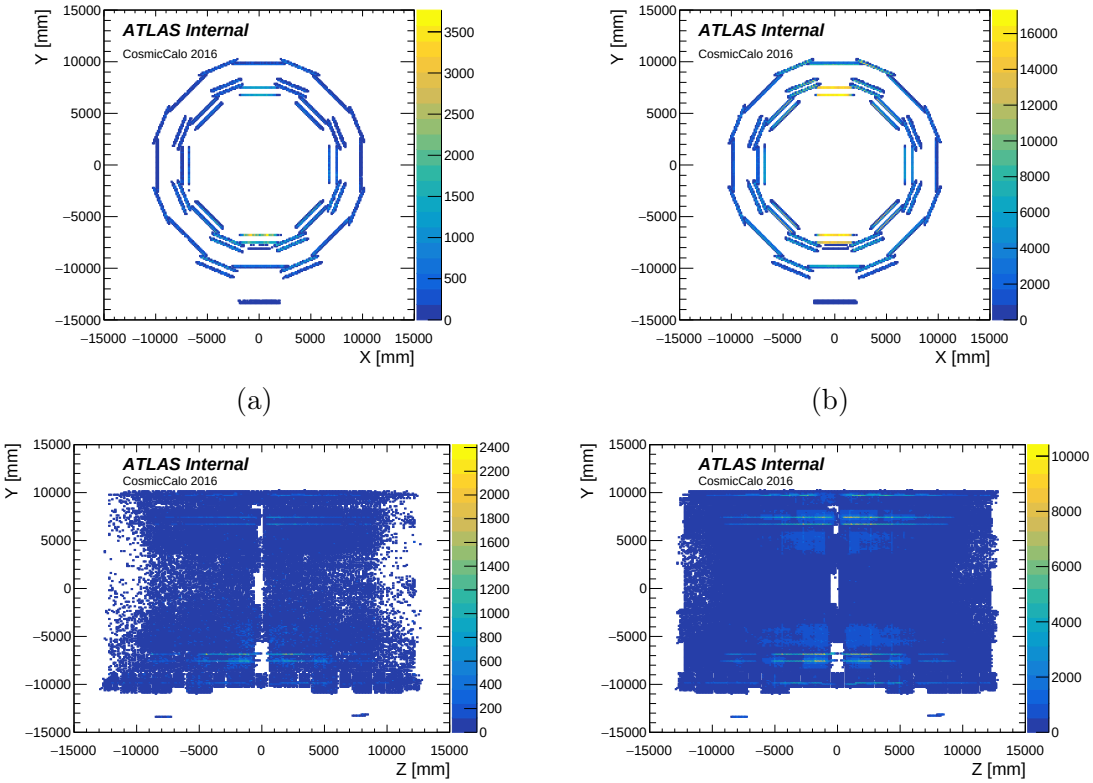

Figure 5.6: (a) and (b): distribution of RPC hits in the x-y plane for mu and single jet triggers respectivley. (c) and (d): the same distributions seen in the y-z plane.

and not adjusted for cosmic muons. The hit signals are internally aligned by applying 3 ns delays so that the hits belonging to the same particle arrive at the same time at the input of the front-end electronics performing the trigger algorithm. Cosmic muons in the top hemisphere of ATLAS travel the "wrong way" or "backwards in time" wrt muons from collisions. In the ATLAS top hemisphere the trigger arms of the low-p_T roads are short enough that the ToF of the cosmic muons is negligible and the low-p_T road trigger algorithms are always satisfied. For cosmic muons in the top hemisphere the high-p_T road trigger algorithms are less likely to be satisfied because the length of the trigger arm is so large that the ToF is larger than 3 ns and the hit signals in the innermost and outermost RPC stations will not be aligned. In fact, out of a total of 36924445 events only 606758 have been identified as muon events and of these only 3 are high-p_T muon events. Almost all triggers fired are MU6 and MU11.
Fig. 5.7 shows, as done in the case of normal p-p collisions, the RPC hit time distributions on the 3 layers defined above for the top and bottom ATLAS hemisphere. The distributions show times centered at t = -60 ns for layer 1 top and times centered at -40 ns for the other two layers. In the case of the bottom hemisphere we find times centered around 10 ns for all three layers. Therefore the time difference between layer 3 and 1 will be different from zero only in the case of the top hemisphere. That is, cosmic muons will be distinguishable from muons coming from p-p collisions only in the top hemisphere using the RPC timing only, as shown in Fig. 5.8.

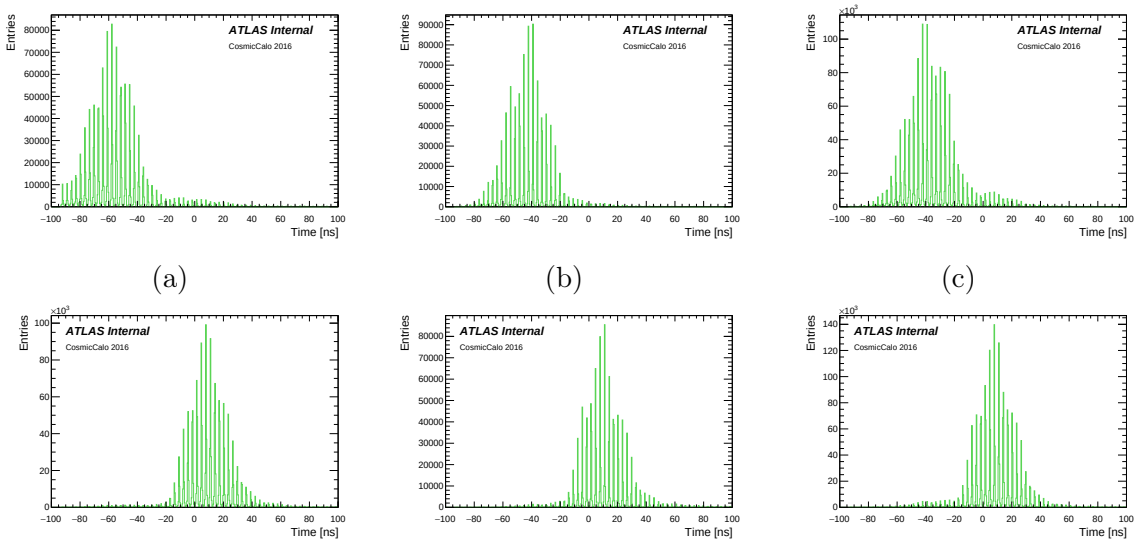

(a) (b) (c)

(d) (e) (f)

Figure 5.7: (a),(b),(c): RPC time distribution in the top hemisphere for layer 1, 2 and 3 respectivley in the mu trigger case. (c),(d),(e): RPC time distribution in the bottom hemisphere for layer 1, 2 and 3 respectivley in the mu trigger case.

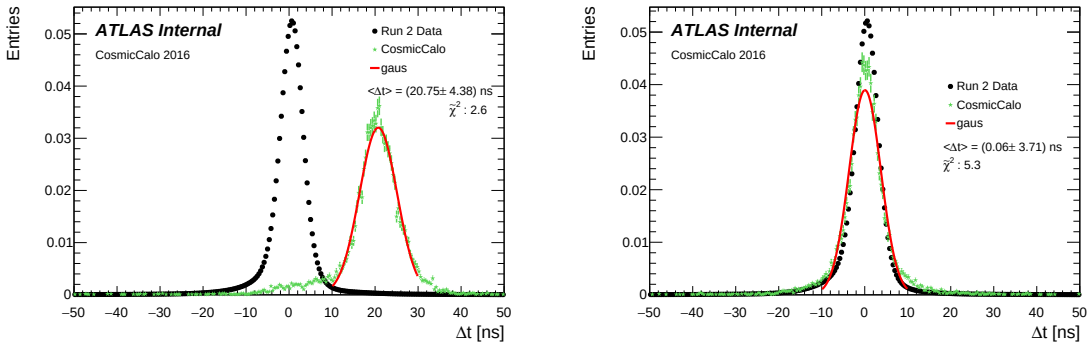

(a) (b)

Figure 5.8: (a): RPC time difference between layer 1 and layer 3 in top hemisphere for CosmicCalo stream (green dots) and Main stream (black dots). The average Δt values of the distributions are spaced by 20 ns. (b): the same distributions in the bottom hemisphere. No differences in time between CosmicCalo and Main streams are observed.

Chapter 6

Standalone Vertex Reconstruction in the Muon Spectrometer

A number of extensions to the Standard Model (SM) predict, at the LHC energy, the production of particles that are neutral, weakly interacting and long-lived, with final state decays that may contain SM particles. These neutral particles with long decay path represent, from an experimental point of view, a challenge for the reconstruction capabilities of the LHC detectors. If their lifetimes are long enough, there will be a non negligible number of decays in the external layers of the detectors and in particular in the MS. This chapter deals with the development of a vertex reconstruction algorithm using standalone MS tracks only. The algorithm is implemented only on Monte Carlo (MC) data. Then we will briefly describe the MC benchmark model and its simulation inside the ATLAS detector. Then we move on to describe the vertex reconstruction algorithm and therefore the results obtained.

6.1 The Benchmark Model

Among the numerous models predicting dark photons, one class particularly features a hidden sector communicating with the SM through the Higgs portal for production and through vector portal for decay. The benchmark model used in this vertex reconstruction is the Falkowski–Ruderman–Volansky–Zupan (FRVZ) model [2] , where a pair of dark fermions f_{d_2} is produced via a Higgs boson (H) decay. In particular it is considered the model involving the production of two dark photons γ_{dark}. Each dark fermion decays into a γ_{dark} and a lighter dark fermion assumed to be the hidden lightest stable particle (HLSP), see Fig. 6.1.
The number of radiated dark photons is proportional to the size of the dark gauge coupling α_d [4]. In the benchmark model used $\alpha_d = 0.01$. The vector portal communication of the hidden sector with the SM is through kinetic mixing of the dark photon and the standard photon

$$L_{gauge\ mixing} = \frac{\epsilon}{2} B_{\mu\nu} b^{\mu\nu}$$

where $B_{\mu\nu}$ and $b^{\mu\nu}$ denote the field strengths of the electromagnetic fields for the SM and dark sector respectively, and ϵ is the kinetic mixing parameter. ϵ, which can vary over a wide range of values ($\simeq 10^{-11}$-10^{-2}), determines the lifetime of the dark photon. For a small kinetic mixing value, the γ_d has a long lifetime, so that it decays at a macroscopic

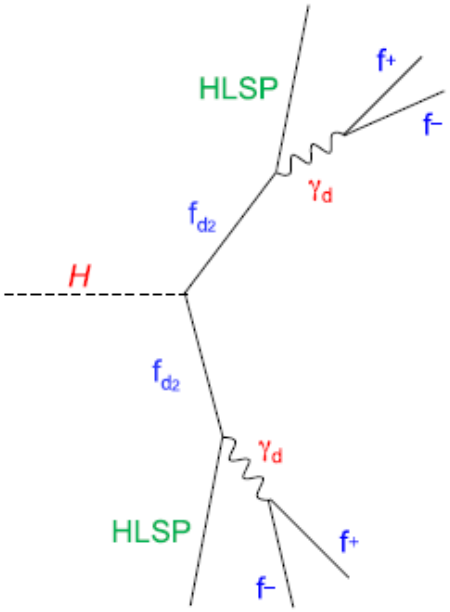

Figure 6.1: The process of the FRVZ model used as model benchmark. The dark fermion f_{d_2} decays into a γ_d and an HLSP. The γ_d decays into SM fermions, denoted by f^+ and f^-.

distance from its production point. A dark photon with a mass m_{γ_d} up to a few GeV that mixes kinetically with the SM photon will decay into leptons or light mesons, with branching fractions that depend on its mass. The mean lifetime τ , expressed in seconds, of the γ_d is related to the kinetic mixing parameter [3] by the relation

$$\tau \propto \left(\frac{10^{-4}}{\epsilon}\right) \left(\frac{100\ MeV}{m_{\gamma_d}}\right)$$

For a small kinetic mixing value, the γ_d has a long lifetime, so that it decays at a macroscopic distance from its production point. Due to their small mass, the dark photons are expected to be produced with large boosts, resulting in collimated groups of leptons and light hadrons in a jet-like structure, referred to as Dark-Photon Jets (DPJs)

6.2 The MC Sample

The Monte Carlo (MC) simulation sample used is generated using *MadGraph*5 [7] interfaced to *Pythia* [17] and processed through a full simulation of the ATLAS detector geometry and response using the *Geant*4 [10] toolkit. The simulated detector response to the MC input is therefore organized in data containers of the xAOD type [55].
The MC sample is generated for the Higgs boson mass of 125 GeV. The mass of the hidden fermion $m_{f_{d_2}}$ and of the hidden scalar m_{s_d} are low relative to the H mass. The dark-photon mass is 0.4 GeV, above the pion pair mass threshold, and the γ_d decay branching fractions (B) are $B(\gamma_d \to ee) = 45\%$, $B(\gamma_d \to \mu\mu) = 45\%$, $B(\gamma_d \to \pi\pi) = 10\%$. The proper decay length $c\tau$ of the γ_d is equal to 49.3 mm, such that $\simeq$80% of the decays occur in the volume delimited by the muon trigger chambers, i.e. up to 7 m in radius and 13 m along the z-axis. Fig. 6.2a shows the Z coordinate distribution of the γ_d decay vertex position in the ATLAS detector. Fig. 6.2b shows the R coordinate distribution of the vertex posi-

tion. Near the IP there is the highest density. Density that decreases exponentially for increasing R and Z, see Fig. 6.2b.

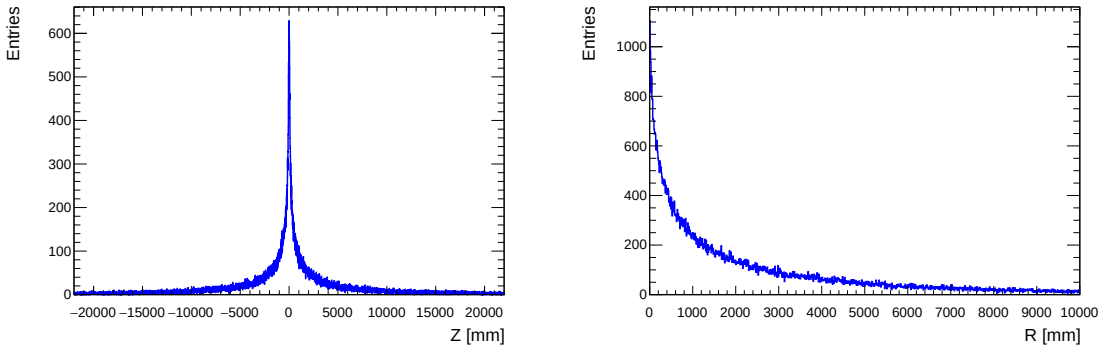

(a) (b)

Figure 6.2: (a): Z coordinate distribution of the γ_d decay vertex position. (b): R coordinate distribution of the γ_d decay vertex position.

DPJs are reconstructed in the ATLAS detector with criteria that depend on the γ_d decay channel. A γ_d decaying into a muon pair is searched for by looking for two closely spaced muon tracks in the MS, while a γ_d decaying into an electron or pion pair, given the high boost of the γ_d, is searched for as an energy deposit in the calorimeters identified as a single narrow jet. In particular the MC shows that the γ_d decay products are contained, in 90% of cases, within a cone of size $\Delta R = 0.4$. Fig. 6.3 shows the ΔR distribution of the muon tracks deriving from the decay of a reconstructed γ_d, in the ATLAS detector.

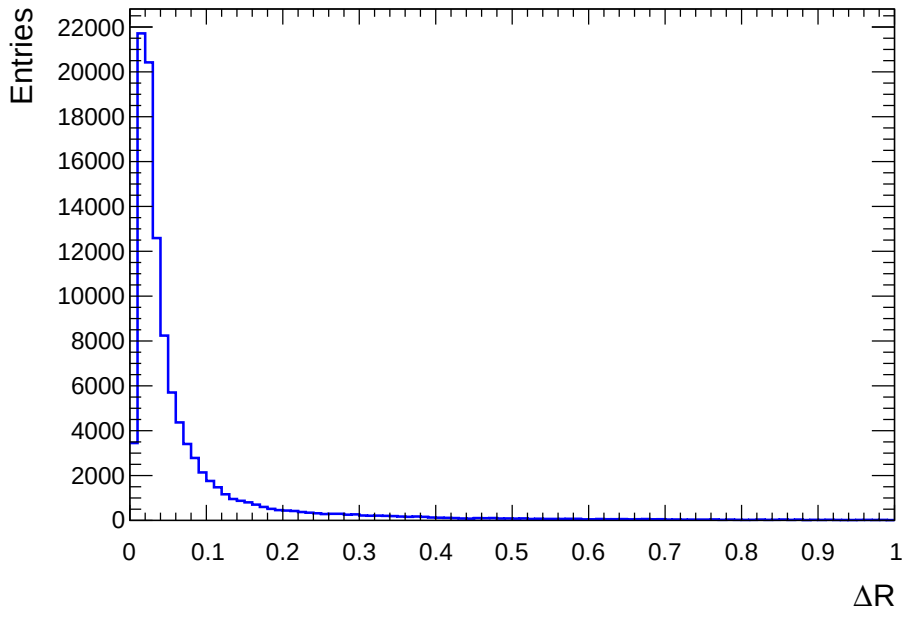

Figure 6.3: Muon tracks ΔR distribution for the $\gamma_d \rightarrow \mu^+\mu^-$ decay. Almost all the muon tracks associated with this decay are contained in a cone of size 0.4

6.3 Vertex Reconstruction in the Muon Spectrometer

The γ_d decay vertex reconstruction takes into account only the $\mu^+\mu^-$ decay channel that occur outside the calorimeter system, therefore the decay vertices can be reconstructed using only the standalone muon tracks. The vertex reconstruction algorithm obviously takes into account the different spatial arrangement of the MS chambers in the barrel and in the endcap regions.

6.3.1 Vertex Reconstruction in the Barrel Region

In the barrel region are recontructed only the truth vertices that are located at a distance from the beam line between 3800 mm and 9000 mm, or in the region included between the outside of the calorimeter system and the outer MS chambers. Vertices pointing toward the magnetic transition region ($1.0 < |\eta| < 1.05$), have been excluded. Two standalone muon tracks are then selected for each vertex. These tracks must be contained within a cone of width $\Delta R = 0.4$ and must point in the direction of the truth decay vertex. No conditions on the p_T are applied. Once the tracks have been selected, the radius of the first hit is extracted from the $TrackParticle_v1$ xAOD container by means of the $radiusOfFirstHit()$ (RoFH) method. This parameter tells us what is the distance between the beam line and the first hit generated in the MS chambers by the muon in the x-y plane. Fig. 6.4 shows the distribution of the RoFHs for some reconstructed standalone muon tracks. The peaks are located at the MS chambers location, between 3800 and 8000 mm.

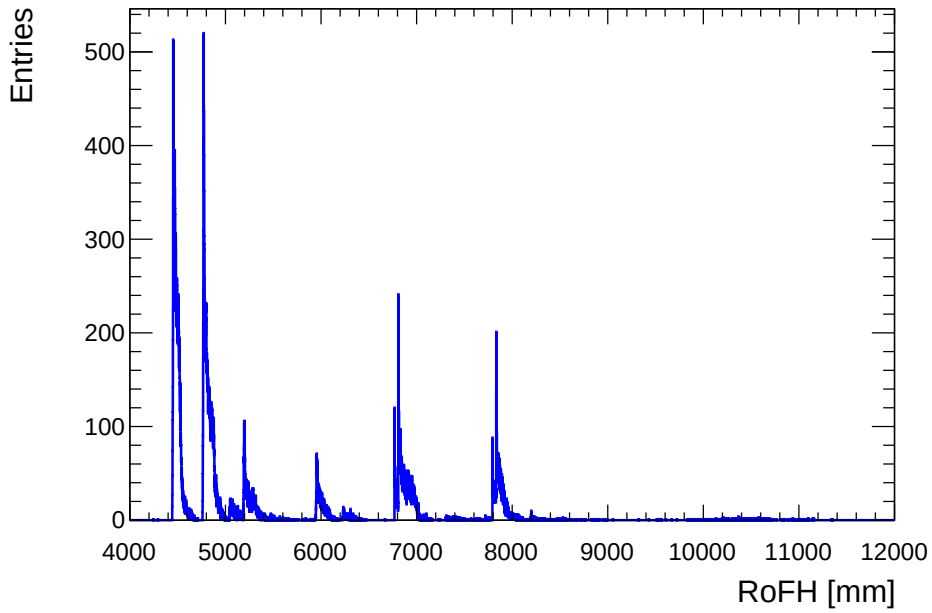

Figure 6.4: Radius of first hits distribution in the barrel MS. These are located between 3800 mm and 8000 mm.

A track is characterized by 5 parameters, d_0, z_0, ϕ_0, θ_0 and q/p. These parameters can be exploited to determine, through the use of *Extrapolator* tool [51], the coordinates of the intersection point between the track and a specific surface inside the detector. It is therefore possible to perform a back-extrapolation of the muon track trying to determine

the point where it was created, that is the γ_d decay vertex. Having determined the RoFH in the MS associated with a track, we build a cylindrical surface whose axis corresponds to the beam and that have a radius is r = RoFH and e total lenght of 10000 mm. We therefore extrapolate the intersection point P(x, y, z) between the track and this surface and then we move to a cylindrical surface with a smaller radius. This process is repeated, in steps of 50 mm, on concentric cylindrical surfaces, moving up to a distance from the beam line of just under 3800 mm. At the end of the process we will have a curve with n points that represents the path of the muon inside the MS (see Fig. 6.5).

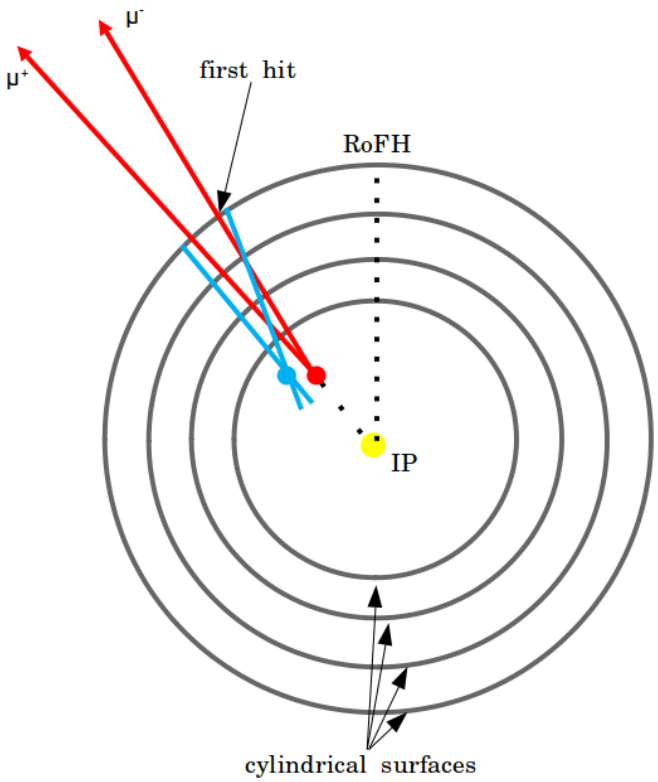

Figure 6.5: An explanatory sketch of the reconstruction algorithm for the barrel region. The muon tracks deriving from the γ_d decay are represented in red. The vertex of truth decay is the red dot. The blue lines indicate the reconstructed curves that cross the cylindrical surfaces of radius equals to RoFH rapresented in gray. The blue dot indicate the reconstructed vertex position.

Once the back-extrapolations of the selected tracks have been performed we can determine the point of maximum approach between the two curves. The point of maximum approach will be that for which the Euclidean distance between the two curves will be minimal. To the point of maximum approach we will associate the reconstructed decay vertex.
Using this algorithm, the γ_d decay vertices are reconstructed with a resolution of about 50 cm in r and 24 cm in z, as shown by the results of the Gaussian fit calculated on the residuals of these coordinates calculated wrt the the truth vertex R_{truth} and $Z_t ruth$ coordinate (Fig. 6.6). The residuals between the reconstructed and truth vertices of the polar (θ) and azimuthal (ϕ) angles are shown in Fig. 6.7.

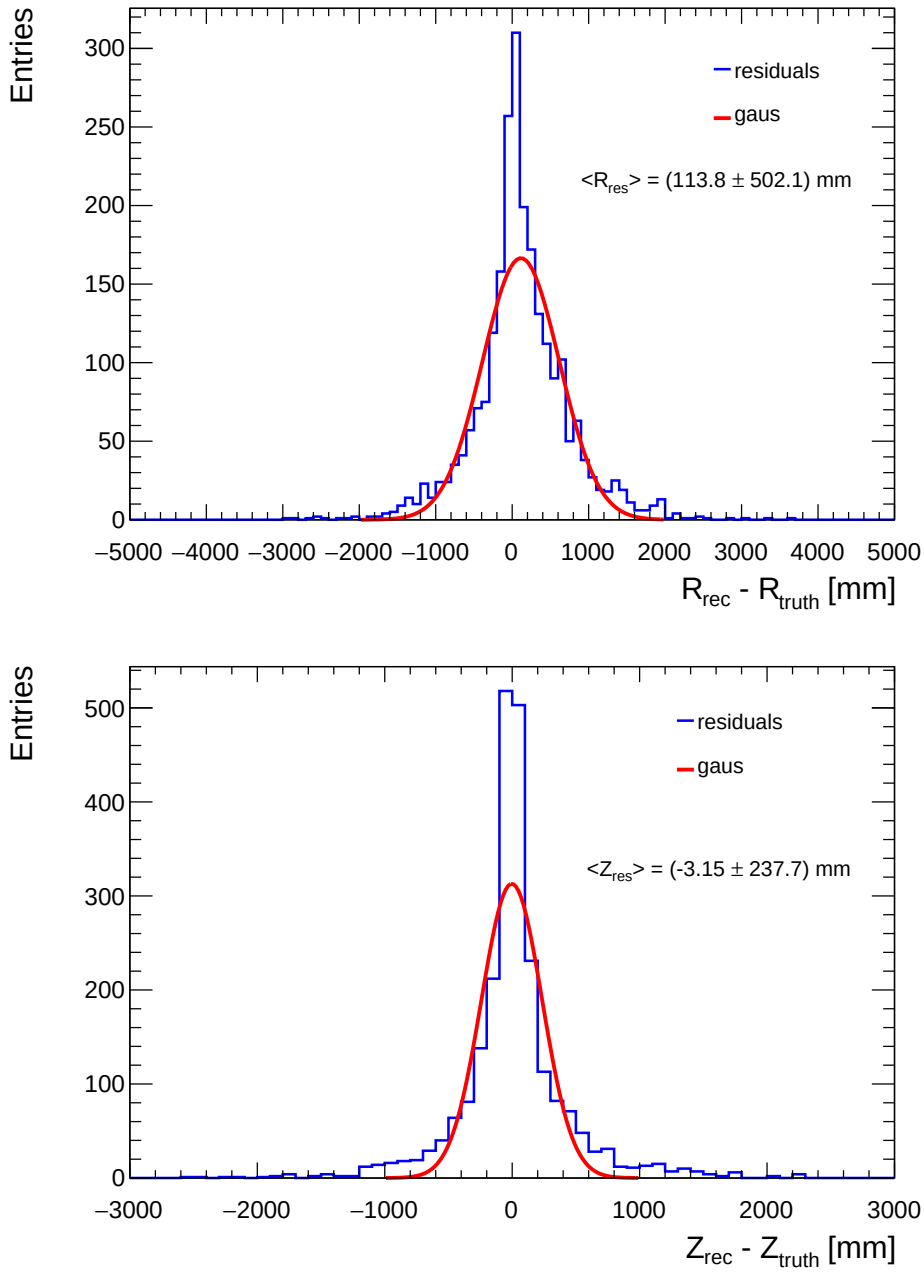

Figure 6.6: Residuals of the R (top) and Z (bottom) coordinates between the reconstructed and truth vertex positions.

6.3.2 Vertex Reconstruction in the End-Cap Regions

Decays in the end-cap MS must occur in the range $7 < Z < 14$ m to be detectable. Muons with low momentum from decays that occur before 7 m will not have enough energy to reach the MS middle station, while decays occurring after the middle station (over 14 m) will not be seen. This implies that most of the detectable decays will occur inside the toroid, so the tracks with their parameters will be reconstructed after the muon has been curved by the magnetic field. This will lead to a systematic shift in the position of the reconstructed vertex and a degraded resolution wrt the vertices found in the barrel region. The algorithm for the vertex reconstruction in the end-cap regions is similar to that used in

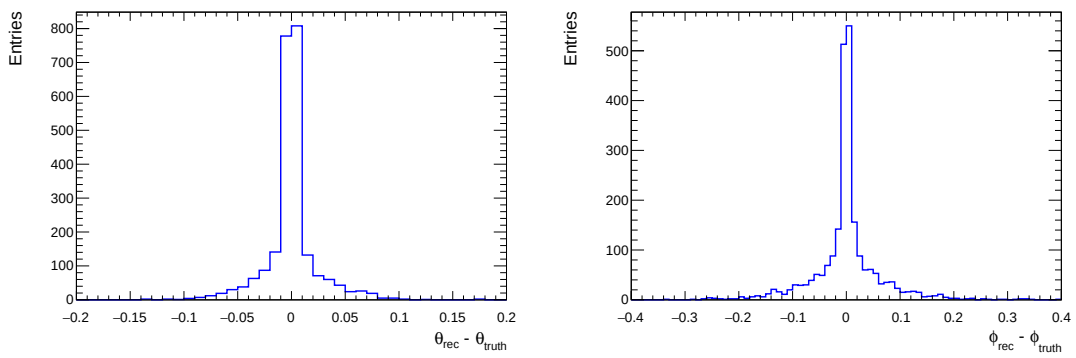

Figure 6.7: Residuals of θ (left) and ϕ (right) angles between the reconstructed and truth vertex positions.

the case of the barrel region, but in this case the surfaces on which the back-extrapolation is performed are disks with a radius equal to RoFH positioned transversely to the beam axis, see Fig. 6.8.

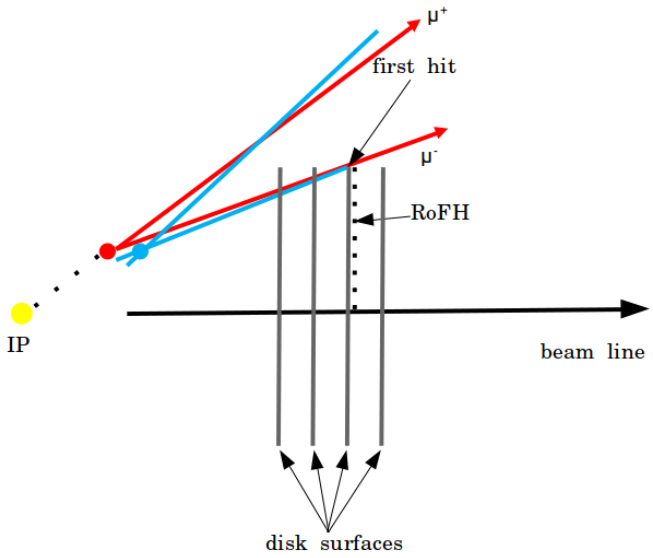

Figure 6.8: An explanatory sketch of the reconstruction algorithm for the end-cap regions. The muon tracks deriving from the γ_d decay are represented in red. The vertex of truth decay is the red dot. The blue lines indicate the reconstructed curves that cross the disk surfaces of radius equals to RoFH rapresented in gray. The blue dot indicate the reconstructed vertex position.

Once the two tracks have been selected, back-extrapolation is carried out on these surfaces at steps of 50 mm from z = +/- 14000 mm to z = +/- 6800 for forward/backward direction. The point of maximum approach between the back-extrapolated curves is associated to the reconstructed γ_d vertex position. The R, Z, θ and ϕ residuals of reconstructed vertex positions wrt the truth vertex positions are shown in Fig. 6.9.

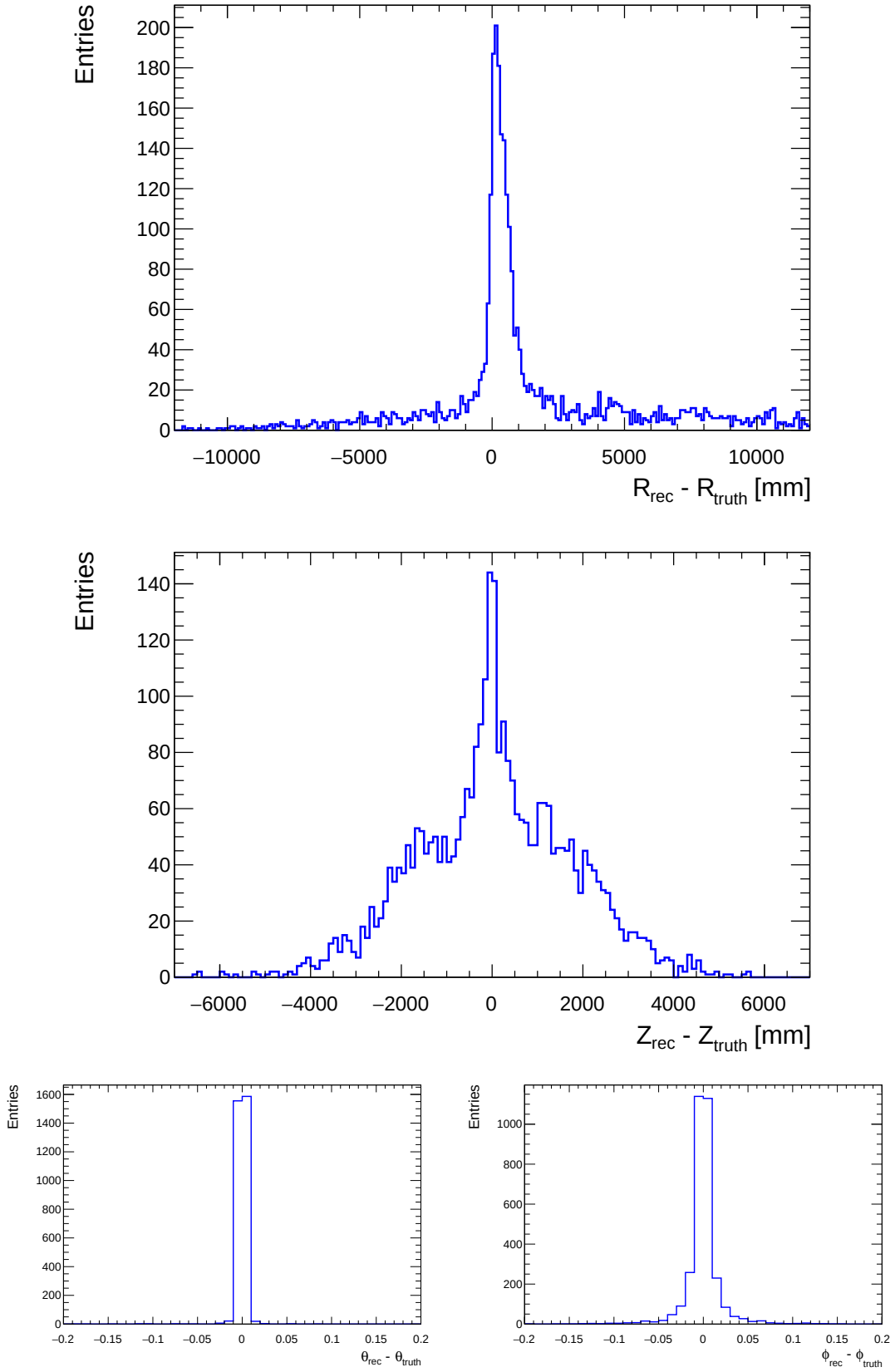

Figure 6.9: Residuals of the R (top) and Z (middle) coordinates of the reconstructed vertex positions wrt truth vertex positions. (bottom): θ (right) and ϕ (left) residuals.

Conclusions

This thesis deals with different aspects of experimental physics, focusing on the description of the construction techniques and test methodologies adopted in the mass production of the SM1 MM 4-plets of the ATLAS NSW project.
Particular attention is paid to the preparation and finalization phases of the drift panels which are carried out at the Cosenza and LNF laboratories, respectively.
The procedure and the instrumentation developed "ad hoc" for these phases gave excellent results. As we could see, the mechanical, electrical and gas tightness specifications have been largely satisfied for all the drift panels. Furthermore, the organization with which these phases were carried out made it possible to finish the work in a short time.
All the methods and related instruments necessary to perform the tests for the drift panels validation are developed and improve at the Cosenza laboratory.
Among the many it is worth mentioning the instrument (improperly called "limbo") designated to measure the height of the panel from the reference surface (optical table). This allows you to appreciate heights with the resolution of μm with a repeatability of few μm. The instrument is composed of 10 linear gauges with digital output read by a PC which stores the collected data and measures the average thickness and the deviation from theoretical flatness.
Another is the so-called local gas tightness test, thought of as a pass/no pass test. This method gave us the possibility to quickly and easily identify the gas leak sources on the panel and then remedy on them before continuing in the subsequent processing phases.
Another one is the global gas tightness test, based on the pressure drop method adapted to the case in which the container is not totally rigid. This method contains corrections to systematic errors due to variations in atmospheric pressure and temperature on the gas leak rate estimation. Chapter 4 has been dedicated to the discussion of this method. We started from the ideal gas equation, then introduce the corrective terms necessary to make the system independent from environmental parameters changes, taking into account, through the so called damping coefficient α, the vessel walls deformability. With this method we are able to appreciate gas losses of the range of $[10^{-5}, 10^{-6}]$ l/min. We have shown that the gas losses measured in the case of deformable volume are consistent with those determined using the acclaimed pressure drop method for a volume with non-deformable walls. The results obtained are in agreement with what is more recent in the specific literature.
The HV stability detector problem is also addressed. The discharge formation main causes have been identified and it has been described how to reduce their impact on the detector HV stability.
The problem of the ROP resistive layer layout has been addressed. Systematic studies on the read out strips resistance value is done. Such studies have highlighted the weaknesses of the resistive layout.
The second part of the thesis, or chapters 5 and 6, focuses on two different topics.

Chapter 5 is dedicated to the study of the cosmic rays background inside the ATLAS cave. We have seen how the ATLAS experiment it is constantly crossed by the most energetic cosmic muons despite being at a depth of about 100 m underground. Cosmic muons can cross the ATLAS experiment, and in particular the muon spectrometer, coinciding with the bunch crossing in the normal p-p collisions. Consequently, it is necessary to be able to distinguish between cosmic muons and those coming from the interaction point, especially when studying vary rare events. One way to do this is to exploit the RPCs timing, which we have seen to be correct considering the ToF. During the normal p-p operations, and therefore studying the RUN 2 stream, the temporal distribution of muon hits is centered at zero. When we analyze, using the CosmiCalo 2016 stream, the temporal distribution of cosmic muon hits we can distinguish two different situations. In the upper hemisphere the distribution is centered towards negative time values as the muon cosmic passes through the spectrometer from the outside to the inside, that is, it travels in the wrong direction. In this case the muon cosmic seems to travel "back in time". In the spectrometer lower hemisphere the hits time distribution appears to be centered in zero. In this case the muon travels in the correct direction and for the RPC system it seems to come from the interaction point. Consequently we can distinguish cosmic muons from muons coming from p-p collisions by exploiting only the timing of the RPCs only in the upper hemisphere of the spectrometer.
The last topic, discussed in chapter 6, concerns the development of an algorithm capable of reconstructing the decay vertices by exploiting the only muon spectrometer stand-alone tracks. The algorithm makes use of a backward extrapolation of the tracks parameters starting from the point where the spectrometer recorded the first hit. The algorithm was only tested on an MC sample in which dark photons γ_d decays in 45 % of cases in a $\mu^+\mu^-$ pair. It is therefore only calibrated for a two-muon decay. Once the muon tracks have been selected within a cone large ΔR, the extrapolation is carried out until the point of minimum approach between the two tracks is reached. To this point we have associated the reconstructed vertex position. Comparing the position of the reconstructed vertex with the position of the true vertex, the resolution of the algorithm was determined for both the barrel and the end-cap regions in both radial and longitudinal direction. The vertex reconstruction resolution (5% - 10%) is found to be, in the barrel region, better than the end-cap ones. Resolution in the end-cap regions degrades. In the end-cap region we have seen most of the decays occur within the toroids and therefore we have track information only after they have been deflected by the magnetic field.
The ATLAS experiment represents an important part of the high energy physics. It is the place where the "craziest" physical hypothesis become laws. It is the place where yesterday dreams become and will become the reality of today and tomorrow. The small part I played in this experiment was the realization of one of my dreams and what is even more important is that the work done in the past years will continue to make dreams come true.

Appendices

Appendix A

Global GTT Stand

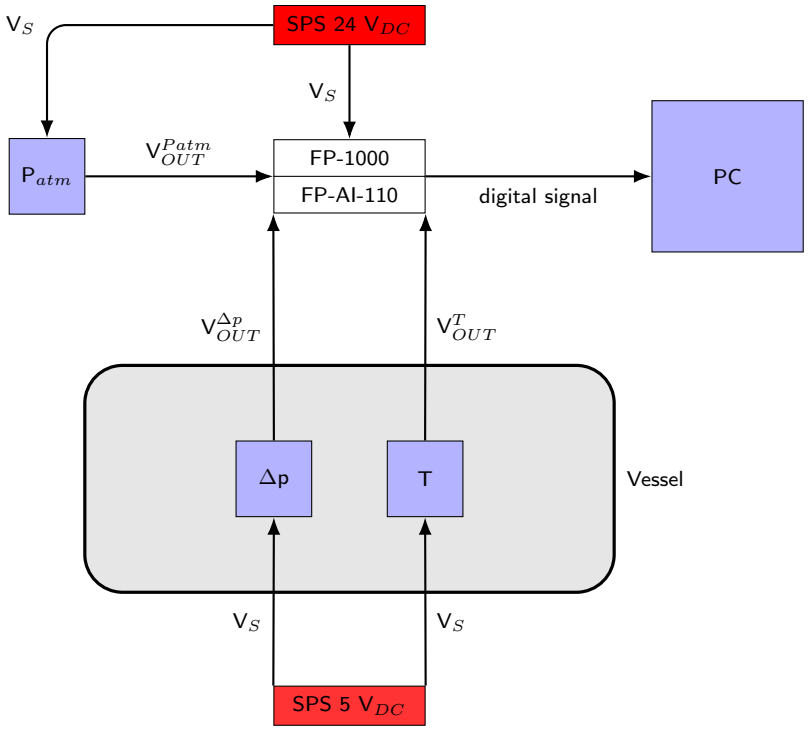

Figure A.1: A graphical scheme of the global GTT stand. The 144SC0811BARO [1] barometric sensor is placed near the trapezoidal table. It is power supplied by the 24 V_{dc} Switching Power Supply (SPS). The HCLA12X5EU [39] differential pressure sensor and the LM35DZ [44] temperature sensor, power supplied by 5 V_{dc} SPS, are integrated in the dpTOP. Their analog signal is digital converted from the FP-AI-110 [34] 16-bit ADC module.
The temperature sensor V_{OUT}^{T} is connected to the 0-1 V input channel ADC module that has 20 μV resolution. The barometric and differential pressure sensors V_{OUT}^{Patm} and $V_{OUT}^{\Delta p}$ are connected to two different 0-5 V input channels of the ADC module. The latter have 95 μV resolution. The FP-AI-110, power supplied by 24 V_{dc} SPS, is connected to the FP-1000 [49] network interface.

Appendix B

Resistance Mappings

In this appendix we report the resistance mappings not shown in the text. Resistance mappings were also carried out keeping us perpendicular to the strips and recording the resistance values always in the middle between two ladders ($SS1_{1086}$ L_{perp} and $SS1_{1106}$ L_{perp}). In this case the arc behavior is obviously suppressed.

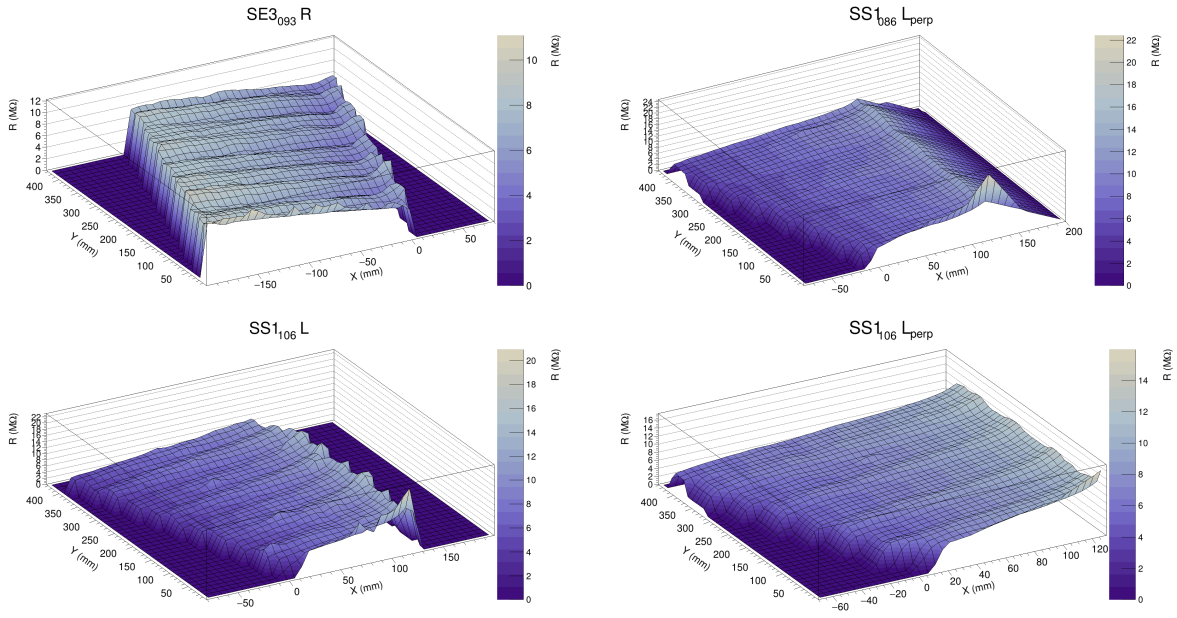

Figure B.1: Other resistance mappings.

Appendix C

Cleaning Procedure

C.1 Mesh Washing Procedure

Before being glued on the DP the mesh must be washed. For this purpose, a special washing cabin was built outside the CR2, which can accommodate not only the transfer frame with the mesh but also the complete DP and the ROP (we remind you that these must be washed before proceeding with the 4-plet assembly), see Fig. C.1. Washing the mesh is mainly aimed to reduce the presence of grease, resulting from industrial processing, on its surface. The mesh washing procedure includes the following operations:

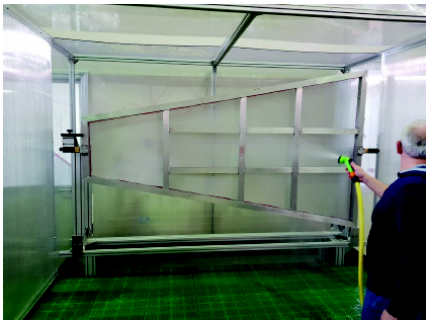

Figure C.1

- get wet the mesh by hot tap water (40 - 45)°;
- pass the brush soaked in a degreaser solution (10 g NGL® 17.40 dissolved in 1.5 l of hot tap water) with circular movement on first mesh side;
- repeat the last operation on second mesh side;
- wait 10 min for the degreaser to act;
- rinse the two mesh face using large amount of hot tap water passing the brush with circular movements;
- rinse the two mesh face using large amount of deionised water using a high pressure (60 - 70) bar Karcher®, kept the lance at a safe minimum distance of about 50 cm from the mesh in order to remove the tap water, which could contaminate the mesh and the panel with mineral deposits;
- visual check to verify the correct cleaning;
- leave to drain for 15 min in the washing cabine.
- after washing, the mesh is left to dry in the CR2 for about one day before its gluing on the DP.

C.2 Drift Panel Assembly Preparation

Preparing the DPs for 4-plet assembly consists of the following operations.
The gas-gap frame is screwed to the panel at a distance of 7 mm from the mesh frame so as to form the O-ring groove. The distance of 7 mm is fixed thanks to the aid of two plastic spacers (7 mm width) that are placed against the mesh frame, then the bars and the corners of the gas gap frame are pressed against the spacers and screwed. The DP is then inserted into the washing cabine and first of all subjected to cathode mesh polishing with 2000/2500 grade sandpaper. Once the mesh polishing is finished, no check is performed to verify the actual lack of spikes on the mesh surface. After the mesh polishing, the panel is washed following the same procedure adopted in the case of the mesh washing with the foresight to spray the de-ionized water under pressure inside the gas distribution pipes. In addition to cleaning the internal surface of the pipes, this operation also allows us to check that they are not obstructed by glue. Clean room tissues and nitrogen flux are used to remove the water drops from assembly holes and gas distribution pipes. The DP is left to dry in the drying station for a minimum of 48 hours before 4-plet assembly.

C.3 Read Out Panel Assembly Preparation

The following operation are performed in order to prepare the ROP for the 4-plet assembly:

- after a visual inspection of the ROP surfaces, the panel is washed a first time to clean the area which will be covered by glue with the edge-passivation procedure;
- once the applied glue is completely cured on both sides of the panel the panel is inserted into the washing cabin;
- the edge of the panel and then the assembly and alignment holes are covered with kapton;
- a polishing of the passivated region by means of a brush and pumice powder so to flatten any tips is performed;
- an accurate washing of the panel surfaces by means of tap water (40-45)° C, a micro-crystal creamy detergent (e.g. CIF) and a soft brush.
- washing and rinsing are performed until any soap residual is removed;
- the last two operation are repeated twice for each panel surface;
- jets of deionized water are used for the final rinsing;
- leave to drain for 15 minutes in the washing cabine;
- clean room tissues and nitrogen flux are used to remove the water drops from rim and assembly holes;
- The ROP is left to dry in the drying station for a minimum of 48 hours before 4-plet assembly.

Appendix D

ATLAS Gas Leak Rate Limit for the SM1 MM Singlet

Consider a chamber with a volume V filled with an ideal gas at pressure p and temperature T. This system can be described by the ideal gas law:

$$pV = nRT$$

where n is the number of gas moles and R the ideal gas constant.
The gas leak rate of the system Q_l for T = T_0 = cost. can be expressed as the leaking quantity of substances $\frac{dn}{dt}$

$$Q_l = \frac{dn}{dt}RT_0 = \frac{d}{dt}(pV) = V\frac{dp}{dt} + p\frac{dV}{dt}$$

Three cases can be distinguished:

$$V = V_0 = cost. \Rightarrow Q_l = V_0\frac{dp}{dt} \tag{D.1}$$

$$p = p_0 = cost. \Rightarrow Q_l = p_0\frac{dV}{dt} \tag{D.2}$$

$$pV = p_0V_0 = cost. \Rightarrow Q_l = V_0\frac{dp}{dt} + p_0\frac{dV}{dt} = 0 \tag{D.3}$$

In the event that our system has V_0 = cost., we can use Eq. D.1 to evaluate the gas leak rate Q_l. The ATLAS specifications allow a maximum pressure drop rate of 0.6 mbar/h at 3 mbar overpressure, or, using the Eq. D.3, in terms of volume

$$\frac{dV}{dt} = -\frac{V_0}{p_0}\frac{dp}{dt} \simeq 10^{-5}V/min$$

with p_0 = 1013.2 mbar. For a single SM1 MM gas gap with a volume V $\simeq$ 7.5 l the maximum allowed gas leak rate is Q_l = 4.5 mbar l/h or written in terms of volume Q_l = $7.5 \cdot 10^{-5}$ l/min.
Let's introduce another relation that will come in handy later. Consider two different non-deformable volumes V and V'. Let's assume that are characterized by an equal gas leak rate. Then we can write:

$$Q_l = Q'_l \Rightarrow V\frac{dp}{dt} = V'\frac{dp'}{dt} \Rightarrow \frac{dp'}{dt} = \frac{V}{V'}\frac{dp}{dt} \tag{D.4}$$

therefore with the same gas leak rate the dp'/dt grows linearly as V/V'.

Name Index

Bibliography

[1] *144S...-PCB Series, Signal conditioned precision pressure transducers*. URL: https://dtsheet.com/doc/1339388/144s...-pcb-series.

[2] A. Falkowski et al. "Hidden Higgs decaying to lepton jets". In: *JHEP* 5.077 (2010).

[3] C. Cheung et al. "Kinetic mixing as the origin of a light dark-gauge-group scale". In: *Phys. Rev. D* 80.035008 (2009).

[4] C. Cheung et al. "Lepton jets in (supersymmetric) electroweak processes". In: *JHEP* 4.116 (2010).

[5] D. E. Groom et al. *MUON STOPPING POWER AND RANGE TABLES 10 MeV - 100 TeV*. Tech. rep. 2001.

[6] D. S. Bhattacharya et al. "A numerical study on the discharges in Micromegas". In: *arXiv:1907.08955v1* (2019).

[7] J. Alwall et al. "The automated computation of tree-level and next-to-leading order differential cross sections, and their matching to parton shower simulations". In: *JHEP* 7.079 (2014).

[8] O. Sahin et al. "Penning transfer in argon-based gas mixtures". In: *Jinst* 5 P05002 (2010).

[9] R. Alemany-Fernandez et al. *Operation and Configuration of the LHC in Run 1,* Note 0041. 2013.

[10] S. Agostinelli et al. "GEANT4: a simulation toolkit". In: *NIMA* 506.250 (2003).

[11] T. Alexopoulos et al. "A spark-resistant bulk-micromegas chamber for high-rate applications". In: *NIMA* 640 (2011), pp. 610–618.

[12] T. Alexopoulos et al. "Construction techniques and performances of a full-size prototype Micromegas chamber for the ATLAS muon spectrometer upgrade". In: *NIMA* 955.162086 (2020). URL: https://doi.org/10.1016/j.nima.2019.04.040.

[13] T. Alexopoulos et al. *Design of the NSW Gas Distribution System for Micromegas Detectors*. Note. 2015.

[14] T. Alexopoulos et al. *Determination of the Feasible Gas Sealing Level of the NSW Micromegas Quadruplets*. Note. 2017.

[15] T. Alexopoulos et al. *Impact of the Temperature Variations to the Sealing Performance of the NSW Micromegas Quadruplets*. Note. 2019.

[16] T. Alexopoulos et al. *Stereo Information in Micromegas Detectors*. Note. 2015.

[17] T. Sjostrand et al. "An introduction to PYTHIA 8.2". In: *Comput. Phys. Commun.* 191.159 (2015).

[18] Y. Giomataris et al. “MICROMEGAS: a high-granularity position-sensitive gaseous detector for high particle-flux environments”. In: *NIMA* 376.29-35 (1996).

[19] S. F. Biagi. “Monte Carlo simulation of electron drift and diffusion in counting gases under the influence of electric and magnetic fields”. In: *NIMA* 421.234-240 (1999).

[20] A. Blanc. “Recherches sur le mobilités des ions dans les gaz”. In: *J. Phys. Theor. Appl.* 7.825 (1908).

[21] J. Bortfeldt. “Development of Floating Strip Micromegas Detectors”. PhD thesis. Fakultat fur Physik der Ludwig-Maximilians-Universitat Munchen, 2014.

[22] *The ATLAS New Small Wheel project: SM1 drift panels assembly and finalization*. Nuovo Cimento C, 2020. URL: https://inspirehep.net/literature?sort=mostrecent&size=25&page=1&q=g%20carducci&author_count=Single%20author.

[23] G. Chiodini and S. Spagnolo. “Off-line time calibration of the ATLAS RPC system”. In: *Jinst* 8.T02004 (2013).

[24] ATLAS Collaboration. “The ATLAS Experiment at the CERN Large Hadron Collider”. In: *Jinst* 3.S08003 (2008).

[25] ATLAS Muon Collaboration. *ATLAS Muon Spectrometer*. Technical Design Report 10. 1997.

[26] The ATLAS Collaboration. “Muon reconstruction and identification efficiency in ATLAS using the full Run 2 *pp* collision data set at $\sqrt{s}$ = 13 TeV”. In: (2020). arXiv: 2012.00578.

[27] The ATLAS Collaboration. “Operation of the ATLAS trigger system in Run 2”. In: *Jinst* 15.P10004 (2020).

[28] The ATLAS Collaboration. “Performance of the ATLAS RPC detector and Level-1 muon barrel trigger at $\sqrt{s} = 13$ TeV”. In: (2021). arXiv: 2103.01029.

[29] M. J. Druyvesteyn and F.M. Penning. “The mechanism of elelectric discharges in gases of low pressure”. In: *Rev. Mod. Phys.* 12 (1940), pp. 87–174.

[30] A. C. Dudder. “First Measurement of the Branching Ratio Fraction BR(W $\rightarrow \tau\nu \rightarrow \mu\nu\nu$)/BR(W $\rightarrow \mu\nu$) in $\sqrt{s}$ = 7 TeV Proton-Proton Collisions with the ATLAS Detector and Realization of a Production Facility for Large Scale Micromegas Drift Boards”. PhD thesis. 2019.

[31] Lyndon Evans and Philip Bryant. “LHC Machine”. In: *Jinst* 3.S08001 (2008).

[32] P. Iengo F. Kuger. “Design, construction and quality control of resistive Micromegas anode boards for the ATLAS experiment.” In: 2018. URL: https://doi.org/10.1051/epjconf/201817401013.

[33] A. Sharna F. Sauli. “Micropattern Gaseous Detectors”. In: *Annual Review Nuclear Particles Science* 49 (1999), pp. 341–388.

[34] *FieldPoint Operating Instructions, FP-AI-110 and cFP-AI-110, Eight-Channel, 16-Bit Analog Input Modules*. URL: https://manualsbrain.com/it/manuals/1163108/.

[35] in press G. Carducci et al. “Construction and test of the SM1 Micromegas chambersfor the upgrade of the ATLAS forward muon detector”. In: *NIMA* (in press).

[36] T. K. Gaisser. *Cosmic Rays and Particle Physics*. Cambridge University Press, 1990.

[37] I. Gnesi. *The Micromegas chambers for the ATLAS New Small Wheel upgrade*. 2020.

[38] M. Gupta. *Calculation of radiation length in materials*. Tech. rep. 2010.

[39] *HCLA Series, Miniature amplified low pressure sensors*. URL: https://manualzz.com/doc/20045376/hcla-series-miniature-amplified-low-pressure-sensors.

[40] E. C. Hill. *The Cosmic Muon Flux in the ATLAS Detector at the Large Hadron Collider*. 2008.

[41] J. Illingworth and J. Kittler. "A survey of the Hough transform". In: *Computer Vision, Graphics, and Image Processing* 44.87 (1988).

[42] F. Kuger. "Signal Formation Processes in Micromegas Detectors and Quality Control for large size Detector Construction for the ATLAS New Small Wheel". PhD thesis. 2017.

[43] W. R. Leo. *Technique for Nuclear and Particle Physics Experiment*. Springer-Verlag Berlin Heidelberg, 1994.

[44] *LM35 Precision Centigrade Temperature Sensors*. URL: https://www.ti.com/product/LM35.

[45] L. Martinelli. "Studio dell'impatto della mesh metallica sulle prestazioni dei rivelatori Micromegas dell'esperimento ATLAS". In: 2018. URL: https://www.sif.it/attivita/congresso/104.

[46] in press P. F. Giraud. "Micromegas internal geometry measurement". In: *NIMA* (in preparation).

[47] B.N.J. Persson and C. Yang. "Theory of the leak-rate of seals". In: *arXiv:0805.0699* (2008).

[48] M. Radmilovi´c-Radjenovi´c. "The role of the field emission effect in direct-current argon discharges for the gaps ranging from 1 to 100 μm". In: *JOURNAL OF PHYSICS D: APPLIED PHYSICS* 46 (2012).

[49] *RS-232 and RS-485 Serial Network Interfaces*. URL: https://www.yumpu.com/en/document/view/13777602/rs-232-and-rs-485-serial-network-interfaces-national-instruments.

[50] Cecchini S. and Sioli M. "Cosmic ray muon physics". In: *5th ICTP School on Nonaccelerator Particle Astrophysics*. 1998. arXiv: hep-ex/0002052.

[51] A. Salzburger. *The ATLAS Track Extrapolation Package*. Note. 2007.

[52] G. Schultz. "Mobilities of positive ions in some gas mixtures used in proportional and drift chambers". In: *HAL* 12 (1977), pp. 67–70.

[53] *The ATLAS Forward Detector project*. URL: https://atlas-project-lumi-fphys.web.cern.ch/.

[54] J. Wenninger. *Operation and Configuration of the LHC in Run 2*. Note 0007. 2019.

[55] *xAOD Samples*. URL: https://atlassoftwaredocs.web.cern.ch/ABtutorial/xaod_samples/.